DETECTING AND IMAGING MICROBUBBLE CONTRAST AGENTS WITH ULTRASOUND

by

David Hope Simpson

A thesis submitted in conformity with the requirements
for the degree of Doctor of Philosophy
Graduate Department of Medical Biophysics
University of Toronto

National Library
of Canada

Acquisitions and
Bibliographic Services

395 Wellington Street
Ottawa ON K1A 0N4
Canada

Bibliothèque nationale
du Canada

Acquisitions et
services bibliographiques

395, rue Wellington
Ottawa ON K1A 0N4
Canada

Your file Votre référence

Our file Notre référence

0-612-53785-4

Canada

Detecting and Imaging Microbubble Contrast Agents With Ultrasound

By David Hope Simpson
Doctor of Philosophy, 2000
Graduate Department of Medical Biophysics
University of Toronto

Abstract

Ischemic heart disease is one of the leading causes of morbidity and mortality worldwide. Imaging techniques that detect and measure blood flow in the heart muscle (myocardium) are used routinely to aid in the diagnosis and management of this disease. With the aid of microbubble contrast agents, myocardial blood flow can now be detected with transthoracic ultrasonic imaging, but low frame rates and/or poor image properties have limited clinical applications.

This thesis represents an attempt to optimize techniques for imaging microbubbles in tissue with ultrasound. To overcome the limitations of existing methods, a new technique, Pulse Inversion Doppler, has been developed. Algorithms for optimizing detection filters based upon the measured echoes from tissue and microbubbles have also been developed which facilitate comparisons with existing imaging techniques. Data from *in vivo* experiments show that pulse inversion Doppler can significantly outperform existing harmonic and Doppler imaging techniques, enabling realtime imaging of myocardial blood flow. Variants of pulse inversion Doppler are now available on clinical ultrasound systems. Applications for these techniques are discussed.

Acknowledgements

I owe a great deal of thanks and gratitude to the many people who have helped to make the writing of this thesis possible.

I would like to thank my supervisor and mentor, Dr. Peter Burns, for introducing me to a fascinating field of science, for instructing me in the fine art of communication (or "How to Prepare a Show-Stopping Presentation in 5 Minutes or Less"), and for showing me that much good science occurs at the borders between traditional disciplines.

To my friend and colleague Chien Ting "Cash" Chin: You are a scholar and a gentleman. Thanks for acting as a constant sounding board for new ideas, for your continued help, and for the many late night discussions on topics ranging from Copernicus to Natural Selection to Eastern medicine.

To Dr. Stuart Foster, who taught me that optimism often breeds innovation, and Dr Mike Bronskill, who taught me many valuable lessons on "onion peeling": Thanks.

To Dr. Stephanie Wilson at the Toronto Hospital: It has been a privilege to be able to work with you and to watch you at work.

To Carrie Purcell, without whose help much of the experimental work in this thesis would not have been possible: Your friendliness, professionalism and dedication make you a pleasure to work with.

To Jeff Powers, Mike Averkiou and Matt Bruce at ATL Ultrasound: Thank you for your help and assistance over the years.

To Drs. Matthew O'Donnell, Mark Henkelman and Wayne Johnston: Thank you for your constructive criticism.

To Kasia Harasiewicz: Thank you for acting as a surrogate parent to all of us in the lab, and thanks for the many early morning tennis games.

To Conrad Walker: Your boundless good humour and zest for life touched all those around you.

To my mother and father, who always provided quiet encouragement: Thanks.

To Clara, my daughter, and the joy of my heart: Thanks for teaching me how to see the world again through new eyes.

And finally, to my wife Michele, the love of my life, my best friend and my constant support along the way: Thank you for believing in me.

In Memoriam

Zane R. Holowachuk

Dr. Artur Z. Arthur

TABLE OF CONTENTS

LIST OF TABLES

LIST OF FIGURES

1 Introduction and Background

> *"...So the heart is the beginning of life, the Sun of the Microcosm, as proportionably the Sun deserves to be call'd the heart of the world, by whose virtue, and pulsation, the blood is mov'd perfected, made vegetable, and is defended from corruption, and mattering; and this familiar household god doth his duty to the whole body, by nourishing, cherishing, and vegetating, being the foundation of life, and the author of all."*
>
> from *De Generatione* (1651), William Harvey[1]

1.1 The Heart and Cardiovascular System

The human body is composed of literally trillions of cells linked together into a single organism. Each cell within the body must continually consume nutrients and dispose of wastes to function properly. Since diffusional transport is only effective over a range of several cell diameters (60 to 80 μm (Fox 1987)), the body relies on a highly developed system, the cardiovascular system, to transport nutrients to cells and to remove waste.

The human cardiovascular system involves an estimated 100 000 kilometers of vessels through which blood circulates constantly (Fox 1987). The heart, whose four chambers comprise two separate pumps, controls the motion of blood through these vessels. The right heart comprises the right atrium and right ventricle and pumps blood through the pulmonary circulation, where waste carbon dioxide is exchanged for oxygen in the lungs (Figure 1). From the lungs, blood returns to the left heart, which comprises the left atrium and left ventricle. The left heart is the main pump that drives blood through the systemic circulation. Blood is pumped from the left ventricle into the aorta, and is distributed throughout the body through a series of branching vessels decreasing in size from the arteries to arterioles, to the smallest capillaries with

---

[1] (translated in (Porter 1997))

sizes on the order of 7 to 10 μm. Although they contain less than 7% of the systemic blood volume (Nichols and O'Rourke 1998), the systemic capillaries have over 80% of the surface area and account for most of the exchange between blood and tissue. From the capillaries, blood drains into a series of larger vessels from venules, to veins, to the venae cava which return blood to the right atrium. Compared to the arteries, the veins have relatively larger diameters and smaller velocities, so that the venous system contains about 70% of the blood volume in the systemic circulation (Nichols and O'Rourke 1998). The properties of some of these vessels in humans are listed in Table 1.

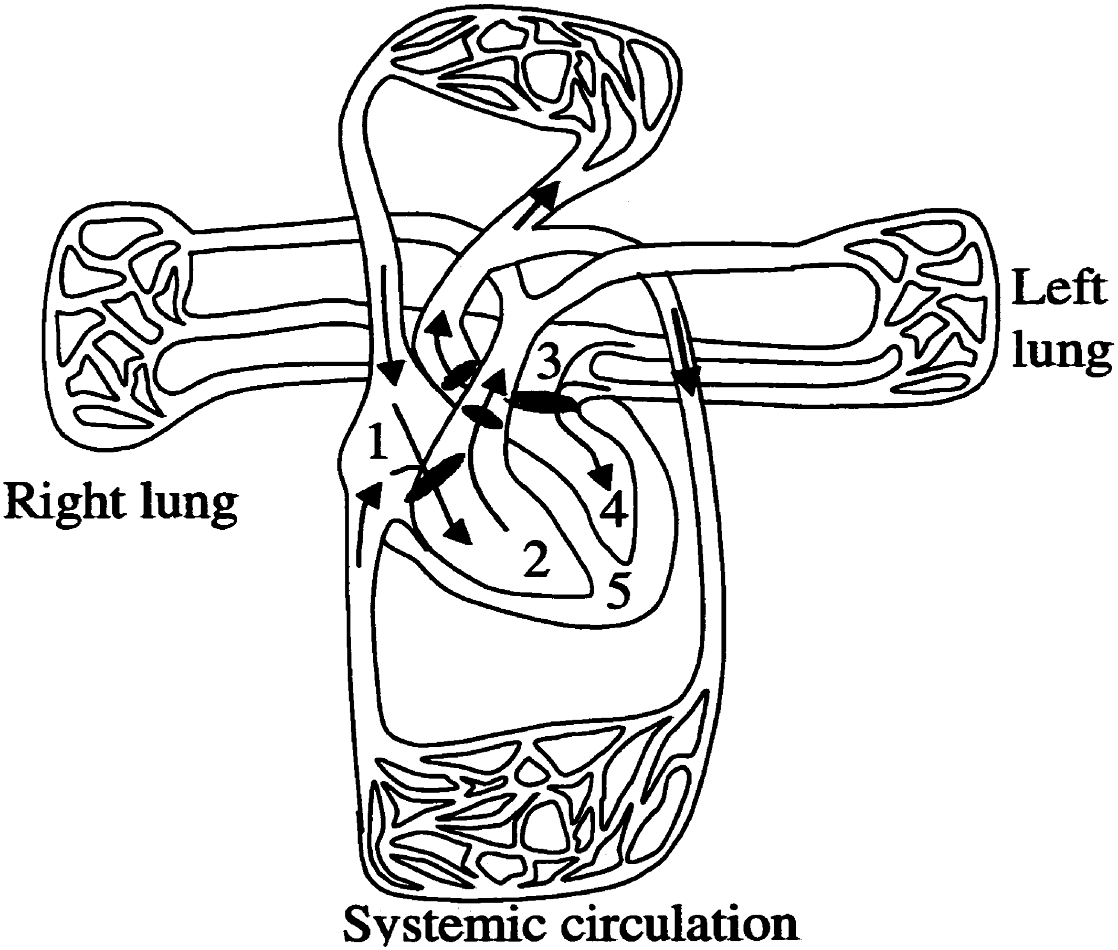

Figure 1: Schematic of the circulatory system. Venous blood returns to the heart via the right atrium (1) and enters the right ventricle (2). The right ventricle contracts, ejecting blood into the pulmonary circulation. Oxygenated blood from the lungs returns to the heart via the left atrium (3), and enters the left ventricle (4), which contracts, pumping blood out the aorta and into the systemic circulation. The heart wall, or myocardium (5) provides the pumping action of the heart.

Table 1: Properties of Selected Blood Vessels in humans **(Jensen 1996)**

Vessel	Internal Diameter	Length	Peak Velocity	Mean Velocity
Aorta	$0.5\text{-}2.4 \times 10^{-2}$ m	3.5×10^{-1} m	0.6-2.9 m/s	$0.8\text{-}4 \times 10^{-1}$ m/s
Femoral artery	$2\text{-}8 \times 10^{-3}$	1×10^{-1}	1.0-1.2	$1.0\text{-}1.5 \times 10^{-1}$
Carotid Artery	$2\text{-}8 \times 10^{-3}$	$1\text{-}2 \times 10^{-1}$	1.1-1.5	
Arteriole	$1\text{-}8 \times 10^{-5}$	$1\text{-}2 \times 10^{-3}$	$0.5\text{-}1 \times 10^{-2}$	
Capillary	$4\text{-}8 \times 10^{-6}$	$0.2\text{-}1 \times 10^{-3}$	$0.2\text{-}1.7 \times 10^{-3}$	
Inferior Vena Cava	$0.6\text{-}1.5 \times 10^{-2}$	$2\text{-}4 \times 10^{-1}$	$1.5\text{-}4.0 \times 10^{-1}$	

The wall of the heart is composed of bands of muscle fibers, collectively known as the myocardium. Blood flow to the myocardium is provided by the left and right coronary arteries which arise from the aorta immediately downstream of the aortic valve, and branch over the outer surface of the heart (Kassab et al. 1994b). Smaller arterioles then pass radially inwards to supply a thick web of capillaries within the myocardium. Venules draining the myocardium pass outwards to the surface of the heart into a series of collecting veins that ultimately drain into the right atrium (Kassab et al. 1994a). As a result of this configuration, blood flow within the heart muscle itself occurs predominantly in small arterioles, capillaries and venules, sometimes referred to as the coronary microcirculation (Kassab and Fung 1994).

1.1.1 Ischemic Heart Disease

When the blood supply to a region of tissue is inadequate to meet the demand for oxygen, the tissue is said to be ischemic. In the heart, moyocardial ischemia most often occurs as a result of atherosclerosis in the main coronary arteries. Atherosclerotic plaques (or atheromas) develop over time in these vessels, gradually narrowing their diameters until they begin to affect blood flow to the myocardium. In some instances, the plaques may actually rupture, blocking blood flow completely and causing death of a portion of the heart muscle (a myocardial infarction). Ischemic heart disease is one of the leading causes of morbidity and mortality worldwide. In Canada, the direct costs from ischemic heart disease (including hospitalization, physicians, drugs and research) and indirect costs (including short term and long term disability and mortaility costs) are estimated at over 7 billion dollars annually, and approximately 1 in 5 people will eventually die from this disease (Wielgosz et al. 1999).

A variety of imaging techniques are currently used to assess the nature and extent of myocardial ischemia in patients (Skorton et al. 1992; Van Der Wall et al. 1998). Techniques in clinical use include single photon emission computed tomography (SPECT), positron emission tomography (PET), and ultrasound. SPECT uses photon emitting radioisotopes such as Tl-201 (a potassium analog) and Tc-99m Sestamibi (MIBI), whose myocardial uptake is a measure of blood flow and the integrity of cell membranes (Hesse 1999; Maddahi et al. 1991). PET uses positron emitting radioisotopes whose myocardial uptake can be used to image and measure myocardial blood flow (e.g: ^{82}Rb, ^{13}N ammonia, and ^{15}O water)(Schelbert 1993), and metabolic activity (e.g.: ^{18}F fluoro-deoxyglucose). PET offers a wider choice of tracers and better quantification than SPECT, but requires more complicated radioisotope preparation, is more expensive and is less widely available. Unlike PET and SPECT which require long acquisition times (on the order of ½ minute per projection and 30 minutes for complete acquisition for SPECT (Garcia 1996)), ultrasound imaging can be performed in "real-time" at rates exceeding 30 frames per second. Real-time ultrasound imaging in conjunction with pharmacological or exercise stress testing is currently used to assess the mechanical function of the heart muscle (Bax et al. 1999; Senior et al. 1999). Ischemic and infarcted myocardium are identified as regions with abnormal or absent wall motion and reduced thickening on contraction. The fraction of blood in the left ventricle ejected with each beat (the ejection fraction) – an important global measure of cardiac function – also may be calculated with all three modalities.

In addition to the techniques described above, new techniques such as electron beam computed tomography (EBCT) and magnetic resonance imaging (MRI) are also being developed to assess ischemic myocardium (Lerman et al. 1999; Schmermund et al. 1998; Van Der Wall et al. 1998). Both of these techniques use diffusable contrast agents which produce a myocardial enhancement that initially is proportional to blood flow. The gadolinium agents used in MRI show prolonged retention in infarcted myocardium, offering an "infarct-avid" imaging technique (Higgins 1993). MRI agents that remain within the blood are also under development (Marchand et al. 2000; Prasad et al. 1999).

Compared with other cardiac imaging techniques, ultrasound offers significant advantages in many situations. It is widely available, relatively inexpensive, offers high spatial and temporal resolution (1 to 2 mm at 30 frames/sec), does not involve ionizing radiation, requires short exam times, and is potentially portable (complete hand-held ultrasound machines weighing less than 3kg are now available (Hwang et al. 1998)). Despite these advantages, ultrasound has been limited by its inability to measure myocardial blood flow non-invasively. A non-invasive means of measuring blood flow in the myocardium with ultrasound could have a significant impact on the diagnosis and management of patients with ischemic heart disease.

1.2 Basic Principles of Ultrasonic Imaging

Ultrasonic imaging uses pulse/echo ranging principles similar to those used in radar and sonar. The imaging process starts with the application of an electrical pulse to an ultrasonic transducer. The transducer converts this electrical pulse into a high frequency ultrasound pulse that it directs into tissue (Figure 2a). The transmitted pulse is composed of a high frequency sinusoidal "carrier", usually at or near to the natural resonant frequency, f_0, of the transducer, modulated by a slowly-varying "envelope", ε(t) (Figure 2b):

$$p(t) = \varepsilon(t) \cdot \cos 2\pi f_0 t, \qquad 1$$

where *t* is the time from the start of transmission.

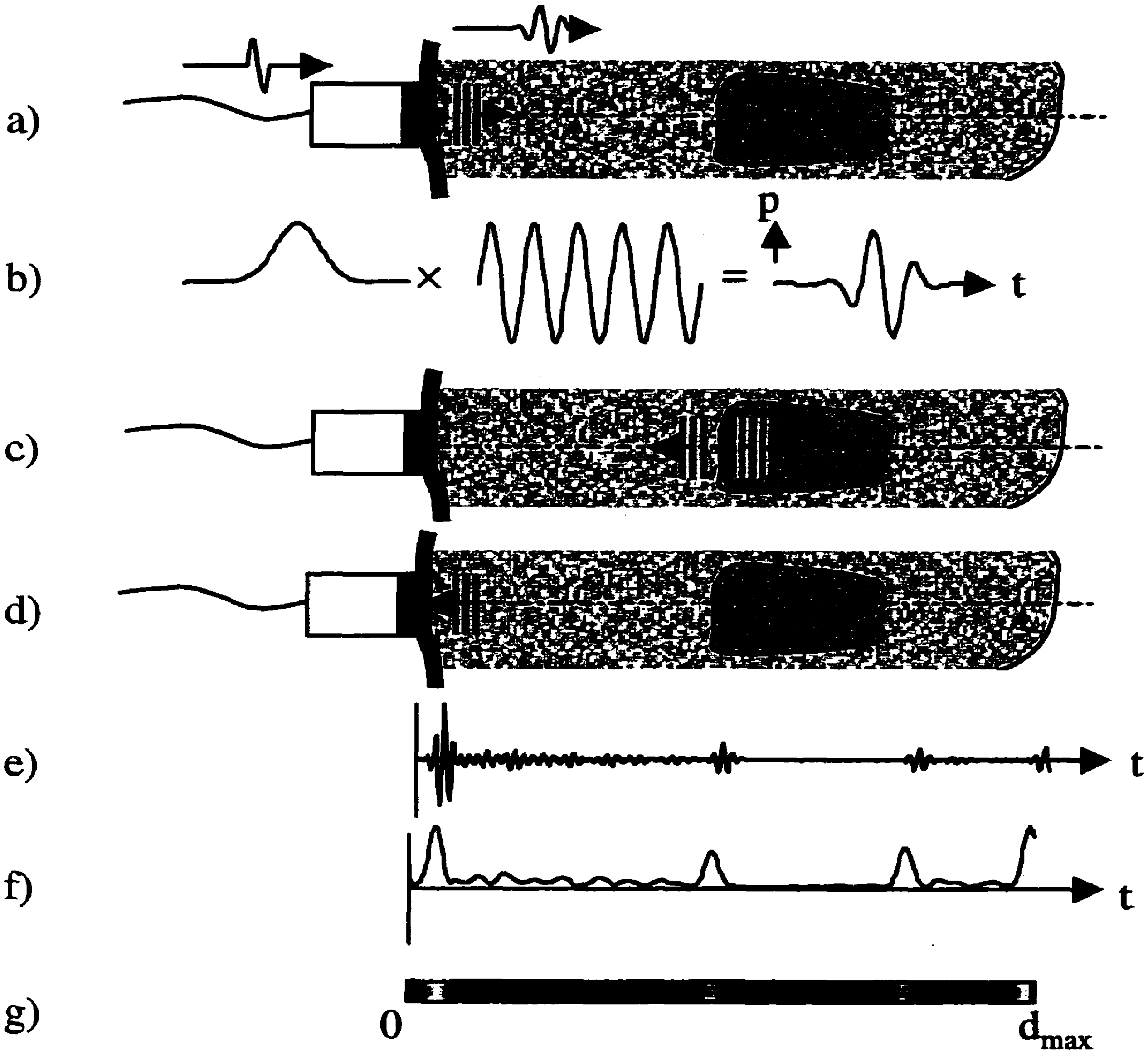

Figure 2: Principles of ultrasonic imaging: a) an ultrasonic pulse is transmitted into tissue; b) the transmitted pulse is the product of a slowly varying envelope and a sinusoidal "carrier"; c) echoes are produced by structures in the body; d) the echoes are detected by the transducer and reconverted into an electrical signal (e); f) the signal is compensated for attenuation and the envelope is extracted; g) each echo is converted into a line in the image with a brightness related to the intensity of the echo.

Whenever the outgoing pulse encounters an interface between tissues with different mechanical properties, a fraction of the sound energy is scattered back towards the transducer (Figure 2c), where it is reconverted into an electrical echo signal, $s(t)$, which is the sum of the echoes from all scattering interfaces (using the subscript I to denot the ith interface) along the line of sight (Figure 2d,e):

$$s(t) = g(t)\sum_{i}\varepsilon_i'\left(t - t_{d,i}\right)\cdot\cos 2\pi f_0\left(t - \Delta t_{d,i}\right) \tag{2}$$

where the subscript i is used to denote the i^{th} interface. Here, ε is replaced by ε' to show that the envelope of the each echo will differ from the envelope of the transmitted pulse due to the combined effects of attenuation, scattering, the frequency response of the transducer, and filtering of the echo signals.

Because the speed of sound in most soft tissues is similar, each echo will arrive back at the transducer with a delay, $t_{d,i}$, proportional to the depth of the corresponding interface:

$$t_{d,i} = \frac{2\cdot depth_i}{c_{sound}}, \tag{3}$$

where c_{sound} is the speed of sound in tissue.

As sound travels through tissue, it is attenuated due to scattering and absorption, making echoes from deeper structures weaker than those from superficial structures. To compensate for the depth-dependent intensity of the returning sound, the echo signals are amplified by an amount, $g(t)$, that increases with increasing delay times in a process known as time-gain compensation (TGC). Following amplification and TGC, the envelope of each echo signal is found (Figure 2f). To make a cross-sectional image each detected echo signal is converted to a line in the image whose brightness at each point is related to the amplitude of the echo envelope from the corresponding depth (Figure 2g). The pulse/echo process is then repeated rapidly down many lines of sight and an image is formed. Such ultrasound imaging is referred to variously as greyscale imaging, 2D imaging or B-mode (Brightness) imaging. Depending on the maximum imaging depth and the number of pulses transmitted, sustained rates of over 50 2D images per second can be produced by clinical ultrasound systems. Sample ultrasound images of the heart are shown in Figure 3.

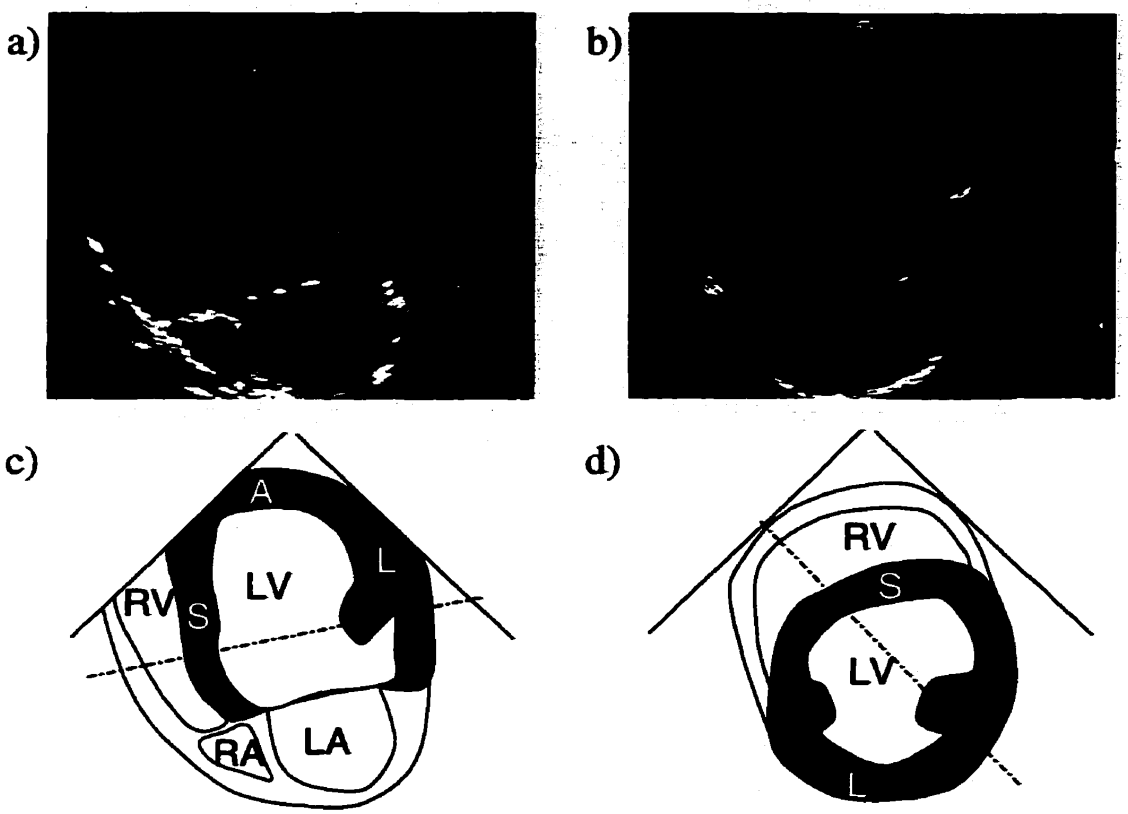

Figure 3: Ultrasonic cross-sectional images of a dog heart made with a phased array transducer: a) apical 4-chamber view (foreshortened); b) Right parasternal short axis view; c),d) schematics of a) and b). The right hand side markers are in cm. LV=left ventricle, RV = right ventricle; LA = left atrium; RA=right atrium; S=septum; A=apex; L=lateral wall. The myocardium of the left ventricle (shaded) is of primary interest in perfusion imaging.

1.2.1 Connections Between Mechanical and Acoustic Properties

Ultrasound waves are longitudinal pressure waves created by alternately pushing and pulling on a medium. We can think of the medium as an assembly of small masses connected by springs: the masses are compressed together during the push (or condensation) and moved apart by the pull (or rarefaction). The combination of the spring forces and the inertia of the masses causes the sound wave to propagate through the medium with a speed given by

$$c_{sound} = 1/\sqrt{\rho_o \beta}, \qquad 4$$

where ρ_0 (kg/m^3) is the density of the medium (the masses), and β (Pa^{-1}) is the adiabatic bulk compressibility of the medium (the springs). For diagnostic ultrasound imaging, the speed of sound in tissue is usually assumed to be constant at 1540 m/s, which is close to the speed of sound in water at body temperature.

The relationship between sound speed, frequency (f) and wavelength (λ) is given by

$$f\lambda = c_{sound} \qquad 5$$

or

$$\lambda = c_{sound}/f. \qquad 6$$

For diagnostic imaging, sound frequecies of 2 to 10 MHz are commonly used corresponding to wavelengths between 0.75 and 0.15 mm. The wavelength of sound acts as a form of ruler for medical ultrasound, governing imaging resolution and the nature of scattering processes.

1.2.2 Bandwidth and Axial Resolution

Ultrasonic imaging uses echo delays to measure distances (see Equation 3). If the duration of the transmitted pulse is τ_{pulse} seconds, then echoes arriving less than τ_{pulse} seconds apart will be blurred together. This blurring limits the axial resolution of the imaging system to:

$$axial\ resolution \approx \frac{c_{sound}\tau_{pulse}}{2}. \qquad 7$$

To optimize axial resolution, the transmitted pulse must be as short as possible. Figure 4 shows two possible ultrasound pulses together with the spectra of sound frequencies required to form them. The duration and bandwidth of a sound pulse are inversely related to each other. Hence, imaging resolution is inversely proportional to bandwidth:

$$\boxed{\textit{axial resolution} \propto \frac{1}{\textit{bandwidth}}} \qquad 8$$

For typical modern ultrasound systems, the range of frequencies that can be transmitted efficiently by a single transducer (the transducer's bandwidth) ranges from 50 to 100 % of the transducer centre frequency. Combining this fact with Equations 6 and 7, the finest imaging resolution possible is approximately equal to the wavelength of sound at the centre frequency of the transducer:

$$\text{maximum resolution} \approx \lambda/2. \qquad 9$$

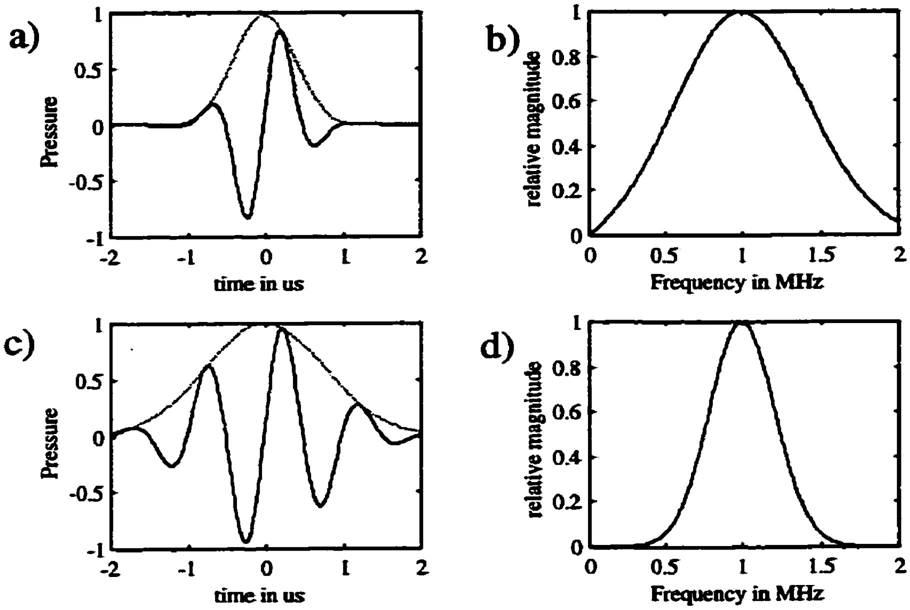

Figure 4: Relationship between bandwidth and resolution: A short ultrasound pulse (a), contains a broad spectrum of sound frequencies (b). Doubling the duration of the pulse (c) halves its bandwidth (d).

1.2.3 Reflection and Scattering

Interfaces with a lateral extent much larger than the wavelength, such as the interface between two organs, behave as specular reflectors, reflecting sound as a mirror reflects light. For normally incident plane waves, the fraction of the incident sound intensity reflected by such an interface, R_{12}, is independent of sound frequency and is given by (Shung and Thieme 1993)

$$R_{12} = \left(\frac{Z_2 - Z_1}{Z_1 + Z_2} \right)^2 \qquad 10$$

where Z_1 and Z_2 are the characteristic acoustic impedances of the two tissues forming the interface. The characteristic acoustic impedance of a medium is defined as the ratio of the incident acoustic pressure at a point in the medium to the particle displacement at the same point. For plane waves, the acoustic impedance (in Rayls) is

$$Z = \rho_0 c_{sound} = \sqrt{\rho_0 / \beta} \qquad 11$$

When a sound wave encounters multiple scattering interfaces in tissue with dimensions on the order of the sound wavelength or smaller, the scattering process, sometimes called stochastic scattering, is much more complicated. For any scatterer, the scattering cross-section in mm^2, $\sigma(f)$, is a function of the frequency and may be defined as

$$\sigma(f) = \frac{\text{total scattered power}}{\text{incident intensity}} \qquad 12$$

The differential backscatter cross-section of a single scatterer, $\sigma_d(f)$ (m^2·Sr^{-1}) is defined similarly as the power scattered backwards per unit solid angle divided by the incident intensity. For a complex medium such as tissue, composed of many random scatterers, the backscatter coefficient, $\sigma_b(f)$ (m^{-1}·Sr^{-1}), is defined as the differential backscattering cross-section per unit volume.

1.2.4 Attenuation

As an ultrasound wave propagates through a uniform tissue, its intensity decreases exponentially with depth due to absorption and scattering. The attenuation coefficient for a given tissue, $\alpha(f)$(dB·m^{-1}), is defined as the fractional rate of attenuation per unit depth and is a function of frequency. For most tissues, $\alpha(f)$ increases approximately linearly with frequency, with typical values ranging from 0.3 to 0.7 dB/cm/MHz.[2]

Together, specular reflection, stochastic backscatter and attenuation are responsible for the appearance of tissue in an ultrasound image. Specular reflections produce strong echoes along the boundaries between different organs, which are useful for depicting anatomy. Backscatter produces different levels of image brightness depending upon inter-cellular and intra-cellular structure, enabling different tissues to be distinguished. Changes in attenuation produce either shadows or enhancement behind structures in the body and can be used to differentiate and identify tissues.

1.2.5 Doppler Ultrasound Detection of Blood Flow

In the frequency range used in medical ultrasound (2 to 10 MHz), blood is a very poor reflector of ultrasound, with a backscatter coefficient between 100 and 500 times smaller (20-27 dB smaller) than the backscatter coefficients of soft tissues (Jensen 1996; Shung et al. 1976; Shung and Thieme 1993). Reflections from blood within vessels less than one or two wavelengths in diameter (0.15 to 1.5 mm depending on frequency) are thus masked by the stronger echoes from the surrounding tissues and cannot normally be seen. For this reason, ultrasound greyscale imaging is of limited utility in imaging the anatomy of the vascular system and cannot provide functional information about haemodynamics.

---

[2] The Decibel scale is a logarithmic scale used to compare power or intensity. It is defined by:

$$power(dB) = 10\log_{10}\left[\frac{power}{reference\ power}\right].$$

Thus, 10 decibels (dB) represents a power 10 times larger than the reference value and 20 dB represents a power 100 times greater than the reference value.

Pulsed Doppler ultrasound offers a method to detect the presence and velocity of moving blood (Jensen 1996). With this technique, a rapid series of ultrasonic pulses is transmitted down the same line of sight into tissue and the echoes are detected for processing. Echoes from scatterers moving towards or away from the transducer will arrive at the transducer with delays that change from echo to echo. For an isolated scatterer moving towards the transducer with a relative velocity, v, the echo signal, $s(k,t)$, due to the k^{th} transmitted pulse will be (from Equation 2):

$$s(k,t)=g(t)\varepsilon'\left(t-t_d-(k-1)\Delta t_d\right)\cdot\cos 2\pi f_0\left(t-t_d-(k-1)\Delta t_d\right), \tag{13}$$

where t represents the time from the start of transmission of the k^{th} pulse. The change in delay, Δt_d, between successive echoes will be proportional to velocity (from Equation 3):

$$\Delta t_d=\frac{2\Delta depth}{c_{sound}}\approx\frac{2vT}{c_{sound}}, \tag{14}$$

where T is the pulse repetition interval (PRI) (the time between successive pulses)[3].

To extract the delays, the carrier frequency components of the echo signals are usually removed in a process known as quadrature demodulation. Each echo signal is multiplied by $\cos 2\pi f_0 t$ and $\sin 2\pi f_0 t$ then filtered to remove noise and high frequency components, yielding two signals, denoted $I(k,t)$ (in-phase) and $Q(k,t)$ (quadrature) respectively:

$$\begin{aligned} I(k,t) &= g(t)\varepsilon''\left(t-t_d-(k-1)\Delta t_d\right)\cdot\cos\phi(k), \\ Q(k,t) &= g(t)\varepsilon''\left(t-t_d-(k-1)\Delta t_d\right)\cdot\sin\phi(k), \\ \varphi(k) &= \phi_d-2\pi f_0\frac{2v}{c_{sound}}kT, \end{aligned} \tag{15}$$

where $\phi(k)$ is independent of t and ϕ_d is a constant. The term ε'' is used in this equation to show that the echo signal envelope may be affected by the filters used in the demodulation process. These expressions assume that attenuation does not cause significant changes Following demodulation, a time delay, t_{gate}, is chosen corresponding to a depth of interest down the line of sight, and the in-phase and quadrature signals from each echo are sampled at this delay and combined to form a sampled complex Doppler signal, $A(k)$ (Figure 5):

$$\begin{aligned} A(k) &= I(k,t_{gate})+iQ(k,t_{gate}) \\ &= \underbrace{g(t_{gate})\varepsilon''\left(t_{gate}-t_d-(k-1)\frac{2v}{c_{sound}}T\right)}_{envelope}\cdot\underbrace{e^{-i2\pi f_d kT}}_{complex\ \ sinusoid}, \end{aligned} \qquad 16$$

where:

$$\boxed{f_d=\frac{2v}{c_{sound}}f_0} \qquad 17$$

Equation 16 shows that the Doppler signal, $A(k)$, will be the product slowly varying envelope and a complex sinusoid with a frequency, f_d, proportional to velocity as given by the Doppler equation (Equation 17), sampled at the Doppler pulse repetition frequency, $f_{pr}=1/T$.

When the echoes from all scatterers at the depth of interest are combined, *A(k)* will contain a spectrum of Doppler frequencies related to the distribution of scatterer velocities. To estimate the distribution of blood velocities, a high-pass filter (a "clutter" or "wall" filter) is applied to the Doppler signal to eliminate echoes from slow-moving tissue, and a windowed Fourier transform is then applied to the filtered signals. Due to the sampled nature of the Doppler signal, velocities can be calculated unambiguously only if all Doppler frequency shifts are below the Nyquist frequency, f_{Nyq}, defined as:

---

3 The approximation in Equation 14 is valid when $v/c_{sound} \ll 1$. In the human body, the fastest velocities are on the order of 1 to 3 m/s for blood flow in the aorta (Jensen 1996), so that $v_{\max}/c_{sound} < 1/500$.

$$f_{Nyq} = \frac{f_{pr}}{2}. \qquad 18$$

Doppler frequencies higher than f_{Nyq} will produce an artifact known as aliasing, and will be misinterpreted as lower frequencies (Jensen 1996).

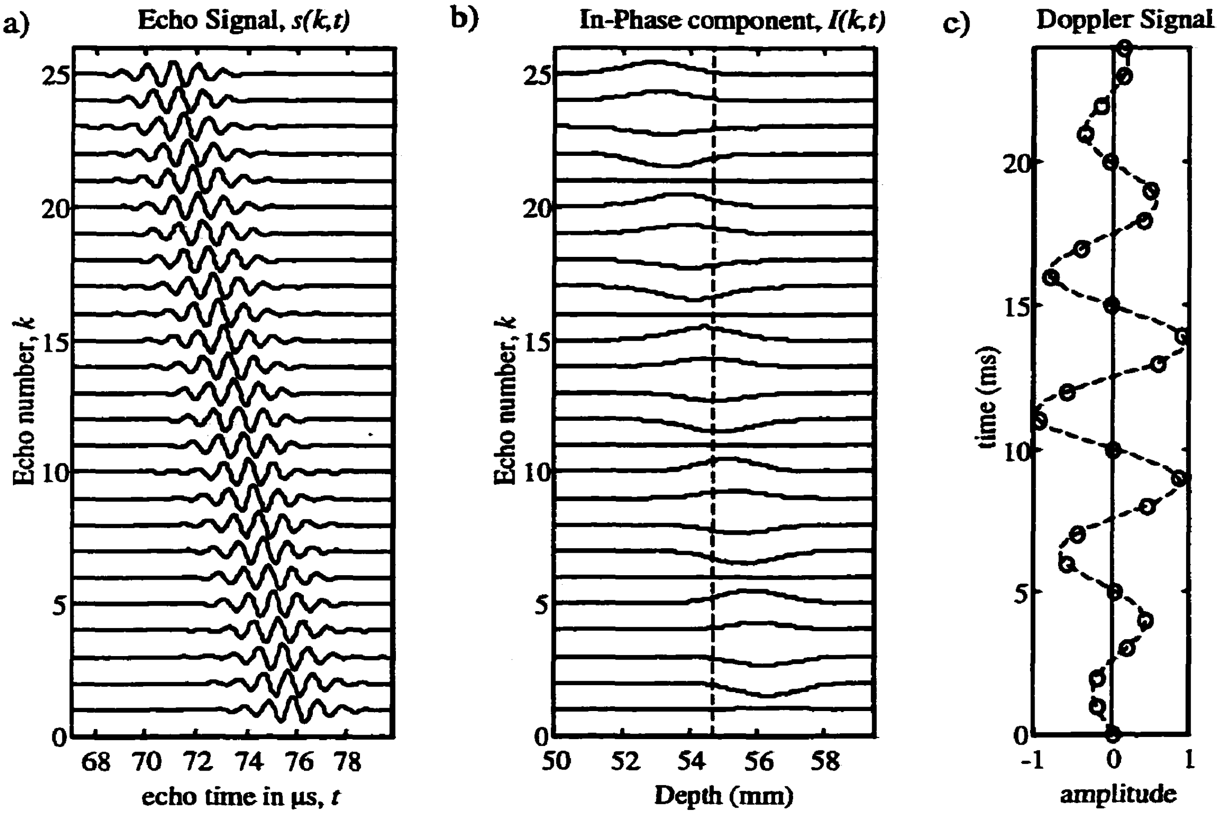

Figure 5: Simulation of pulsed Doppler detection: a) simulated echo signals for a moving target, s(k,t)*; b) in-phase component of demodulated echoes,* I(k,t)*, showing the location of the sample gate (dotted line). The echo time on the horizontal axis has been converted to depth; c) real component of Doppler signal,* A(k)*, from sample gate. The frequency of the Doppler signal is proportional to velocity. The simulation parameters were:* f_0= *1 MHz,* T= *1 ms (PRF= 1 kHz),* v= *15 cm/s, giving* f_d=*200 Hz (Equation 17).*

1.2.6 Colour Doppler Imaging

By transmitting from 4 to 16 Doppler pulses down each lines of sight in the image plane and processing the resulting echoes, a colour Doppler image can be formed in which colour indicates the estimated mean velocity of the moving blood at each point on the image (Ferrara and DeAngelis 1997). Rather than calculating the Doppler spectrum from 4 to 16 samples, algorithms are usually employed which estimate velocity from the mean change in time delay or phase using Equations 14 or 15 respectively (Omoto and Kasai 1987). A related technique, power Doppler imaging, produces an image whose colour is related to the power of the Doppler signal, which is proportional to the volume of moving blood at each point on the image (Rubin et al. 1995). Such Doppler ultrasound systems provide anatomical and functional information about the vasculature and are widely used clinically to detect the presence and velocity of blood flowing in large blood vessels (arteries, large arterioles and veins) (Taylor et al. 1995).

1.2.7 Limitations of Doppler Techniques

Two sources of unwanted signals mask the echoes from blood and limit the performance of Doppler ultrasound: echoes from moving tissue ("clutter"), and electronic noise from various sources (such as the thermal motion of electrons in the transducer and Doppler receiver). The Doppler filters that remove clutter ("clutter" filters) also remove the echoes from slowly moving blood (Winkler and Helmke 1990; Winkler et al. 1990). Electronic noise can mask the weak echoes from small volumes of blood located deep in tissue (Winkler and Helmke 1990). Together, these two factors prevent the reliable detection of blood in small arterioles, capillaries, and venules such as those found in the coronary microcirculation.

1.3 Microbubble Contrast Agents

One way to make blood more detectable by ultrasound is to introduce scattering particles into the blood. To recirculate freely, these particles must be smaller than the diameter of the smallest capillaries in the lungs (about 10μm) and consequently much smaller than the wavelengths of sound used for medical imaging (150 to 750 μm). The scattering cross-section of such a particle can be approximated by (Morse and Ingard 1968)

$$\sigma(\lambda) \cong \frac{1}{9} 4\pi R^2 \left(\frac{2\pi}{\lambda} R\right)^4 \left(\left| \frac{\beta_p - \beta_b}{\beta_b} \right|^2 + \frac{1}{3} \left| \frac{3\rho_p - 3\rho_b}{2\rho_p + \rho_b} \right|^2 \right) \qquad 19$$

where the subscripts p and b denote particle and blood respectively, and R is the particle radius. This cross-section can be maximized if the compressibility of the particles is much greater than the compressibility of blood, making gas bubbles the best choice for such scatterers (Ophir and Parker 1989).

Gas bubbles were first detected in the body with ultrasound in 1968 as an incidental and transient finding following the rapid injection of saline into the heart (Gramiak and Shah 1968). Unfortunately, free gas bubbles small enough to pass through capillaries are unstable in the blood and dissolve in a fraction of a second due to the combined effects of surface tension and diffusion (Epstein and Plesset 1949). To prevent dissolution and allow microbubbles to recirculate for several minutes, the bubbles must be stabilized, either by surrounding them with a shell, or by filling them with low solubility, high molecular weight gases such as perfluorocarbons, or both. The use of ultrasound contrast agents was consequently limited to direct intraventricular or intracoronary injections until techniques were perfected for producing stable gas microbubbles capable of traversing the pulmonary circulation.

The first transpulmonary contrast agent, Albunex™ (Mallinckrodt Medical, St. Louis), consisting of air bubbles stabilized with a shell of human serum albumin, was introduced in the mid 1980's. This agent contains micron-sized bubbles ranging in diameter from approximately 1 to 10 μm, with a mean diameter of approximately 4 μm. Albunex was originally developed, not to enable detection of blood flow in the smallest vessels in the human body, but to improve visualization of the border of the left ventricle, the largest blood reservoir in the body (Feinstein et al. 1990).

A number of microbubble contrast agents are now undergoing clinical trials or are approved for use. These agents contain from 10^8 to 10^{10} bubbles per millilitre, and are typically administered in boluses of 5 to 50 microlitres per kilogram of body mass. Table 2 summarizes the properties of some of these agents **(Becher and Burns 2000; Correas 1996; Schlief 1996; Skyba et al. 1996; Sontum et al. 1999)**.

Table 2: Properties of Ultrasound Contrast Agents

Agent	Manufacturer	Gas	Shell	Mean Diameter
AI700	Acusphere	Perfluorocarbon	Synthetic Polymer	?
Albunex*	Mallinckrodt Medical Inc.	Air	Cross-linked Albumin	4.3 μm
Optison*	Mallinckrodt Medical Inc.	Perfluoropropane	Cross-linked Albumin	2-5
Echovist**	Schering AG	Air	(galactose matrix)	
Levovist***	Schering AG	Air	Palmitic Acid	2-3
Sonavist	Schering AG	Air	Cyanoacrylate (polymer)	~1
Echogen	Sonus Pharmaceuticals	Dodecafluoropentane	Surfactant	2-5
Sonovue	Bracco	Sulfur Hexafluoride	Phospholipid	~3
Definity	Dupont Pharmaceuticals	Perfluoropropane	Phospholipid bilayer	?
Sonazoid (NC100100)	Nycomed	Perflurocarbon	Lipid	3.2
Quantison	Quadrant	Air	Albumin	3.2
BiSphere	Point Biomedical	Air	Biodegradable Polymer	
Imavist	Alliance/Schering	Perfluorohexane-air	Buffered surfactant	?

Note: ? = information not available, * = FDA approved (USA), ** = approved in Europe, *** = approved in Canada and Europe.

1.3.1 Acoustic Properties of Microbubble Contrast Agents

If the behaviour of microbubbles in a sound field were simply to increase the scattering from blood as suggested by Equation 19, then the treatment of bubble scattering would be complete. However, this equation was developed to describe scattering from semi-rigid particles, and does not adequately describe the complex acoustic behaviour of gas bubbles. A gas bubble can be modeled as a sphere of light, highly compressible gas surrounded by dense, virtually incompressible fluid (Leighton 1994). When the bubble is compressed by a sound wave, the compressed gas acts as a spring, pushing out on the water to restore the bubble to its equilibrium size. As the bubble changes size, it must move the water surrounding it, which behaves as though it has an effective mass equal to three times the mass of water displaced by the bubble (Leighton 1994). Such a coupling of a mass with a restoring spring acts as an oscillator that can absorb and release energy extremely efficiently when driven at its natural resonant frequency. Assuming that the pressure, p, and volume, V, of the gas obey a polytropic gas law of the form $pV^{\kappa} = \text{constant}$, the resonant frequency for small amplitude oscillations of a free gas bubble, f_0, is approximately

$$f_0 = \frac{1}{2\pi R}\sqrt{\frac{3\kappa p_o}{\rho}} \qquad 20$$

where p_0 is the ambient pressure surrounding the bubble (Anderson and Hampton 1980). For an air bubble in water at one atmosphere under adiabatic conditions, this equation reduces to (Leighton 1994)

$$f_0 R \approx 3 m/s \qquad 21$$

or

$$\frac{R}{\lambda} \approx \frac{1}{500}. \qquad 22$$

Equation 21 predicts that the resonant frequency of a micron-sized gas bubble (capable of recirculating) will be 3 MHz, which is in the middle of the diagnostic frequency range. When the above equations are modified to account for surface tension and shell elasticity (Anderson and Hampton 1980), the predicted resonant frequencies of contrast microbubbles will be somewhat higher, so that a 6 μm diameter bubble of Albunex is predicted to resonate at approximately 5 MHz (de Jong 1997; Medwin 1977).

Medwin provides an approximate formula for the scattering cross-section of a single gas bubble as a function of radius and frequency (Medwin 1977):

$$\sigma(R,f)=\frac{4\pi R^2}{\left[\left(\frac{f_0}{f}\right)-1\right]^2+\delta^2}, \qquad 23$$

where δ is a dimensionless term representing the summed effects of viscous, thermal, and radiation damping (radiation damping refers to the energy carried away by the scattered sound wave). For air bubbles between 2 and 20 µm, δ is approximately 0.15 (Leighton 1994). Below resonance, this scattering cross-section has a frequency dependence similar to that given by Equation 19 (Figure 6). Near resonance, the scattering cross-section increases significantly, limited only by damping effects. Above resonance, this model predicts that the scattering cross-section is approximately 4 times the geometric cross-section (πR^2), however this model is less accurate above resonance and higher order terms are required (Anderson and Hampton 1980).

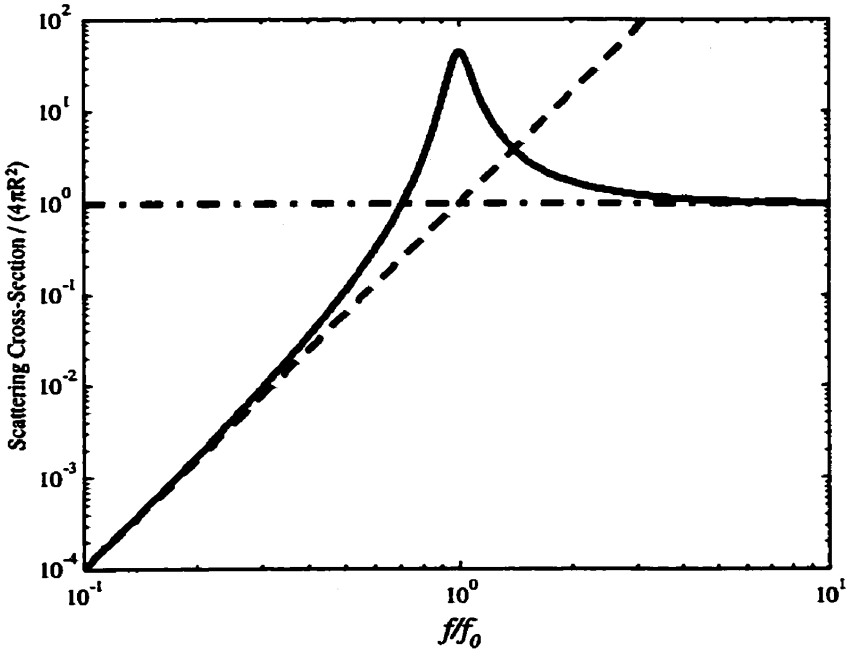

Figure 6: Theoretical backscatter cross-section of a micron-sized gas bubble (from Equation 23 with δ=0.15), normalized to $4\pi R^2$ and plotted as a function of normalized frequency.

Because all available contrast agents contain a range of bubble sizes, the echoes from a population of contrast microbubbles will be the sum of the contributions from bubbles of many sizes, and the frequency dependence will be less marked than that given by Equation 23. Shell damping will further reduce resonance. For example, the backscatter spectrum from Albunex has almost no resonance peak (de Jong 1997; de Jong and Hoff 1993).

1.3.1.1 Attenuation

The viscous, thermal and radiation damping effects listed above cause energy to be removed from the incident sound beam. This energy loss for a free gas bubble is given by the extinction cross-section, $\sigma_e(f)$ (de Jong 1997; Medwin 1977):

$$\sigma_e(f)=\frac{\delta}{\delta_{rad}}\sigma(f)=\sigma(f)+\sigma_a(f) \qquad 24$$

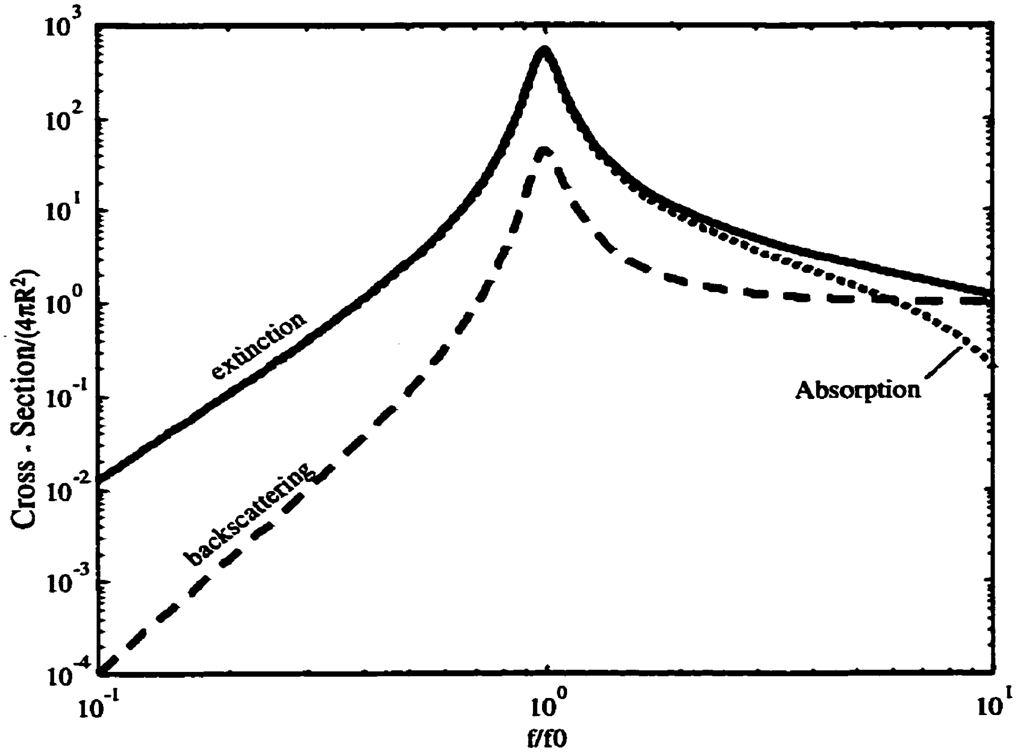

Figure 7: Theoretical extinction (solid line), absorption (dotted line) and back-scattering (dashed line) cross-sections for a micron-sized air bubble plotted against normalized frequency.

where $\delta_{rad} = 2\pi f R / c_{sound}$ is the radiation damping contribution to δ, and $\sigma\ (f)$ is the absorption cross-section (which describes non-radiative energy loss). From Equations 21, 23, and 24, the scattering, absorption and extinction cross-sections for a micron-sized gas bubble are shown in Figure 7. For small bubbles below their resonant frequency, attenuation is due mainly to absorption; for larger bubbles above resonance, attenuation is due primarily to scattering. Boukaz et al. have proposed that the scattering to attenuation ratio (STAR), defined as $\sigma(f)/\sigma_e(f)$, be used as a figure of merit for ultrasound contrast agents (Boukaz and De Jong 1996). STAR values up to 12% have been reported for Albunex (Boukaz and De Jong 1996).

As with backscatter, the attenuation for a population of bubbles will contain contributions from bubbles of many sizes and will therefore exhibit less of a resonance peak than the single bubble resonance shown in Figure 7 (de Jong and Hoff 1993).

1.3.1.2 Effects of Agent Concentration

For dilute solutions of a given contrast agent and fixed transmission conditions, backscatter is directly proportional to agent concentration (de Jong 1997). Doppler power from flowing agent is also proportional to agent concentration, provided that the flow conditions remain constant (Schwarz et al. 1993; Schwarz et al. 1996). At low agent concentrations, thus, it is possible to control the degree of backscatter from the blood by adjusting the dose of contrast agent. Above a certain concentration, however, agent-induced attenuation will limit the effectiveness of further increases in concentration (de Jong 1997; Uhlendorf 1994). Agent-induced attenuation will be particularly significant when sound must be transmitted long distances through high concentrations of agent (e.g. when imaging the distal myocardium through the ventricles of the heart).

1.3.1.3 Nonlinear scattering

The scattering of sound from tissue is a linear process (Shung and Thieme 1993) that satisfies two conditions:

$$x\{a \cdot f_1(t)\} = a \cdot x\{f_1(t)\} \qquad 25$$

and

$$x\{f_1(t) + f_2(t)\} = x\{f_1(t)\} + x\{f_2(t)\}, \qquad 26$$

where $x\{f(t)\}$ is the response due to an input, $f(t)$, a is a constant, and $f_1(t)$ and $f_2(t)$ are time varying inputs. The first condition (Equation 25) states that scaling the input by a given amount scales the response by the same amount, but does not change the shape of the response. The second condition (Equation 26) says that the response due to a sum of two inputs is the sum of the individual responses. For linear scattering from tissue, if the incident sound pressure varies sinusoidally with time at a frequency, f, the scattered wave measured at any point in space will also vary sinusoidally with time at the same frequency (Morse and Ingard 1968).

When intensity of the incident sound is low and the induced oscillations in bubble radius are small ($\Delta R/R << 1$), the scattering of sound from gas microbubbles is also a linear process. The resonance calculations described in the previous section assume this condition. As the incident acoustic pressure amplitude is increased, however, scattering from a microbubble quickly becomes nonlinear, especially if the incident sound frequency is near the bubble's resonant frequency. The nonlinear nature of gas bubbles was first recognized and modeled mathematically by Lord Rayleigh (Rayleigh 1917). Subsequent workers have refined Rayleigh's model, producing models of increasing accuracy and complexity (Ayme-Bellegarda 1990; Leighton 1994; Plesset 1949; Poritsky 1951; Trilling 1952; Volkurka 1986). The fundamental nonlinearity in bubble scattering may be explained as follows: during the expansion phase of oscillation, a gas bubble's radius can increase by as much as several hundred percent ($\Delta R/R > 1$)

due to the high compressibility of the gas within. During the contraction phase of oscillation, the gas inside the bubble stiffens rapidly as the molecules are forced closer together, becoming less compressible and limiting the decrease in bubble radius. Because the bubble contains a finite mass of gas, the radius must always be greater than zero, and hence the fractional radius change during contraction must always be less than 100%. This pressure-dependent asymmetry in the radial response of the bubble creates a corresponding asymmetry in the scattered sound.

1.3.1.4 Harmonics, Subharmonics and Superharmonics

One of the effects of nonlinear scattering from near-resonant microbubbles is to introduce harmonic distortions into the scattered sound. If the incident sound contains components at a frequency, *f*, then the scattered sound will contain components not just at *f*, but also at higher harmonics (*2f*, *3f*, and so on). It is also possible for an oscillating bubble to generate subharmonics (*f/2*, *f/3*, *f/4*...) and ultraharmonics (*3f/2*, *5f/2*, *7f/2*...) of the incident sound frequency (Brennan 1995; Lauterborn 1976; Leighton 1994). For contrast agents under diagnostic imaging conditions, theoretical and experimental results show that the second harmonic component is almost always larger than all other components except the fundamental (Eatock and Johnston 1985; Morgan et al. 1997). While the pressure amplitude of the linear echo is proportional to the incident pressure, theory for single frequency insonation predicts that the pressure of the second harmonic echo will be proportional to the square of the incident pressure (Church 1995; Miller 1981).

1.3.1.5 Transient Scattering and Microbubble Disruption

Most contrast microbubbles require a shell or surfactant to stabilize them and prevent dissolution. When these agents are exposed to pulsed ultrasound at diagnostic pressures and frequencies, the bubbles can disrupt, producing echoes which decay in amplitude from pulse to pulse and disappear completely in times varying from microseconds to hundreds of milliseconds.

Figure 8 summarizes the results of an experiment in which diluted samples of stationary contrast microbubbles were exposed to 5-cycle tone bursts of pulsed ultrasound at 2.2 MHz (Burns et al. 1997).

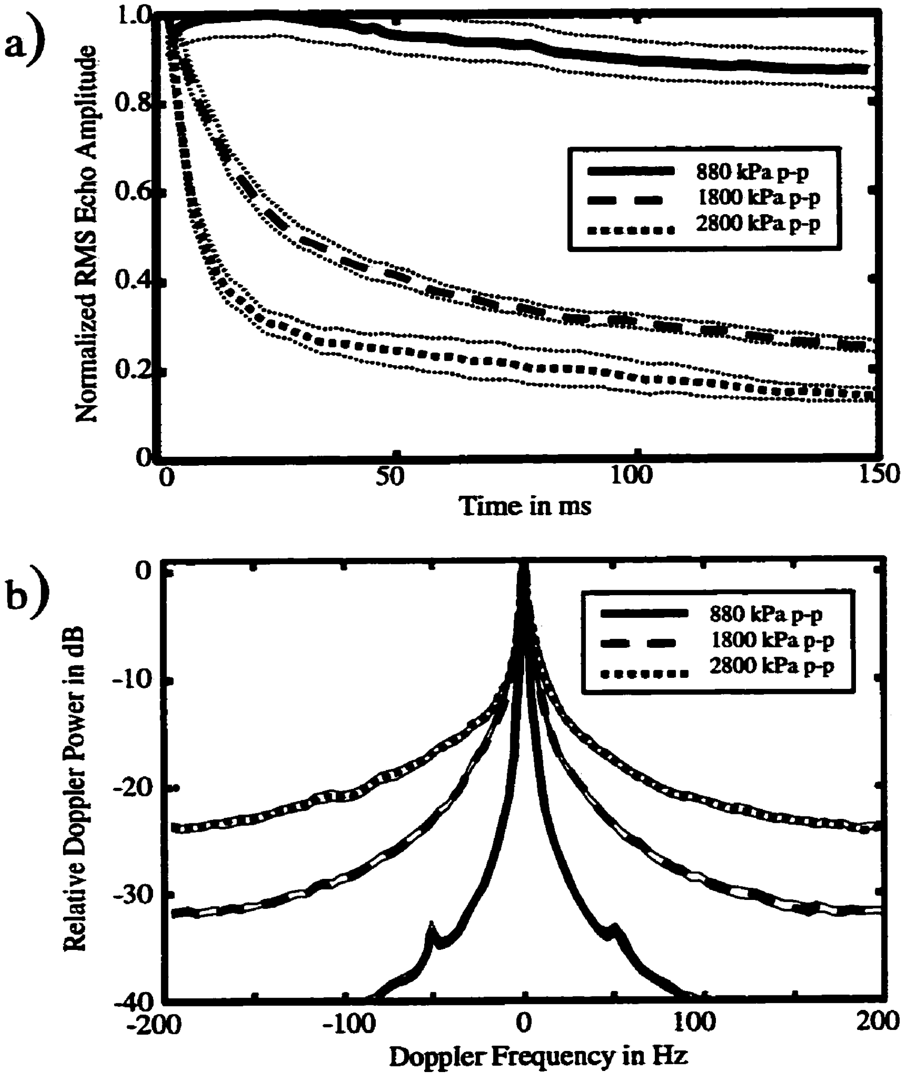

Figure 8: a) Normalized echo amplitude versus time after start of insonation for samples of SHU 563A insonated at different transmit pressures. In each case, the transmitted pulses were 5 cycle tone bursts at 2.2 MHz and the pulse repetition frequency was 2 kHz. b) Normalized Doppler spectra for the data shown in a). High intensity sound disrupts microbubbles, producing measurable Doppler shifts. The thin lines represent the standard error of the mean.

When the incident sound peak-to-peak pressure amplitude was 2.8 MPa (within the range of pressures used for diagnostic imaging), echoes from the air-filled, polymer-shelled agent Sonavist™ (Schering AG, Berlin) decayed rapidly over a period of 5-10 ms, after which time echo strength continued to decrease at a slower rate (Figure 8a). For lower incident pressures, the bubbles decayed progressively more slowly. This decay of microbubble echoes caused a corresponding broadening of the microbubble Doppler spectrum that was inversely proportional to the bubble lifetime in the sound beam (Figure 8b). A similar phenomenon, "transit time broadening", occurs in conventional Doppler ultrasound since moving blood spends only a limited time within the sound beam (Jensen 1996). When the same experiments were performed using the perfluoropropane-filled, albumin-shelled agent Optison, bubble lifetimes were on the order of 200 to 400 ms, and spectral broadening was measurable but reduced accordingly.

Experiments similar to the one described above have been performed on a wide range of different agents with qualitatively similar results, and a picture is emerging of the processes involved. Dayton et al. (Dayton et al. 1999b), who investigated disruption of isolated microbubbles using both optical and acoustic measurements, concluded that disruption occurred through a combination of mechanisms including:

1. **Gradual Gas Diffusion**: The initial sound pulse disrupts the shell and the gas within the bubble subsequently diffuses into the surrounding solution.
2. **Formation of a Defect, Escape of Gas**: The initial sound pulse creates a defect in the bubble through which the gas escapes and dissolves into solution.
3. **Microbubble Fragmentation**: The initial sound pulse breaks the bubble into a number of smaller free gas bubbles which dissolve into solution over the course of successive pulses.

4. **Rapid Destruction of a Bubble:** This is essentially an accelerated version of microbubble fragmentation in which shell fragments and gas are ejected rapidly from the bubble following the first incident pulse.

For Optison, these processes were observed to occur with increasing rapidity and severity according to incident acoustic pressure, starting with gradual diffusion at ~100 kPa. Time scales ranged from tens of seconds (for gradual diffusion) to tens of milliseconds (for fragmentation) and could be prolonged by increasing perfluoropropane concentrations in the surrounding fluid.

Due to the complex nature of microbubble disruption and the varied nature of microbubble shells and sizes, few quantitative models exist to describe these mechanisms. Models of the passive diffusion of gas from a free gas bubble indicate that the diffusion process is dependent upon many factors including: gas density; gas diffusivity, solubility, and starting concentration in the surrounding fluid; surface tension; ambient pressure; temperature, and bubble radius (Epstein and Plesset 1949; Leighton 1994). Shell properties and blood surfactants will also affect gas diffusion from contrast microbubbles *in vivo*.

1.3.1.6 Cavitation and Bioeffects

Whenever a physical probe such as sound is used to interrogate the body, safety should always be considered. In particular, the interaction of sound with gas-filled cavities is known to produce measurable biological effects ("bioeffects") under some conditions (Barnett 1998). These conditions and their relevance to ultrasound contrast imaging are reviewed below.

The formation, growth and collapse of a gas cavity in fluid as a result of ultrasound exposure, commonly called *cavitation*, was studied intensively even prior to the development of microbubble contrast agents (Brennan 1995). In fact, most of the mathematical models used to describe contrast microbubbles were originally developed to model cavitation (Plesset 1949; Poritsky 1951; Rayleigh 1917). When sound waves of sufficient intensity travel through a fluid, the rarefactional half-cycle of the sound wave can actually tear the fluid apart, creating spherical cavities within the fluid. The subsequent rapid collapse of these cavities during the compressional half cycle of the sound wave can focus large amounts of energy into a very small volume, raising the temperature at the centre of the collapse to thousands of degrees Kelvin, forming free radicals, and even emitting flashes of light (sonoluminescence) (Apfel 1997; Leighton 1994; Riesz et al. 1985; Riesz and Christman 1986; Suslick 1989).

Concern over potential cavitation-induced bioeffects in diagnostic ultrasound has lead to the development of several indices to describe the relative likelihood of cavitation from clinical instruments (Apfel and Holland 1991). The most commonly used index, the Mechanical Index (MI), is

$$MI = \frac{p_{neg}}{\sqrt{f}} \tag{27}$$

where p_{neg} is the peak rarefactional pressure of the incident sound in MPa, and f is the frequency in MHz (Leighton 1994). This index, related to the amount of mechanical work that can be performed on a bubble during a single negative half cycle of sound (Apfel and Holland 1991), is now displayed on the monitors of most clinical ultrasound systems. Reported values of MI from clinical systems range from approximately 0.1 to 1.9. With the exception of one study which showed cavitation-induced hemorrhage in mouse lung (Child et al. 1990), no evidence of bioeffects from conventional imaging at these levels have been reported.

Several groups have performed experiments to assess whether the presence of contrast microbubbles can act as cavitation seeds, potentiating cavitation-induced bioeffects (Everbach et al. 1998; Holland et al. 1992; Miller et al. 1997; Miller and Thomas 1995; Miller et al. 1991; Miller et al. 1996; Williams et al. 1991). While almost all of these groups have shown that adding contrast agents to blood increased cavitation effects (e.g. peroxide formation, acoustic emissions) and related bioeffects (e.g. hemolysis, platelet lysis), all significant bioeffects occurred with either very high agent concentration, sound pulse duration or MI, or with decreased hematocrit (Fowlkes and Holland 2000). In experiments in which clinically relevant values of these parameters were used (agent concentration <0.2 %, pulse duration <2 μs, MI< 1.9, hematocrit ~ 40-45%), no significant bioeffects have been reported (Miller et al. 1997; Uhlendorf and Hoffman 1994). Such results suggest that contrast imaging should not produce significant bioeffects provided that the transmit intensities used (as measured by the mechanical index), are no larger than those used at present. These results are preliminary, and more work is required to monitor the safety of microbubble imaging techniques. Using as low a mechanical index as possible, and minimizing ultrasound exposure, the margin of safety can be maximized (Barnett 1998; Fowlkes and Holland 2000).

The acoustic behaviour of microbubble contrast agents as a function of MI is summarized in Figure 9.

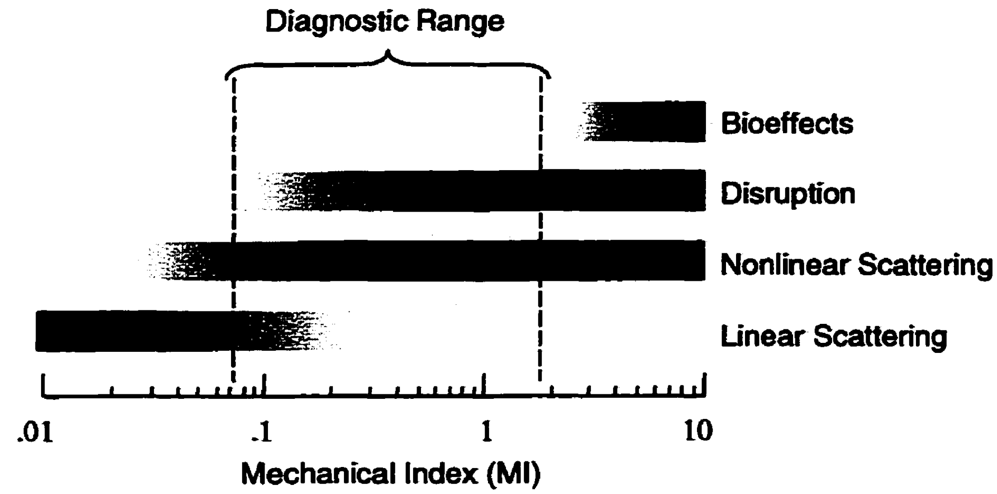

Figure 9: The acoustic response of microbubble contrast agents to pulsed ultrasound at diagnostic frequencies varies according to the mechanical index (MI). At the low end of the diagnostic range (MI = 0.05 to 0.1), most agents already exhibit signs of nonlinear scattering, but few are disrupted significantly. At the high end of the diagnostic range (MI=1.1 to 1.9), almost all agents are highly nonlinear and disrupt quickly. Significant bioeffects have been detected above the range of mechanical indices used diagnostically.

1.4 Existing Techniques for Microbubble Imaging

The goal of this work is to study and improve techniques for detecting and imaging contrast microbubbles in the presence of tissue. Because existing Doppler ultrasound techniques are capable of detecting blood flow in larger vessels, interest is focussed on detecting microbubbles in terminal arterioles, capillaries and venules where blood cannot be detected by other means. The following sections review the techniques that currently exist for detecting microbubble contrast agents *in vivo*.

1.4.1 Conventional Greyscale Imaging

Conventional greyscale imaging is poorly suited to the detection of microbubble contrast agents. In conventional imaging, sound is transmitted and received over the same band of frequencies, usually comparable to the bandwidth of the transducer. Because almost all of the energy scattered from tissue lies in this frequency range, the echoes from small quantities of microbubbles will be masked by strong echoes from tissue. For instance, blood occupies approximately 8 to 14% of the volume of the myocardium (Kassab et al. 1994a). Because the backscatter from blood is 100 to 500 times weaker than tissue (Jensen 1996; Shung et al. 1976; Shung and Thieme 1993), the blood backscatter must be increased by a factor of roughly 1000 to 5000 (30-37 dB) before the scattering from blood is even comparable the scattering from the myocardium. While current contrast agents can achieve this level of enhancement at high doses (subject to attenuation), fundamental greyscale imaging is inefficient and now is seldom used for contrast imaging.

1.4.2 Harmonic Imaging

Miller first suggested the use of second harmonic emissions to detect resonant bubbles in 1981 (Miller 1981). In harmonic detection, sound is transmitted at one frequency, f_o, and the echoes are detected at the second harmonic of the transmit frequency, $2f_o$. Because resonant bubbles are nonlinear scatterers, they will generate detectable echoes at $2f_o$, whereas the linear echoes from tissue will be concentrated at the fundamental, f_o, and can be eliminated by suitable filters. For comparable backscatter at the transmit frequency, contrast agents can scatter up to 15 to 20 dB more energy at the second harmonic than linear scatterers such as cellulose or tissue (Figure 10).

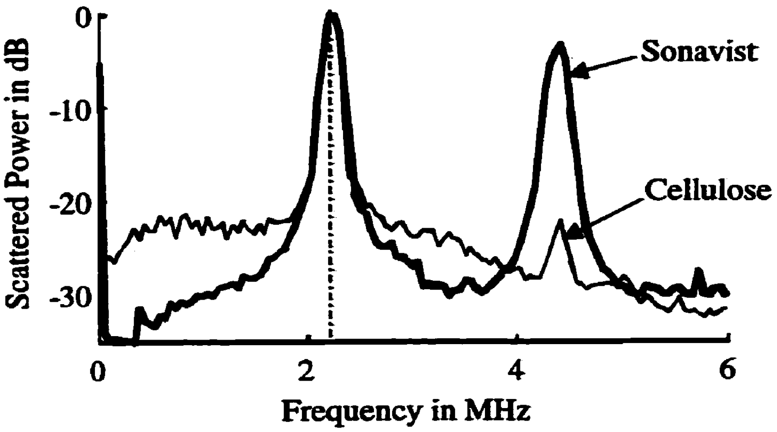

Figure 10: Echo spectra of the contrast agent Sonavist and linear scattering cellulose particles following insonation at 2.2 MHz and 600 kPa. Contrast agents can scatter 15 to 20 dB more energy at the second harmonic than linear scatterers.

Harmonic detection, combined with pulsed wave and colour Doppler, was first used to detect and image microbubble contrast agents *in vivo* in 1992 by Burns et al. (Burns et al. 1992), who demonstrated that clutter could be reduced significantly with this method, enhancing agent detection. Harmonic detection was subsequently applied to power Doppler and greyscale imaging techniques (Burns 1996; Burns et al. 1994; Burns et al. 1996). Both of these latter techniques are now used extensively for ultrasound contrast imaging, and are available on many clinical imaging systems. To provide a given level of myocardial enhancement, harmonic imaging would require less than 1/30th the dose of microbubbles that would be required in conventional greyscale imaging[4].

1.4.3 Transient Power Doppler Imaging

Power Doppler imaging using high intensity transmit pulses (at MIs above 1.0) is the most sensitive technique currently available for detecting and imaging microbubble contrast agents in the microcirculation. Uhlendorf (Uhlendorf and Hoffman 1994) first showed that the high intensity pulses transmitted with this technique can disrupt microbubbles, producing transient Doppler that shifts that can be used to distinguish microbubbles from tissue, even when both are stationary. The cut-off frequency of the Doppler clutter filter should be chosen so that echoes from stationary and moving tissue are suppressed while the high Doppler frequency echoes from disrupting microbubbles are detected. Power Doppler imaging is commonly combined with harmonic detection in an attempt to reduce further the amount of signal detected from tissue.

Because all the microbubbles within the scan plane are disrupted each time an image is made, sufficient time must be allowed between images for blood to reperfuse the entire thickness of the scan plane. For example, if 5 mm of a vessel lie within the scan plane and the blood velocity is 1 mm/s, it will take 5 seconds for the vessel segment to be fully refilled with agent. Because of this, electrocardiogram-triggered (ECG-triggered) imaging is commonly used to detect perfusion in the myocardium, at typical rates of one image frame per 3 to 8 heartbeats (Porter and Xie 1995; Porter et al. 1996).

1.4.4 Microbubble Contrast Imaging in Cardiology

Since the first reports of microbubble contrast effects in 1968 (Gramiak and Shah 1968), the development of clinical applications of contrast techniques has been ongoing. These applications may be subdivided into two classes: those that do not require contrast agents that pass through the lungs and those that do.

Prior to the introduction of Albunex, all contrast effects were short lived since microbubbles were removed by the lungs or disolved rapidly. One of the first applications of microbubbles was for the detection of intracardiac shunting (Fowlkes and Holland 2000). Intravenous injections of agitated saline or dextrose were administered and the appearance of microbubbles in the left heart was used to identify right-to-left shunting (these bubbles would otherwise have been filtered by the lungs). In the early 1980's experiments in dogs showed that it was possible to assess myocardial perfusion by injecting gelatin-encapsulated microbubbles directly into the coronary arteries and measuring changes in fundamental greyscale image intensity (Armstrong et al. 1982). Subsequent experiments with intracoronary and aortic root injections of microbubbles have shown that such Myocardial Contrast Echocardiography (MCE) can be used to quantify infarct volumes (Linka et al. 1997) and to assess myocardial viability (Villanueva et al. 1996). Areas of microvascular obstruction as assessed by contrast echocardiography correlate with histological measurements and measurements by other imaging techniques such as MRI and SPECT (Kaul et al. 1997; Wu et al. 1998a). Intracoronary injections of contrast microbubbles in humans have been used experimentally to identify regions of intact microvasculature, hibernating myocardium, and risk areas following acute myocardial infarction (Ito et al. 1993; Nagueh et al. 1997; Ragosta et al. 1994). Because direct intracoronary injections of microbubbles can produce high microbubble concentrations in the myocardium and because no microbubbles are present within the ventricles to cause attenuation, these techniques can be performed successfully with greyscale imaging (although harmonic imaging provides superior contrast (Firschke et al. 1997)). While their invasive nature makes intracoronary injections less

---

[4] Signal power is proportional to agent concentration and 15 dB represents a factor of 31.6 in power.

desirable for routine use, these experiments have prompted widespread interest in measuring myocardial perfusion with transpulmonary contrast agents following intravenous injection.

With the introduction of Albunex and other contrast agents capable of passing through the pulmonary circulation, it became possible to detect microbubbles routinely in the left heart following intravenous injection. The first clinically approved application of these transpulmonary agents was to opacify the left ventricle. Filling the left ventricle with microbubbles improves detection of the endocardial border and has been shown to increase diagnostic accuracy in "difficult" patients who cannot be imaged successfully with conventional ultrasound due to imaging artifacts (Cohen et al. 1998; Feinstein et al. 1990; Grayburn et al. 1998). For this application, harmonic imaging has been shown to provide better contrast than conventional greyscale imaging.

Studies have been conducted to determine whether or not myocardial perfusion can be detected routinely following intravenous injections of contrast microbubbles. Using intermittent harmonic imaging and intravenous injections of the contrast agent Optison (Mallinckrodt, St Louis) with pharmacological stress testing, Kaul et al. showed a 92 % concordance between segmental myocardial perfusion scores measured with microbubbles and with ^{99m}Tc-Sestamibi SPECT imaging (Kaul et al. 1997). Conversely, Marwick et al. using similar imaging without stress testing in a large multi-centre trial of the agent NC100100 reported much lower sensitivity and specificity compared with SPECT imaging (Marwick et al. 1998)[5]. When real time imaging was used in the NC100100 trial, results were much worse and technical feasibility (the percentage of interpretable segments) was below 50 %. While it now appears clear that

---

[5] Comparison of these two trials suggests that the NC100100 trial lacked a clearly defined imaging methodology.

intermittent power Doppler techniques are more sensitive than harmonic greyscale imaging (Becher et al. 2000), no large scale clinical trial results have been conducted with this technique. In summary, while results from some centres show promise, more work is required to perfect imaging techniques and methodologies before perfusion imaging becomes feasible for widespread use (De Maria et al. 1998). Although a technique is needed to provide the simultaneous real time examination of both myocardial perfusion and regional wall motion (Main and Garyburn 1999), myocardial perfusion has not been demonstrated in real time with either harmonic or Doppler imaging.

1.4.5 Limitations of Existing Techniques:

1.4.5.1 Harmonic Detection

Harmonic detection involves an inherent tradeoff between contrast and imaging resolution (Powers et al. 1997)(Figure 11): if the transmit pulse bandwidth (centred about f_o) and the receive filter passband (centred about $2f_o$) overlap, then the linear echoes from tissue will be detected in the harmonic signal. Such echoes reduce agent to tissue contrast and can mask the nonlinear echoes from small quantities of agent, especially at low incident intensities when nonlinear scattering is weak. To increase contrast, the transmit and receive bandwidths must be narrowed, degrading axial resolution. This tradeoff currently limits both the contrast and resolution of harmonic imaging techniques, particularly in situations where *in situ* concentrations of agent or incident sound intensities are limited. The compromised resolution of harmonic imaging limits its ability to image small vessels, such as those supplying the myocardium and vascularized tumours.

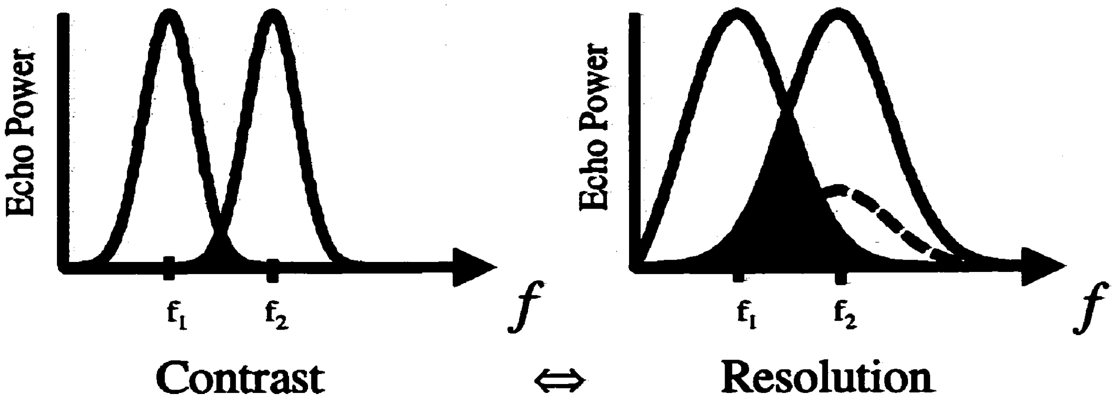

Figure 11: Overlap between the transmit and receive passbands results in unwanted signal in harmonic mode (shaded areas), creating a fundamental tradeoff between contrast and resolution. This tradeoff is especially severe when the harmonic echoes are weak (right, dotted line).

Because of its reduced contrast at low transmit intensities, harmonic imaging is commonly performed at high transmit intensities (MI>1.0) where microbubble disruption is rapid and imaging frame rates must be reduced significantly to maintain detection sensitivity (Porter et al. 1996). The power-dependent contrast of harmonic imaging also leads to variations in agent-to-tissue contrast with depth and transmit focus.

At high transmit intensities, harmonic imaging encounters yet another problem: harmonic echoes detected from tissue can mask the bubble harmonics, reducing contrast. These "tissue harmonics" are generated not by nonlinear scattering (as with microbubbles), but by nonlinear distortion of the transmitted sound as it travels through tissue followed by linear scattering from tissue (Averkiou and Hamilton 1995; Hamilton and Blackstock 1998). The origins of tissue harmonics and their influence on diagnostic imaging are discussed in more detail in Chapter 5.

1.4.5.2 Transient Doppler Detection

Transient Doppler detection also has drawbacks. The low frame rates required to achieve contrast prolong exam times and reduce the number of images that can be acquired with a given dose of contrast media. Because the rate of microbubble disruption is a strong function of the intensity of the incident sound (Section 1.3.1.5), detection sensitivity will vary with depth in the imaging plane, even more so than in harmonic imaging. Because radio frequency and Doppler spectra of microbubble echoes vary with bubble properties and acoustic conditions, Doppler filters must be optimized for each combination of agent conditions, complicating system design.

1.5 Outline of this Thesis

In the following chapters, techniques are introduced which overcome some of the limitations of existing contrast imaging techniques, and which should facilitate the clinical use of ultrasound contrast agents for detecting myocardial perfusion.

In Chapter 2, a new microbubble detection technique called pulse inversion Doppler (PID) is introduced. Data from experiments performed *in vivo* are used to compare PID with fundamental and harmonic Doppler techniques and identify potential benefits of PID detection. This work was first presented at the 1997 IEEE Ultrasonics Symposium (Toronto)(Hope Simpson and Burns 1997), and was later published in the IEEE Transactions on Ultrasonics, Ferroelectrics and frequency control (Hope Simpson et al. 1999). Parts of this work have been submitted for patent protection with the U.S. and European patent offices (Burns and Hope Simpson 1998).

In Chapter 3, a method is described for designing radio frequency and Doppler filters for detecting and imaging microbubble contrast agents in the microcirculation which exploits direct measurements of the echoes from contrast agents and tissue. To demonstrate its application, this method is used to design Doppler and pulse inversion Doppler filters for myocardial perfusion. The text of Chapter 3 is condensed from a paper submitted for publication in the IEEE Transactions on Ultrasonics, Ferroelectrics and Frequency Control. Work on pulse inversion Doppler perfusion imaging was first presented at the 3rd ThoraxCentre European Contrast

Symposium (Rotterdam, 1998), where it received the Young Investigator's Award (Hope Simpson and Burns 1998b).

Chapter 4 uses the techniques outlined in Chapter 3 to assess the power dependence of Doppler, pulse inversion Doppler and harmonic imaging for detecting myocardial perfusion in anaesthetized dogs. The low power performance of pulse inversion Doppler is examined in detail, and the potential for real time perfusion imaging with PID is demonstrated. This Chapter expands upon work first presented at the 1998 IEEE Ultrasonics Symposium (Sendai, Japan) (Hope Simpson and Burns 1998a) and has been submitted for publication in Ultrasound in Medicine and Biology (Hope Simpson et al. 2000).

Chapter 5 covers several important applications of pulse inversion Doppler imaging. Intermittent and real-time myocardial perfusion imaging, quantification of myocardial blood flow, imaging of blood flow in hepatic masses, and nonlinear tissue imaging are discussed. The section on quantification of blood flow contains work performed in collaboration with Dr. P. N. Burns, and presented by Dr. Burns at the 5th Heart Centre European Contrast Symposium, (Rotterdam, 2000) (Burns et al. 2000b). This chapter also includes work from a recent collaborative paper on liver imaging (Burns et al. 2000c), and an invited paper on nonlinear imaging (Burns et al. 2000a).

In Chapter 6, the significance of the present work and the future of ultrasound contrast imaging are discussed.

2 Pulse Inversion Doppler

This Chapter originally appeared in print as: Hope Simpson, D., Chin, C. T., and Burns, P. N. Pulse Inversion Doppler: A New Method for Detecting Nonlinear Echoes from Microbubble Contrast Agents. IEEE Transactions on Ultrasonics, Ferroelectrics and Frequency Control 1999; 49(2):372-382. It is reprinted here with permission. Some sections have been edited for clarity.

The simulations of microbubble scattering presented in Figures 15 and 16 of this Chapter are the work of Chien Ting Chin from the Department of Medical Biophysics, University of Toronto.

2.1 Overview

In the first Chapter, microbubble contrast agents and the principal methods of imaging these agents with ultrasound were described. Almost all clinical applications of ultrasound contrast agents rely on, and are limited by, our ability to detect microbubbles in the presence of tissue. Two acoustic properties of microbubbles, nonlinear scattering and disruption, have been used to distinguish microbubbles from tissue. Power Doppler exploits disruption effects to detect microbubbles and therefore requires intermittent imaging and high incident sound intensities for sensitivity. Harmonic imaging, which exploits nonlinear scattering, suffers from tradeoffs between resolution and contrast that limit its effectiveness, especially at low incident sound intensities, so that it too must requires high incident sound intensities and intermittent imaging.

In this chapter, a new detection method, pulse inversion Doppler (PID), is introduced which detects nonlinear scattering with Doppler methods, overcoming the resolution/contrast tradeoffs of harmonic imaging. Pulse inversion Doppler also exploits disruption effects to match the performance of power Doppler at high transmit levels.

2.2 Theory

As outlined in Chapter 1, the nonlinear scattering from microbubbles is caused by their asymmetric response to the high and low pressure portions of a sound wave. This asymmetric response generates harmonics of the incident sound which are detected in harmonic imaging. Unfortunately, harmonic detection cannot separate nonlinear harmonic echoes from linearly scattered sound at the same frequency. Pulse inversion provides a direct technique for detecting and segmenting the asymmetric components of scattered echoes from the linearly scattered echoes.

2.2.1 Pulse Inversion Detection

Consider a two pulse transmit sequence in which a pulse of sound is transmitted into tissue and, after a suitable delay *T*, a second pulse is transmitted which is an inverted copy of the first pulse. Assuming linear sound propagation, we can write:

$$p_2(\bar{r},t)=-p_1(\bar{r},t), \qquad 28$$

where $p_1(\bar{r},t)$ and $p_2(\bar{r},t)$ represent the acoustic pressure of the first and second pulses as a function of position, $\bar{r}$, and time from the start of transmission, t. If the received echoes from these two pulses are

$$e_1(t)=Echo\{p_1(t)\} \qquad 29$$

$$e_2(t)=Echo\{p_2(t)\}, \qquad 30$$

where $Echo\{p(t)\}$ represents the echo produced by an incident pulse $p(t)$, then the following pulse inversion detection signals may be formed (Figure 12):

$$s(t)=e_1(t)+e_2(t) \qquad 31$$

$$d(t)=e_1(t)-e_2(t) \qquad 32$$

For any scattering processes satisfying

$$Echo\{-p(t)\}=-Echo\{p(t)\}, \qquad 33$$

which includes all linear scattering, the sum signal, $s(t)$, will be zero provided that the scatterer doesn't move relative to the transducer between pulses. For all other types of scattering, including nonlinear scattering from microbubbles, $s(t)$ will be non-zero.

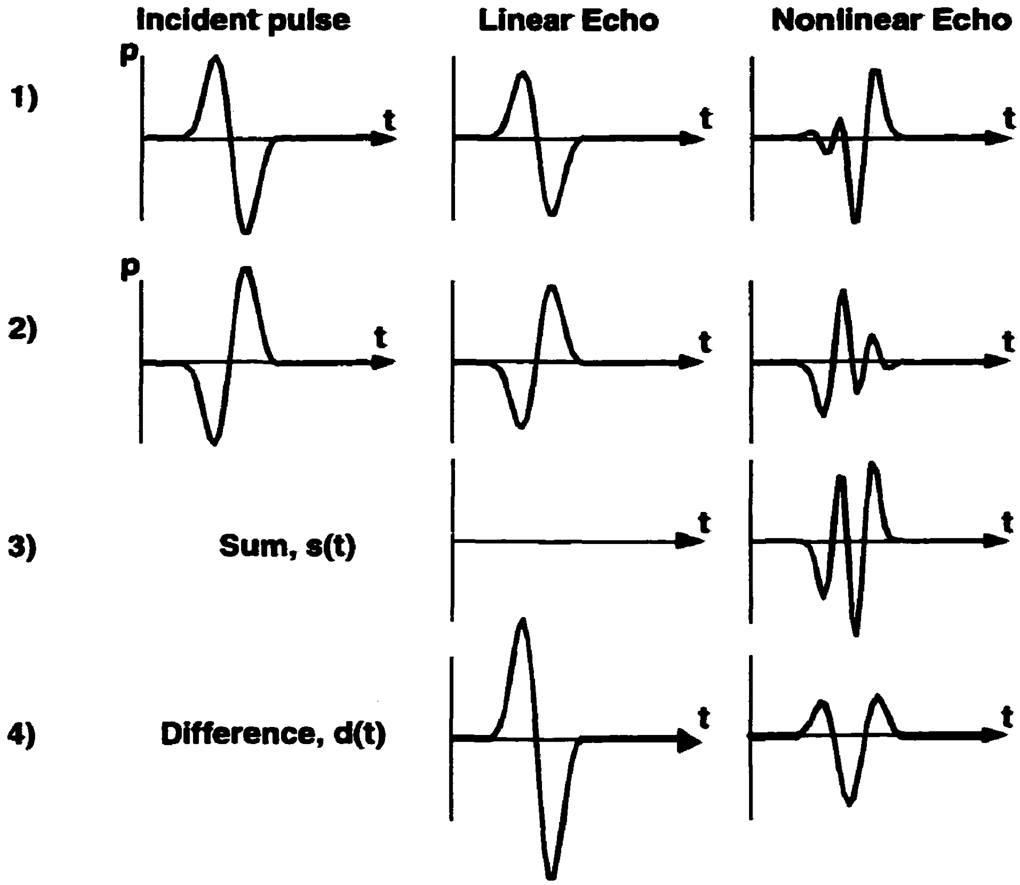

Figure 12: Principles of pulse inversion detection: 1) a pulse of sound is transmitted and echoes are detected from linear and nonlinear scatterers; 2) an inverted copy of the same pulse is transmitted and the echoes are detected; 3) The two echoes are summed; 4) The two echoes can also be subtracted. The sum, s(t) *is nonzero only for nonlinear scattering.*

2.2.2 Predicted Frequency Response

Assuming a simple memoryless model of nonlinear scattering from a point target, based upon a power series expansion of the returned echo,

$$Echo\{p(t)\}=\sum_{m=0}^{\infty}a_m p^m(t-t_d), \qquad 34$$

where t_d is a time delay, and the a_m are the coefficients of the expansion, we obtain

$$s(t)=\sum_{m=0}^{\infty}a_{2m}p^{2m}(t-t_d) \qquad 35$$

$$d(t)=\sum_{m=0}^{\infty}a_{2m+1}p^{2m+1}(t-t_d). \qquad 36$$

If the transmitted pressure, $p(t)$ is a sinusoid at frequency f_o, it can be shown through the use of trigonometric identities that the even order terms in $p(t-t_d)$ give rise to even harmonics of f_o and the odd order terms in $p(t-t_d)$ give rise to odd harmonics of f_o. Pulse inversion detection therefore decomposes the returned echoes into $s(t)$ which contains only even order harmonics of the transmitted signal, and $d(t)$ which contains only odd order harmonics of the transmitted signal. When the difference, $d(t)$, is dominated by the linear term, $a_1 p(t-t_d)$, then the quotient $s(t)/d(t)$ will represent the ratio of (even order) nonlinear to linear scattering. This ratio should be much greater for echoes from contrast media than for echoes from linear tissue (for which it ideally should be zero). If, in addition, the sum, $s(t)$, is dominated by $a_2 p^2(t-t_d)$, then:

$$\frac{s(t)}{d^2(t)}\approx\frac{a_2}{a_1} \qquad 37$$

Pulse inversion detection may thus be used to quantify fundamental properties of nonlinear scattering.

Several imaging systems exploiting pulse inversion detection or variants of this technique are currently being developed for clinical use (Mattrey et al. 1998--see Chapter 6).

2.2.3 Pulse Inversion Doppler

While pulse inversion detection using the sum signal, $s(t)$, can detect the nonlinear echoes from microbubbles and suppress the linear echoes from stationary tissue, echoes from moving tissue will not be suppressed completely and could mask echoes from microbubbles.

Pulse inversion detection and Doppler detection can be combined in a technique, *pulse inversion Doppler* which exploits the advantages of both detection schemes and which can overcome the problem of tissue motion. In pulse inversion Doppler (PID), a series of N ultrasound pulses are transmitted at a pulse repetition interval of T seconds. Unlike conventional Doppler, each transmitted pulse is an inverted copy of the previous pulse. Assuming linear sound propagation, we can write:

$$p_k(\bar{r},t) = (-1)^k p_0(\bar{r},t), k \in [0, N-1] \qquad 38$$

The corresponding echoes, $e_k(t)$, are received by the transducer and demodulated by mixing them in quadrature with a carrier at a frequency, f_c, typically chosen either near the centre of the transducer passband (for broadband transmit pulsing), or at the second harmonic of the transmit frequency (for narrowband transmit pulsing). The demodulated signals are then processed using conventional Doppler processing to produce a Doppler spectrum.

For linear scattering structures, successive echoes will be of the form:

$$e_{k+1}(t) = -e_k(t - \Delta\tau_d), \qquad 39$$

where $\Delta\tau_d = 2\Delta d / c_{sound}$ is a time delay due to an axial motion, Δd, of the scattering structure relative to the transducer between pulses (c_{sound} is the speed of sound in the medium). The corresponding phase shift between successive echoes, measured relative to f_c, will be:

$$\Delta\phi = 2\pi f_c \Delta\tau_d + \pi \qquad 40$$

The additional π term is a consequence of the negative sign in front of e_k in Equation 39.

The estimated Doppler frequency will thus be:

$$f_d = \frac{\Delta\phi}{2\pi} f_{pr} = \frac{2v}{c_s} f_c + \frac{1}{2} f_{pr}, \quad 41$$

where v is the relative axial velocity of the scatterer with respect to the transducer, and $f_{pr} = 1/T$ is the pulse repetition frequency (PRF). Since the conventional Doppler shift for this situation is given by

$$f_d = \frac{2v}{c_s} f_c, \quad 42$$

the signals from linear scatterers will appear shifted in the Doppler spectrum by an amount equal to half the Doppler pulse repetition frequency.

Again, echoes received from nonlinear scattering can be decomposed into odd and even components as follows :

$$Echo\{p(t)\} = e_{even}(t) + e_{odd}(t) \quad 43$$

$$Echo\{-p(t)\} = e_{even}(t) - e_{odd}(t), \quad 44$$

where $Echo\{p(t)\}$ represents an echo from a normal transmitted pulse $p(t)$, and $Echo\{-p(t)\}$ represents an echo from an inverted transmit pulse. For successive PID echoes, the odd component ($e_{odd}(t)$) changes sign with $p(t)$, but the even component ($e_{even}(t)$) does not. This decomposition is general and does not rely on the exact nature of the scattering process.

The Doppler shifts due to these two components are:

$$f_{d,odd} = \frac{2v}{c_s} f_c + \frac{1}{2} f_{pr} \quad 45$$

$$f_{d,even} = \frac{2v}{c_s} f_c \quad 46$$

Note that the even component has a Doppler shift identical to that produced by conventional Doppler.

Providing all scatterer velocities obey the revised Nyquist limit:

$$\frac{2|v_{\max}|}{c_s} f_c \le \frac{1}{4} f_{pr}, \qquad 47$$

which is half of the conventional limit, the portion of the Doppler spectrum between $-f_{pr}/4$ and $f_{pr}/4$ will contain only Doppler signals arising from nonlinear scattering processes (this will be referred to as the low frequency or nonlinear portion of the spectrum). The remaining half of the Doppler spectrum (which will be referred to as the high frequency or linear portion) will contain Doppler signals arising from both linear scattering and possibly higher order nonlinear scattering (Figure 13).

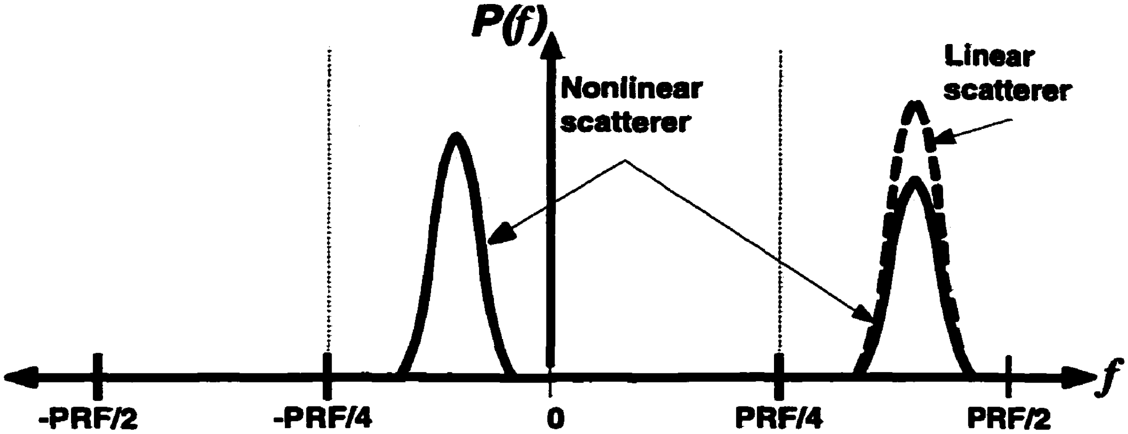

Figure 13: Theoretical pulse inversion Doppler spectra for linear scatterers (dotted line) and nonlinear scatterers (solid lines) moving at the same velocity.

Pulse inversion detection can be considered as a limiting case of pulse inversion Doppler in which only two pulses are transmitted down a given line of sight, resulting in a Doppler spectrum with only two frequency components. The sum signal, $s(t)$, is equivalent to the low frequency component of the Doppler spectrum and the difference signal, $d(t)$ is equivalent to the high frequency component. Tissue motion will cause a portion of the linear tissue signal to appear in the low frequency component, blurring the separation between linear and nonlinear echoes.

2.2.4 Power and Colour Doppler Imaging

The principles of pulse inversion Doppler are readily applicable to colour and power Doppler imaging. For these techniques, every second pulse transmitted down each line of sight is inverted. When the received echoes are detected, Doppler frequencies greater than $PRF/4$ can be removed using suitably modified wall filters, and all existing spectral estimation techniques can then be applied, including recently developed broadband colour Doppler techniques (Ferrara et al. 1996; Loupas et al. 1995). Novel processing strategies such as displaying the ratio of power in the nonlinear portion of the spectrum to power in the linear portion may also have useful applications. Equation 37 could be used as the basis of a technique for measuring the relative efficiency of nonlinear scattering.

2.3 Methods

2.3.1 Contrast Agents

Two contrast agents were used: Sonavist (Schering Ag, Berlin) is a polymer shell air agent; Optison (Mallinckrodt Medical, Inc., St. Louis) is a protein shell perfluorocarbon agent. Both have been shown to scatter in the linear and nonlinear range at diagnostic incident pressures. Cellulose particles (Sigma Cell Type 20, Sigma Chemical Co., St. Louis), were used as control linear scatterers.

2.3.2 Modeling

A modified Trilling model of microbubble scattering (Chin and Burns 1997) was used to predict the frequency response of pulse inversion detection for a realistic population of gas microbubbles modeled upon the contrast agent Optison. Neither the effects of nonlinear sound propagation nor the effects of bubble/shell disruption were included in these simulations. Radio frequency spectra of echoes from normal and inverted transmit pulses were generated, together with the spectra of the pulse inversion signals, $s(t)$ and $d(t)$. These spectra were compared with spectra generated from a best fit to the power series expansion of Equation 34.

2.3.3 Experiment

In vitro experiments were designed to compare the performance of pulse inversion Doppler against harmonic Doppler and conventional Doppler as a technique for separating moving linear scatterers from moving nonlinear scatterers. Apparatus was constructed as shown in Figure 14. Doppler ultrasound pulses were generated using an arbitrary waveform generator (AWG 2020, Sony/Tektronix, Japan) amplified by an RF power amplifier (model 240L, ENI, Rochester) and applied to a 3.5 MHz focused cylindrical transducer (3.5 6-20 Series L, Picker International Inc., Highland Heights, Ohio). The transducer was mounted in a water bath, and aimed at a latex tube containing flowing contrast agent (flow velocity was adjusted so that the highest detected Doppler shifts satisfied the revised Nyquist limit (Equation 47)). Echoes were detected by the transducer, amplified (AU 4A -150 amplifier, Miteq), filtered using a custom filter (0.5-8 MHz 4 pole Butterworth), and recorded on a digital oscilloscope (Lecroy 7200, Lecroy Corporation, Chestnut Ridge, New York) with 8-bit resolution. Sampling on the oscilloscope was synchronized to the waveform generator clock output to minimize random phase errors (jitter) in the Doppler signals. Diode expanders and limiters were used respectively to eliminate low noise from the transmit amplifier and to protect the receive amplifier. A variable attenuator placed in front of the receive amplifier was used to control receive gain. Digitized echoes were processed offline on a computer workstation.

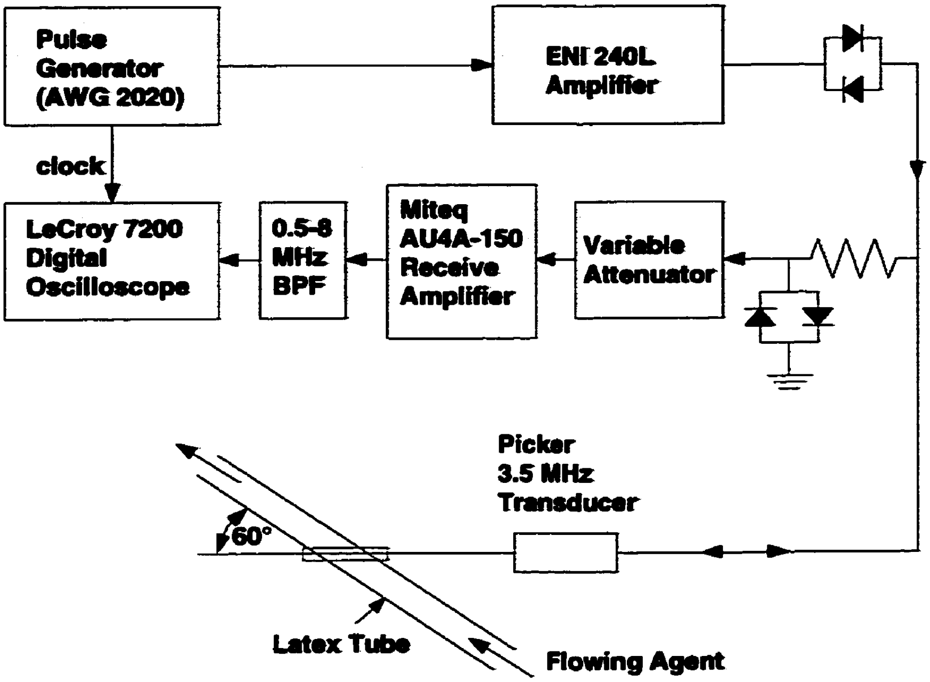

Figure 14: Schematic of experimental apparatus.

Doppler data were acquired from contrast agent suspensions flowing through the latex tube using both conventional (non-inverting) and inverting pulsing at a Doppler PRF of 4 kHz. The one-way propagation distance between the transducer and the centre of the latex tube was approximately 43 mm. Transmit tone bursts of 1 cycle at 3 MHz, 2 cycles at 2.2 MHz and 5 cycles at 2.2 MHz were tested at peak to peak pressures ranging from 50 kPa to 1.5 MPa. These pulses are of similar frequency, duration and intensity to those used clinically for contrast imaging. All experiments were repeated on control solutions of cellulose particles.

2.3.4 Quantification of Contrast

For quantitative comparisons, agent to cellulose contrast was defined as:

$$C_{a,c} = \int_{-f_{pr}/4}^{f_{pr}/4} P_{agent}(f)df \Bigg/ \int_{-f_{pr}/4}^{f_{pr}/4} P_{cellulose}(f)df, \tag{48}$$

where $P(f)$ is the Doppler power spectral density after subtraction of the stationary echoes.

2.4 Results

2.4.1 Modeling

Predicted spectra from a linearly propagated, symmetric 4 cycle tone burst at 2.9 MHz are shown in Figure 15 and Figure 16, for peak to peak incident pressures of 50 kPa and 500 kPa respectively. In each case, results from Equation 34 are calculated using a best fit to the Chin bubble model spectra from a single transmit pulse. While the predictions of the bubble model and Equation 34 agree well at transmit intensities below 100 kPa (Figure 15), the bubble model predicts significant broadening in all spectra at higher transmit (Figure 16). This spectral broadening is not predicted by a best fit to Equation 34.

Such modeling suggests that, for maximum sensitivity, pulse inversion detection should be combined with harmonic detection when narrowband transmit pulses are used. In this mode, significant contrast gains over harmonic imaging are predicted, since the linear scattering from tissue at the second harmonic is entirely cancelled. At high transmit pressures, receive filters should be adjusted to take full advantage of the predicted spectral broadening, particularly since such broadening is not predicted for either system or propagation nonlinearities (Hamilton 1998).

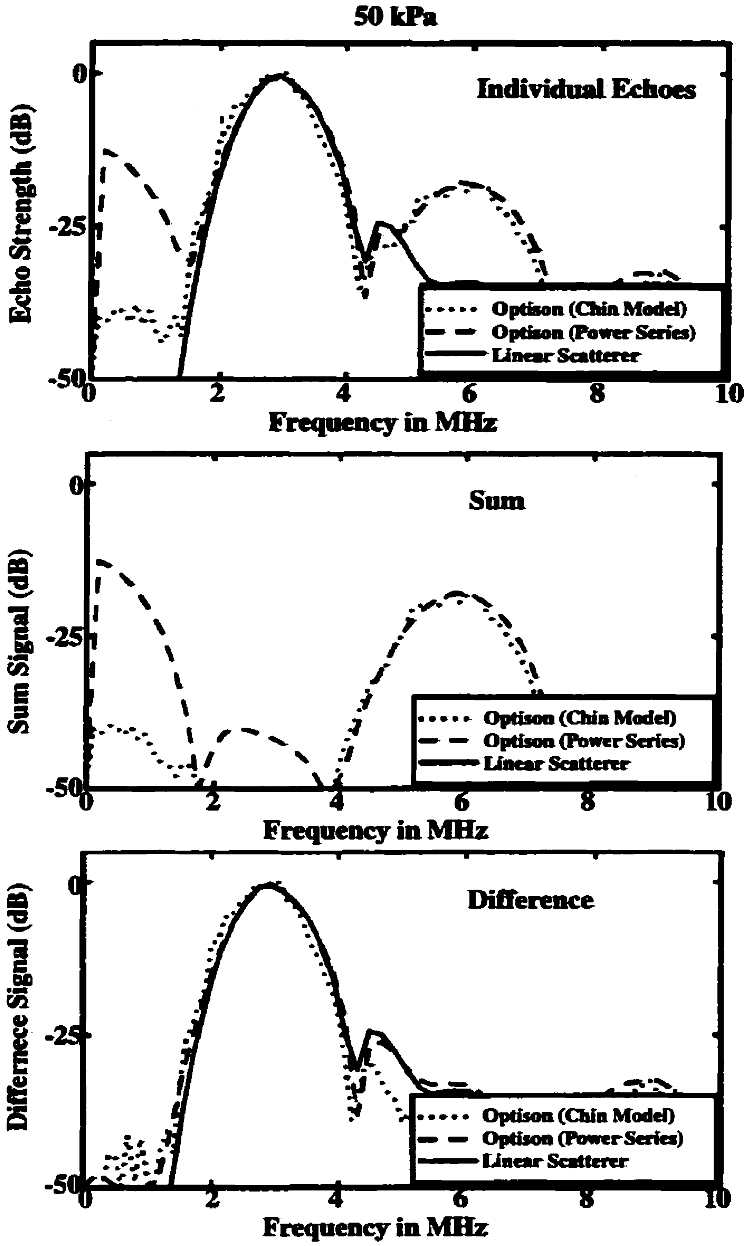

Figure 15: Simulated low power radio frequency (RF) echo spectra from Optison for a 4 cycle, 50 kPa tone burst at 2.9 MHz --- Top: spectra of individual echoes; Middle: spectra of $s(t)$*; Bottom: spectra of* $d(t)$*. Lines represent simulations using the scattering model of Chin et al. (Chin and Burns 1997)(dotted), and the best fit using Equation 34 (dashed). The solid line represents a linear scatterer (specular reflector -- note that the sum signal is zero for stationary linear scatterers). The models agree well at low transmit intensities.*

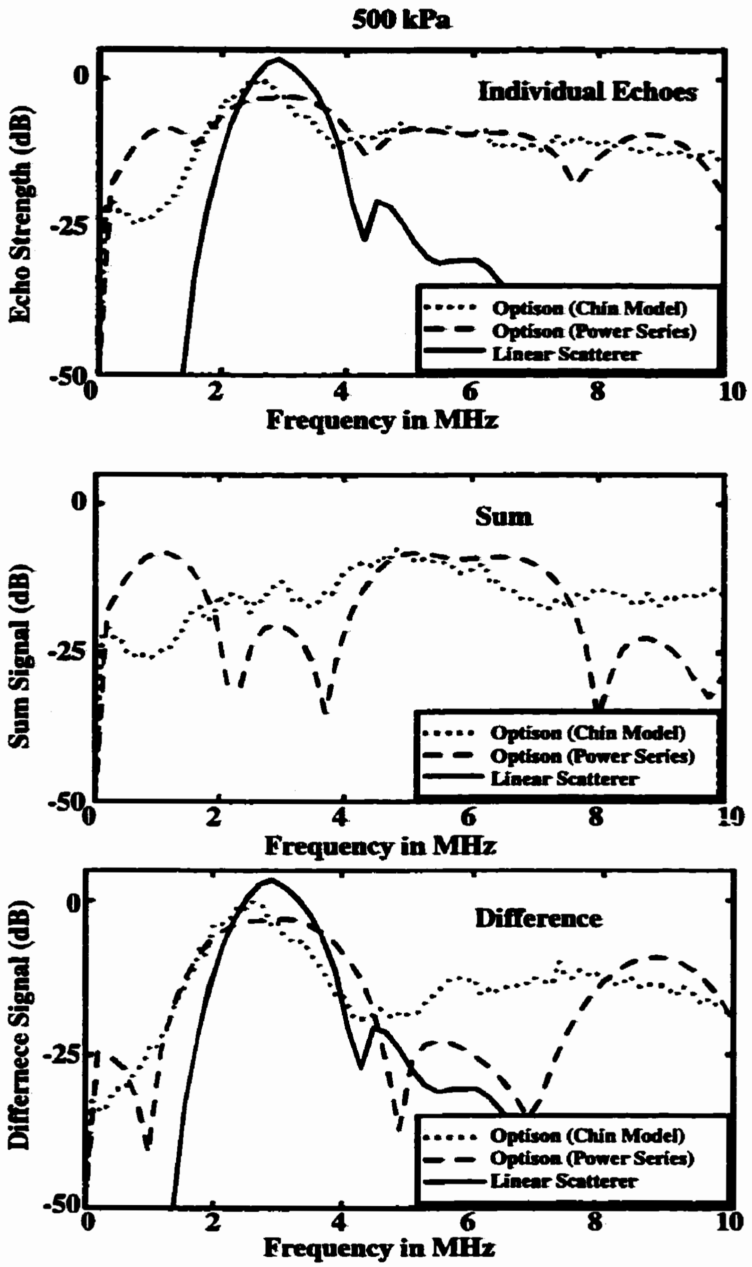

Figure 16: Simulated high power RF echo spectra from Optison for a 4 cycle, 500 kPa tone burst at 2.9 MHz --- Top: spectra of individual echoes; Middle: spectra of $s(t)$*; Bottom: spectra of* $d(t)$*. Lines represent simulations using the scattering model of Chin et al. (Chin and Burns 1997) (dotted), and the best fit using Equation 34 (dashed). The sold line represents a linear scatterer (specular reflector -- note that the sum signal is zero for stationary linear scatterers). The Chin bubble model predicts spectral broadening at high transmit intensities.*

Similar results predict that for broadband transmit pulsing, particularly at high transmit pressures, $s(t)$ will contain significant energy over a range of frequencies overlapping the transmit bandwidth. It should thus be possible to perform pulse inversion detection with broadband transmission and reception over the full bandwidth of the imaging transducer, producing significant contrast gains over conventional imaging without sacrificing resolution.

2.4.2 Experiment

2.4.2.1 Doppler Spectra

Figure 17 shows sample conventional Doppler spectra (top), and pulse inversion Doppler spectra (bottom) for both SHU 563A and cellulose for a single cycle transmit pulse. Both sets of spectra have been processed identically. In the conventional Doppler (Figure 17 top), the zero frequency clutter signal from the latex tube and the spread of Doppler shifts between $-f_{pr}/4$ and $-f_{pr}/4$ from the SHU 563A and cellulose are clearly visible. The SHU 563A and cellulose cannot be distinguished on the basis of signal strength or Doppler frequency.

In the pulse inversion Doppler spectra (Figure 17 bottom), the latex clutter signal appears at $f_{pr}/2$ as predicted by theory. A small nonlinear clutter signal from the latex is also visible at zero frequency and represents the effects of nonlinear propagation followed by linear scattering. Both SHU 563A and cellulose produce signals of comparable strength in the linear portion of the spectrum (between $-f_{pr}/2$ and $-f_{pr}/4$ and between $f_{pr}/4$ and $f_{pr}/2$). More significantly, the nonlinear portion of the SHU 563A spectrum contains clear Doppler shifts where none are present from the cellulose. Positive contrast can thus be achieved between linear and nonlinear scatterers where none existed before. This gain in contrast cannot be explained on the basis of differences between the filtered RF spectra from these two media (Figure 18). Note that the increased agent to tissue contrast in broadband PID is gained at the expense of reduced signal strength in the nonlinear portion of the spectrum.

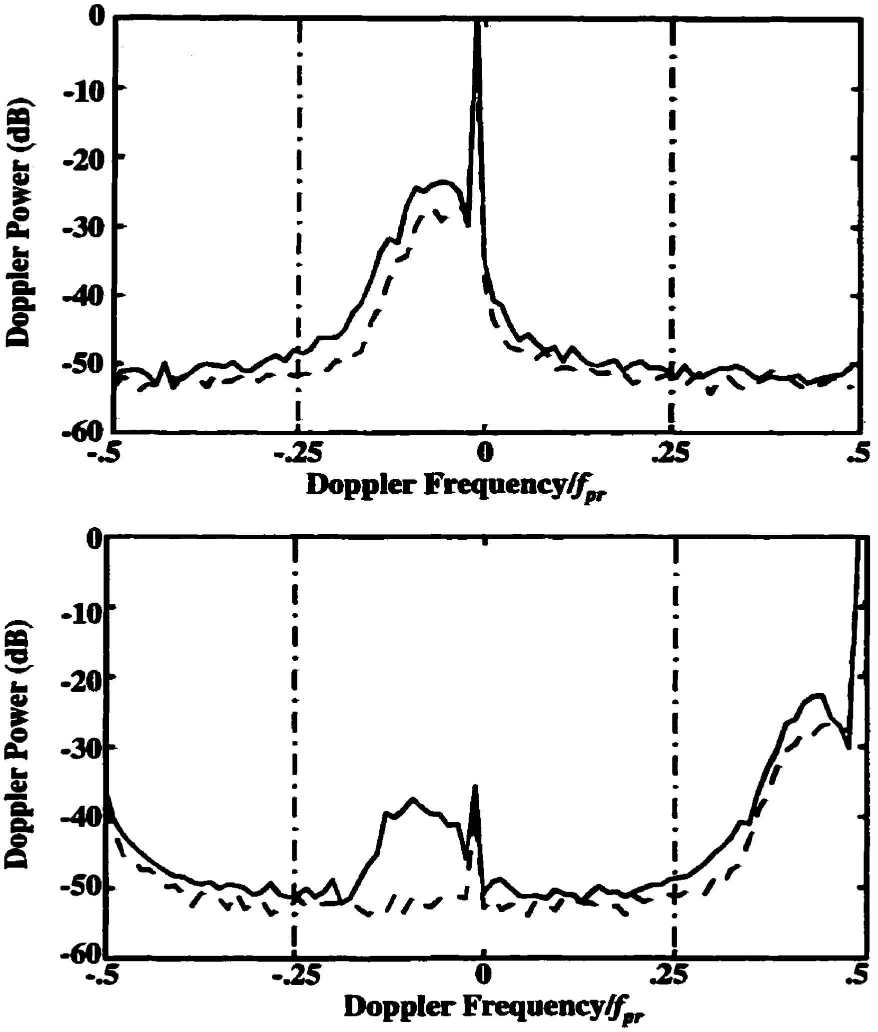

Figure 17: Broadband Doppler Spectra: Conventional Doppler (top) and pulse inversion Doppler spectra (bottom) from SHU 563A (solid lines) and cellulose (dashed lines) for 1 cycle transmit bursts (1.2 MPa peak to peak). In each graph, receiver gain is the same for both cellulose and SHU 563A. Doppler frequencies have been normalized to f_{pr}.

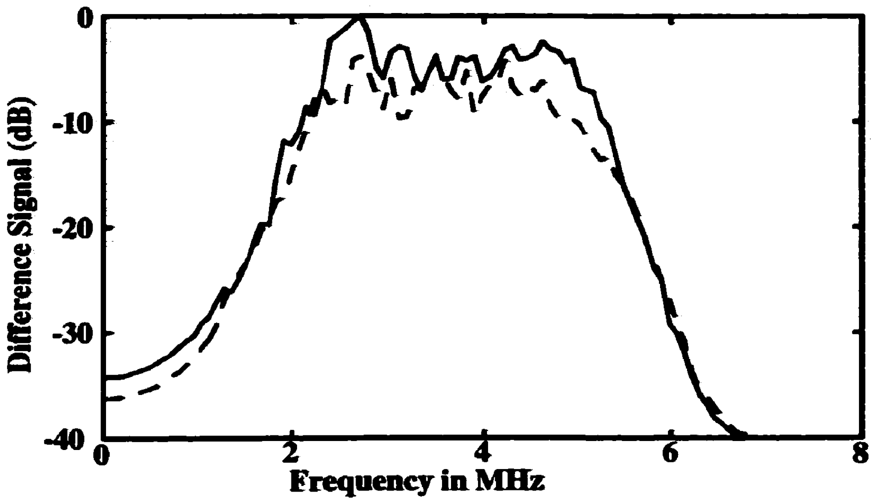

Figure 18: Radio frequency (RF) spectra of data from Figure 17. At 1.2 MPa p-p incident pressure, broadband echoes for SHU 563A (solid) and cellulose (dashed) cannot be separated on the basis of RF frequency content.

The relationship between echo power, Doppler frequency and RF frequency can been derived from a 2D FFT of the Doppler echoes (Wilson 1991). Figure 19 (top) shows conventional Doppler echo power as a function of echo (RF) frequency and Doppler frequency for SHU 563A and the cellulose control (stationary clutter has been suppressed by subtracting the DC and Nyquist frequency Doppler signals from the spectra). Note that in both cases, Doppler frequency increases proportionally with echo RF frequency as predicted by the Doppler equation. These data further demonstrate that broadband conventional Doppler cannot distinguish between linear and nonlinear scattering. Figure 19 (bottom) shows PID echo power as a function of echo (RF) frequency and Doppler frequency for SHU 563A and the cellulose control. Broadband pulse inversion Doppler produces signals in the nonlinear portion of the Doppler spectrum across the entire RF bandwidth of the received signals from the contrast agent, as predicted by the bubble model. No nonlinear echoes were detected from the cellulose control.

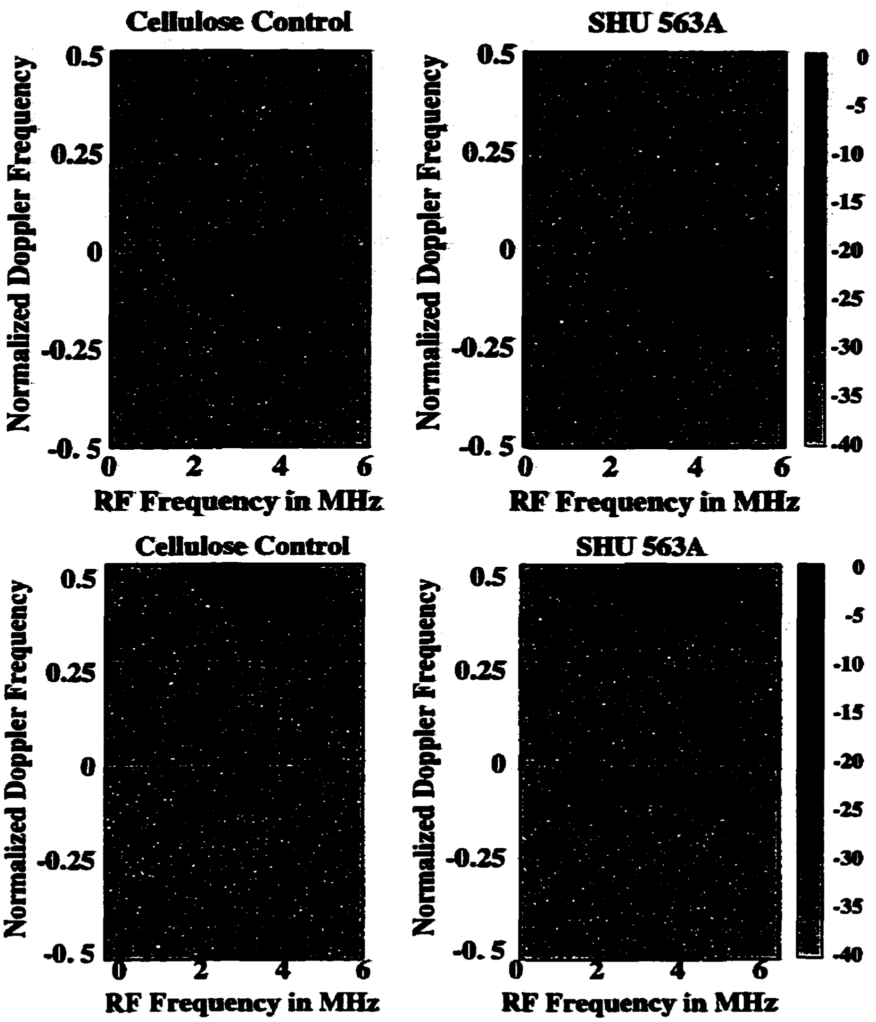

Figure 19: Echo power in dB as a function of Doppler and RF frequency for Broadband Pulses: 1 cycle, 2.9 MHz, 1.2 MPa transmit pulsing; TOP: conventional Doppler; BOTTOM: pulse inversion Doppler. The negative half of the RF spectrum in each case (not shown) was identical to the positive half, but with inverted Doppler shifts. Broadband pulse inversion Doppler can operate over the entire spectrum of the RF echoes.

Conventional and pulse inversion Doppler spectra from the narrowband experiments show features similar to the corresponding broadband spectra (Figure 20 and Figure 21) show sample results from 5 cycle transmit pulses). Narrowband pulse inversion Doppler exploits harmonic detection to increase the relative strength of the nonlinear signal and should therefore provide signal to noise and dynamic range improvements over broadband PID. Some nonlinear signal from the cellulose is now apparent in Figure 21 (bottom), and represents the effects of nonlinear propagation followed by linear scattering from the moving cellulose particles. While nonlinear scattering from stationary objects can be suppressed in PID by using conventional Doppler wall filters, nonlinear propagation echoes from moving tissue will limit the maximum contrast attainable with both PID and harmonic Doppler.

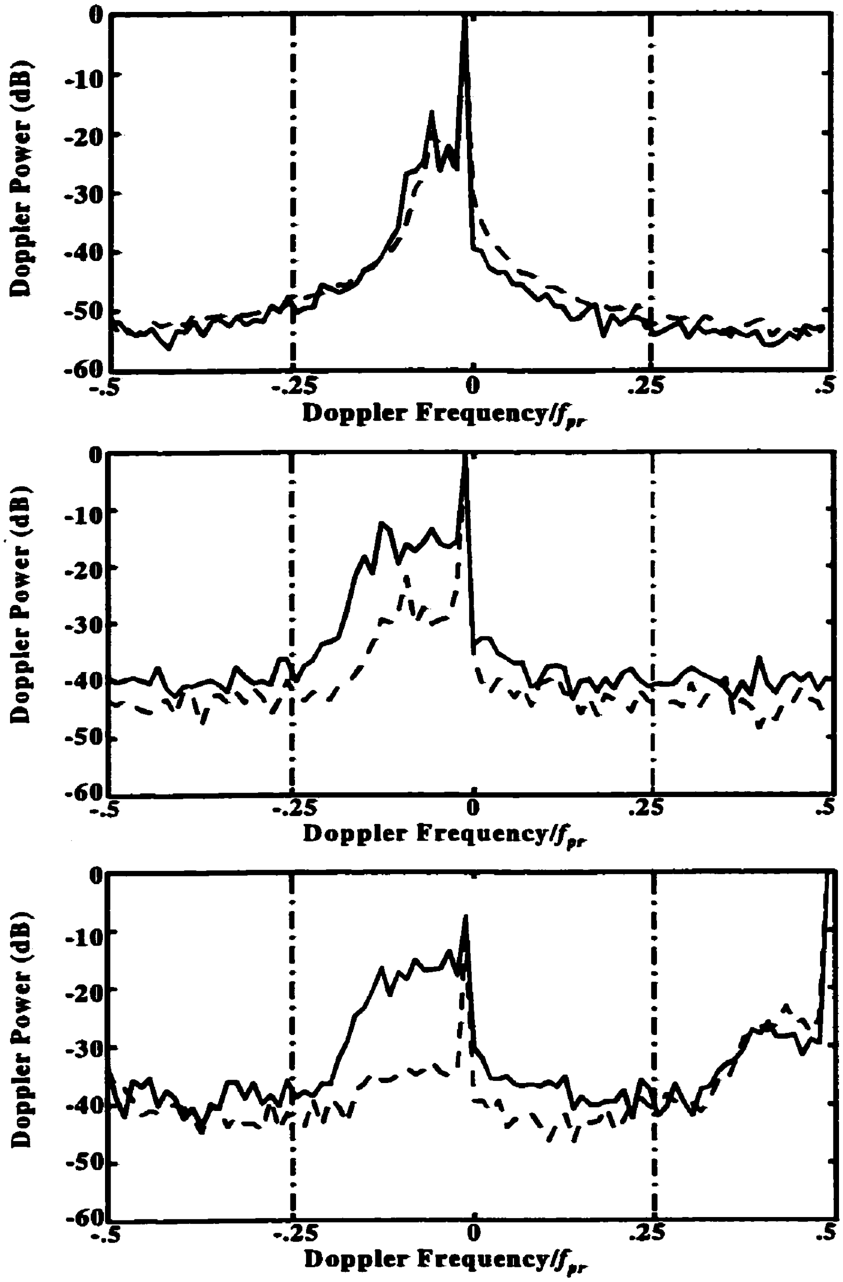

Figure 20: Narrowband Doppler Spectra: Conventional Doppler (top) harmonic Doppler (middle) and pulse inversion Doppler spectra (bottom) from SHU 563A (solid lines) and cellulose (dashed lines) for 5 cycle transmit bursts (500 kPa peak to peak). In each graph, receiver gain is the same for both cellulose and SHU 563A. Doppler frequencies have been normalized to f_{pr}. Apparent nonlinear scattering from cellulose is visible in the PID spectrum (bottom).

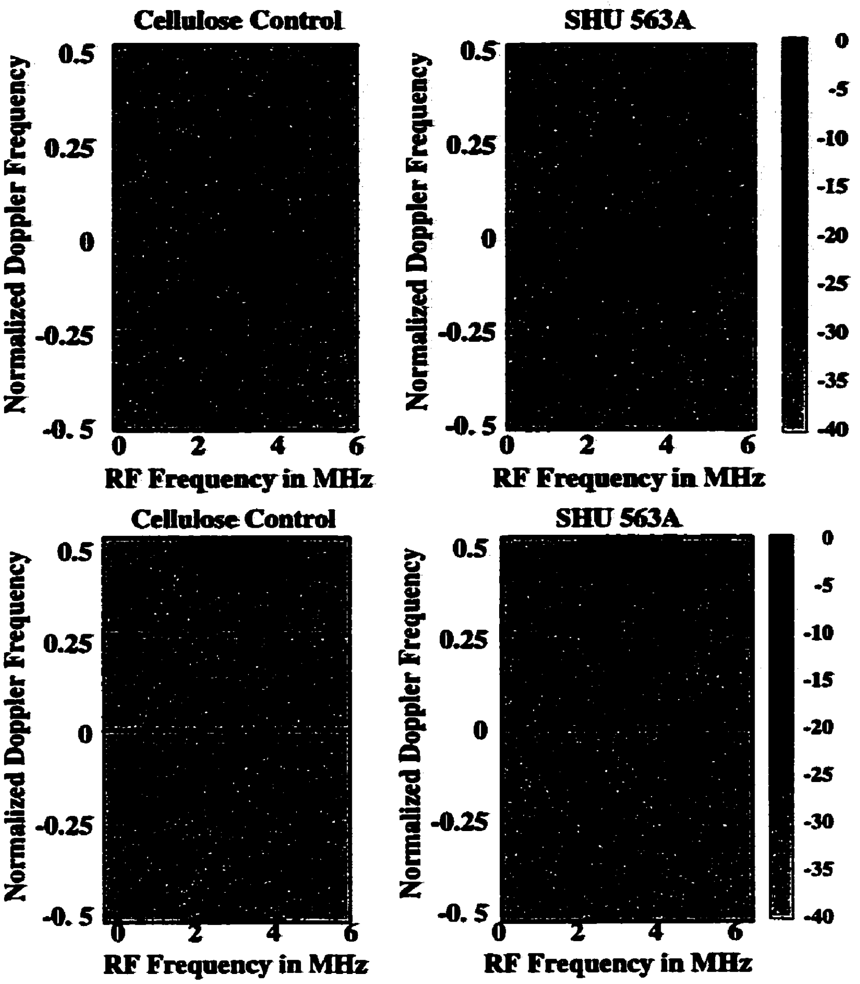

Figure 21: Echo power in dB as a function of Doppler and RF frequency for Narrowband Pulses: 5 cycle, 2.2 MHz, 500 kPa transmit pulsing; TOP: conventional Doppler; BOTTOM: pulse inversion Doppler. The negative half of the RF spectrum in each case (not shown) was identical to the positive half, but with inverted Doppler shifts. The beat patterns in RF frequency in the linear echo components are sidelobes due to windowing of the transmit pulses. The nonlinear signal is concentrated at the second harmonic of the transmit frequency.

2.4.2.2 Power Dependence of Detected Contrast

Pulse inversion Doppler using broadband pulsing increased agent to cellulose contrast by up to 16 dB over conventional Doppler (Figure 22 top). This contrast increase was greatest at high incident pressures (above 1 MPa). For narrowband pulses, pulse inversion Doppler increased agent to cellulose contrast by 5 to 16 dB over conventional Doppler and by up to 10dB over harmonic Doppler (Figure 22 middle, bottom). Like harmonic Doppler, contrast gains over conventional Doppler were largest at high incident pressures. Contrast gains over harmonic Doppler were greatest at incident pressures between 100 and 500 kPa, where overlap between the transmit and receive passbands masks the nonlinear signal in harmonic Doppler. At low transmit intensities, the nonlinear pulse inversion Doppler signals from cellulose were dominated by system noise, resulting in an overestimation of signal power. The data shown in Figure 22 thus represent conservative estimates of agent to cellulose contrast for pulse inversion Doppler. Results from Optison were similar to those from SHU 563A, with increased nonlinear scattering at low transmit intensities.

According to theory, the ratio, ρ, of the total Doppler power in the nonlinear portion of the spectrum to total power in the linear portion of the spectrum will be a measure of the relative amount of nonlinear scattering detected. This ratio was measured experimentally to be 20 dB higher for SHU 563A than for cellulose and 27 dB higher for Optison than for cellulose (Figure 23).

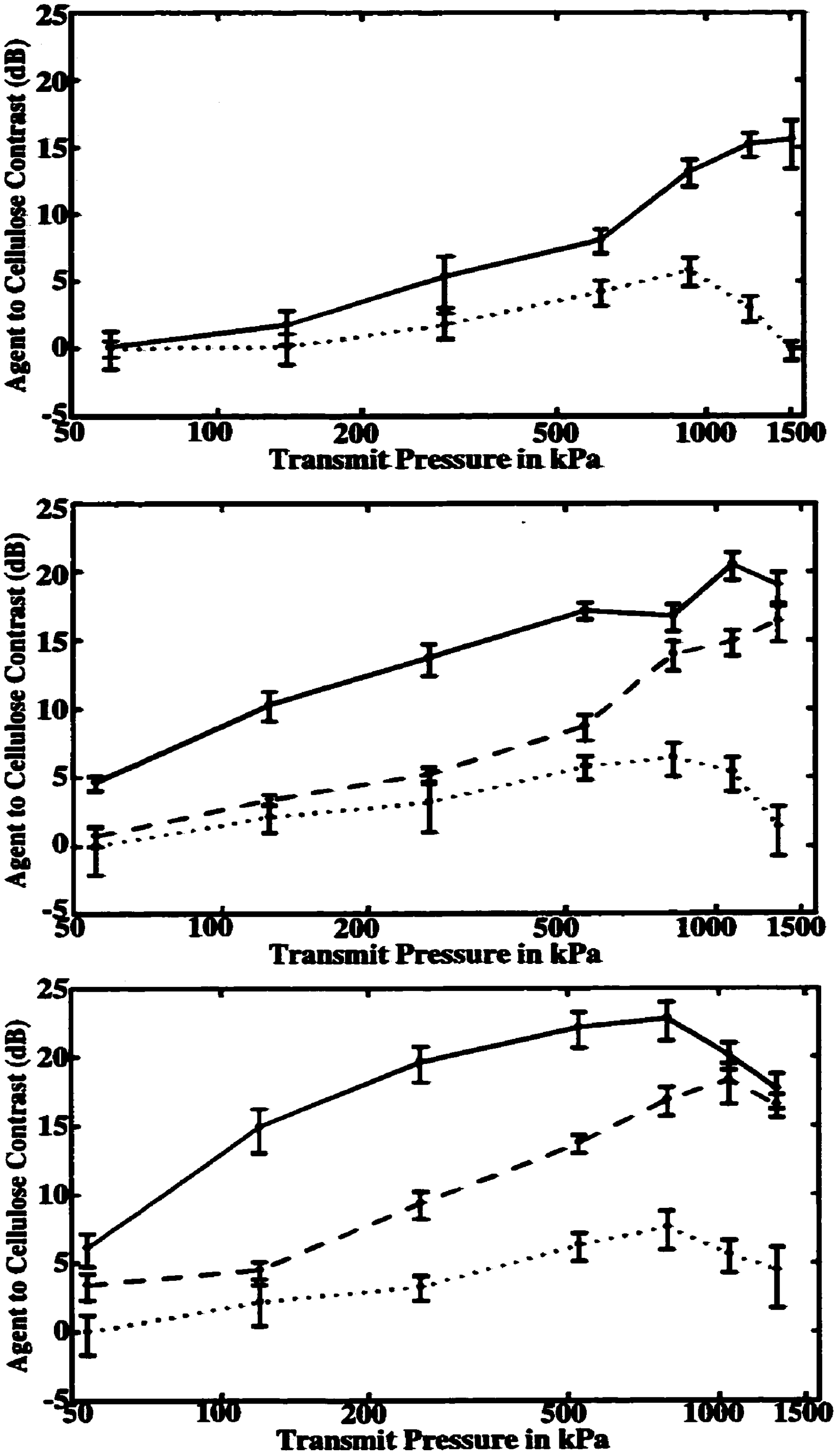

Figure 22: SHU 563A to cellulose contrast vs transmit pressure for 1 cycle (top), 2 cycle (middle) and 5 cycle (bottom) transmit bursts. Lines represent conventional (dotted), harmonic (dashed) and pulse inversion Doppler (solid).

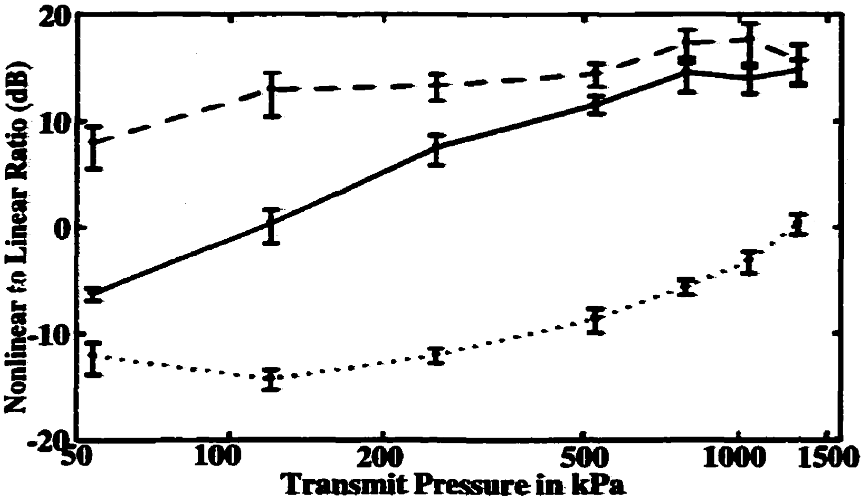

Figure 23: Nonlinear to linear ratio ρ vs transmit pressure for 5 cycle transmit bursts. Lines are for Optison (dashed), SHU 563A (solid) and cellulose (dotted).

2.5 Discussion and Conclusions

Pulse inversion Doppler is proposed as a method to overcome some of the limitations of harmonic detection. The performance of harmonic detection is compromised by an overlap in RF spectra between the second harmonic echoes (centred at $2f_0$) produced by nonlinear scattering and the fundamental echoes (centred at f_0) produced by both linear and nonlinear scattering. This overlap increases with the bandwidth of the transmitted pulses and is particularly detrimental when the nonlinear echoes are weak in comparison with the linear echoes, such as at low transmit amplitudes or low microbubble concentrations. Whereas harmonic detection operates in the radio frequency domain to distinguish between linear and nonlinear scattering, pulse inversion Doppler separates linear and nonlinear scattering in the Doppler frequency domain. It effectively eliminates the problem of spectral overlap and can therefore enhance the detection of nonlinear echoes in the situations mentioned above. In particular, this technique can be applied to broadband transmit pulsing, although some signal strength and dynamic range must be exchanged for contrast.

Since pulse inversion Doppler is a sensitive technique for separating linear and nonlinear scattering, it would seem ideally suited to the detection of microbubble contrast agents in linear tissue. It provides motion discrimination capabilities similar to conventional Doppler techniques and has a maximum detectable Doppler shift which is half that of conventional Doppler. Although further testing is required, results from *in vitro* experiments show that it can offer significant benefits over harmonic Doppler, the most sensitive technique currently available. These benefits include increased resolution, higher contrast, and improved performance at low transmit levels.

There are a number of implications for new contrast ultrasound imaging strategies based upon this technique. Due to its increased resolution, the detection and delineation of small vessels (such as coronary arteries) should be enhanced. Due to its improved sensitivity, smaller quantities of agent should be detectable: a lower dose of agent could be used for a specified task, and a given dose of agent could provide more contrast and a longer effective imaging time. Due to its improved performance at low power levels, it should provide more robust contrast throughout the image field of view. Pulse inversion Doppler imaging can also be performed at lower transmit intensities, prolonging microbubble lifetimes and perhaps obviating the need for intermittent imaging to show myocardial perfusion. Together, these factors should enhance the capabilities of contrast ultrasound imaging in applications ranging from perfusion stress echo measurement to tumour detection and identification.

One other potential application of pulse inversion Doppler is of interest. Harmonic greyscale imaging is now being used to image "tissue harmonic" echoes in the absence of contrast media (Averkiou et al. 1997; Christopher 1997). These echoes are generated by nonlinear propagation of the transmitted pulse followed by linear scattering from tissue and appear to improve image quality in some patients. Pulse inversion Doppler can be operated in a high frame rate power imaging mode in which as few as two pulses of sound are transmitted down each line of sight. This could offer a tissue harmonic imaging technique operating at half the frame rate of harmonic greyscale imaging but with higher resolution and contrast. A related technique has also been described for imaging nonlinear scattering from tissue which uses two pulses of different amplitudes to achieve cancellation of the fundamental signal (Christopher 1997). While contrast with the two-pulse imaging technique will be degraded by tissue motion, a four to eight pulse version should allow the use of more efficient clutter rejection filters and could be used (at a reduced frame rate) in applications such as echocardiography where motion is an issue. To image contrast agents in moving blood with pulse inversion Doppler, the nonlinear clutter from tissue harmonics can be removed using suitable wall filters. Even in the absence of motion, large transient Doppler shifts generated from disrupting microbubbles can be used to distinguish microbubble echoes from the nonlinear tissue clutter (Uhlendorf and Hoffman 1994). The presence of tissue harmonics nonetheless affects the performance of both pulse inversion Doppler and harmonic Doppler (the increase with pressure of the nonlinear to linear ratio for cellulose in Figure 23 is likely due to nonlinear propagation effects).

Experimental results presented in this work are for Doppler detection down a single line of sight. Further experiments with a real time, colour/power Doppler imaging system on an *in vivo* model are required to confirm some predictions and assess the clinical potential of this technique.

3 An Analysis of Techniques for Perfusion Imaging with Microbubble Contrast Agents

This Chapter has been submitted for publication as: Hope Simpson, D., Burns, P.N. An Analysis of Techniques for Perfusion Imaging with Microbubble Contrast Agents. IEEE Transactions on Ultrasonics, Ferroelectrics and Frequency Control (manuscript KF 1702). It has been edited for clarity and is reprinted with permission.

3.1 Introduction

Microbubble contrast agents for diagnostic ultrasound are now available clinically in many countries. These agents, together with newly developed agent-specific imaging techniques, have made it possible to detect and image blood flowing in small blood vessels using diagnostic ultrasound systems. Efforts are underway to develop clinical techniques using ultrasound contrast agents to assess regional microvascular perfusion in tissues such as the myocardium and liver (Blomley et al. 1999a; Cosgrove 1996; Kaul et al. 1997; Porter et al. 1995; Porter et al. 1996). While all of these applications involve contrast imaging, the acoustic conditions (scanning depth, tissue motion, optimal transmit frequency, transmit intensity) vary significantly from application to application and even with depth for a single application. This, combined with the range of acoustic properties of the different contrast agents now available, provides significant challenges for the design and use of contrast imaging instruments. In particular, the selection of imaging techniques and parameters should be optimized carefully for each combination of agent and application.

Current techniques for contrast imaging may be grouped into three classes. Harmonic imaging uses radio frequency filtering on a single echo to separate nonlinear microbubble echoes from the linear echoes from tissue (Burns et al. 1996; Powers et al. 1997; Uhlendorf and

Hoffman 1994). Power Doppler imaging uses pulse-to-pulse decorrelation in agent echoes caused by microbubble disruption to distinguish between agent and tissue using Doppler frequency processing (Powers et al. 1997; Uhlendorf and Hoffman 1994). In the previous Chapter, we described a third class of techniques that we call Pulse Inversion Doppler (PID), which detects both nonlinear scattering and agent decorrelation using Doppler frequency processing (Hope Simpson and Burns 1997; Hope Simpson et al. 1999). Two-pulse variants of this technique have also been developed and marketed by instrument manufacturers ("Pulse Inversion Harmonic Imaging" (ATL ultrasound Inc., Bothell, WA) and "Wideband" or "Ensemble Contrast Harmonic Imaging" (Siemens, Issiquah, WA)).

This Chapter introduces a common methodology, based directly upon the measured or modeled properties of agent and tissue, whereby Doppler and radio frequency filters for perfusion imaging with each of these techniques can be optimized. Data from contrast perfusion measurements *in vivo* are used to illustrate the application of these techniques. This work fills several needs. In addition to providing the first mathematical analysis of Doppler filters for contrast imaging, it examines the connections between radio frequency and Doppler frequency properties of microbubble echoes and the implications for filter development. The algorithms for filter design described here require no *a priori* knowledge of transmit pulse sequences. They are thus equally applicable to PID and conventional Doppler pulsing, and should also be capable of handling other novel pulsing sequences as they are developed. Most importantly, because these algorithms require minimal operator intervention, they will enable objective comparisons of the various contrast imaging techniques to be made under different operating conditions.

3.2 Theory:

In a generalized Doppler imaging system, two or more ultrasound pulses are transmitted down each line of sight in the scan plane and the echoes are accumulated in digital memory and processed to form an image. The basic steps of ultrasound transmission, reception and processing are illustrated in Figure 24. For contrast imaging, transmit pulsing parameters can be adjusted to maximize the differences between the echoes from microbubbles and those from tissue. Doppler and RF filtering can then be developed to exploit these differences and maximize the detected signal from agent, while minimizing the detected signal from tissue.

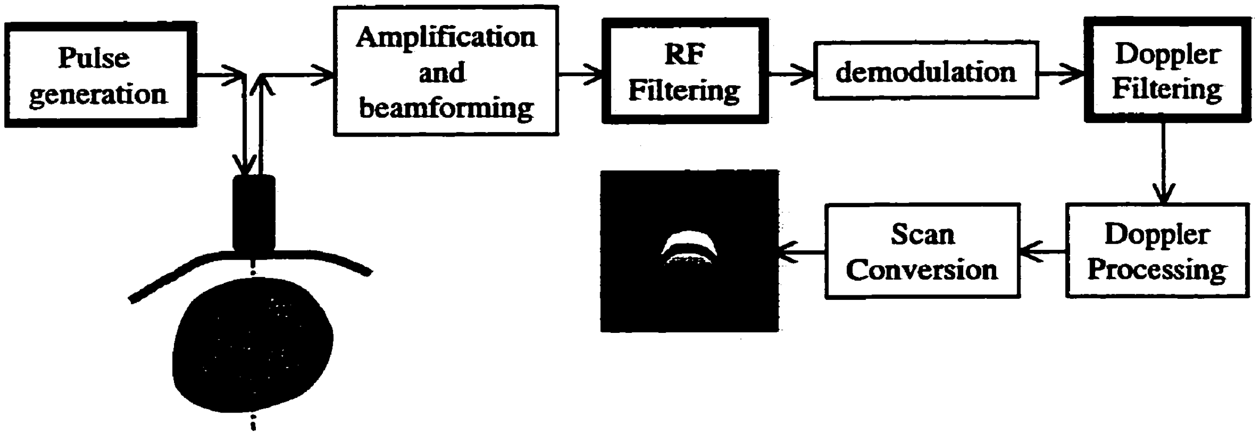

Figure 24: The basic steps of Doppler ultrasound transmission, reception and image formation are shown. The steps in bold are discussed in the present Chapter.

3.2.1 Doppler Versus Pulse Inversion Doppler Transmission

A mathematical treatment of Doppler and pulse inversion Doppler pulsing is provided in Chapter 2. These techniques are illustrated graphically in Figure 25. In conventional Doppler pulsing, a sequence of two or more identical pulses is transmitted down each line of sight in the scan plane at a fixed pulse repetition frequency (PRF), f_{pr}. By using the temporal changes in echo amplitude from a given depth to estimate a Doppler shift frequency (Figure 25a, b, c), echoes from moving blood and moving or disrupting microbubbles, can be distinguished from echoes from slow moving tissue. Doppler clutter filters are then used to remove the tissue echoes. For perfusion imaging, however, blood and tissue have similar velocities. Hence, differences between the Doppler spectra of agent and tissue are due solely to microbubble disruption.

In Pulse Inversion Doppler (PID), the modulation of the transmitted pulse sequence at half the Doppler PRF causes a corresponding pulse-to-pulse modulation of the linear echoes from tissue (Figure 25d), so that Doppler frequencies from tissue are shifted by the $f_{pr}/2$ (the Nyquist frequency) in the Doppler spectrum (Figure 24f). Doppler shifts from linear targets thus almost inevitably produce aliasing in PID, and appear at both the highest ($f_{pr}/2$) and lowest (- $f_{pr}/2$) frequencies in the Doppler spectrum. Unlike tissue, gas bubbles respond differently to rarefaction (negative acoustic pressure), than to compression (positive acoustic pressure). Such nonlinear behaviour produces PID echoes that can be separated into two components: one component that is modulated at half the Doppler PRF, and a second component that remains unmodulated (Figure 25e,f). This second component also gives rise to the second harmonic signals in harmonic imaging. Provided that all Doppler shifts are less than $f_{pr}/4$, stationary and moving linear echoes and stationary and moving nonlinear echoes all will appear at different locations in the Doppler spectrum. Modified Doppler filters can then be used to isolate any combination of these components.

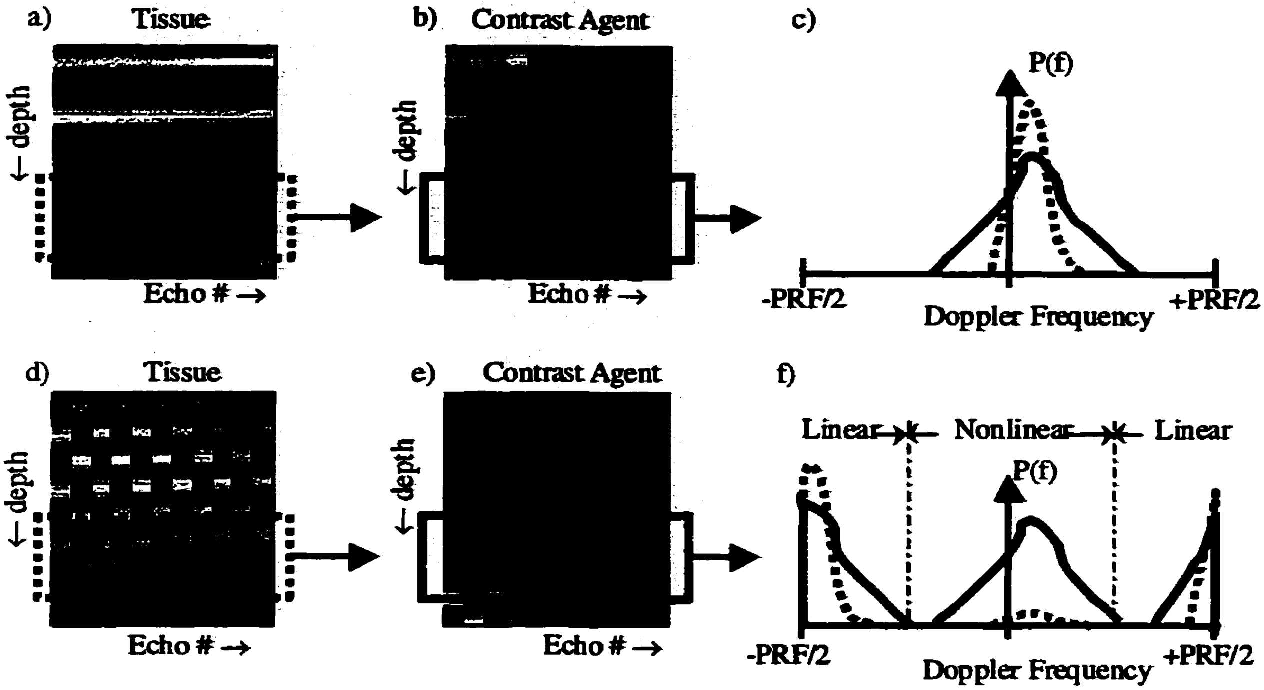

Figure 25: Principles of Contrast Doppler and PID: a) conventional Doppler RF echoes from tissue for a single line of sight - echo amplitude (greyscale) is displayed as a function of depth (y-axis) for successive echoes (x-axis); b) echoes from contrast agent; c) sketch of Doppler spectra from agent (solid lines) and tissue (dotted lines). In conventional Doppler, perfusing agent and tissue have similar Doppler frequencies. Disruption-induced spectral broadening allows the agent to be detected in tissue. d) – f) same as a) – c) but for PID. In PID, successive tissue echoes are inverted, modulating the Doppler shifts by PRF/2. A component of the nonlinear microbubble echoes is not inverted, producing Doppler shifts similar to conventional Doppler.

3.2.2 Echo Processing for Microbubble Detection

In a typical ultrasound system, all of the echoes from each line of sight are collected together for processing. RF filtering is first applied to each individual echo to isolate the frequencies of interest, and remove electronic noise. The echoes are then demodulated in quadrature at the RF filter centre frequency and resampled at a lower sampling rate. The complex Doppler signal is formed by collecting one sample from each demodulated echo at a delay corresponding to the depth of interest. For colour and Power Doppler imaging, this process is repeated at all depths of interest. Doppler wall filters are applied to each of these signals to remove clutter, and algorithms are then used to estimate the Doppler power or mean Doppler frequency in each sample volume.

The following analysis will first consider the optimization of RF filtering and Doppler filtering as separate topics, and will then discuss the simultaneous optimization of these filters. Agent to tissue contrast, defined as the ratio of the power of the signal detected from contrast agent to the power of the signal detected from tissue, will be used to evaluate different detection strategies.

3.2.2.1 Radio Frequency Filtering

Radio frequency filtering for contrast agent detection should take into account the properties of agent, tissue clutter and electronic noise. Signal processing theory shows that the agent to tissue contrast at the RF filter output will be maximized when

$$H(f) = k\frac{A^*(f)}{N(f)}, \qquad 49$$

where *H(f)* represents the frequency response of the filter, $A^*(f)$ represents the complex conjugate of the amplitude spectrum of the agent echoes and *N(f)* represents the combined power spectrum of clutter and electronic noise (Papoulis 1984).

This relationship essentially describes a modified matched filter. It implies that the RF filtering should be designed to have a high gain at frequencies for which the agent signal is strong and the clutter signal is weak, and a low gain when the situation is reversed. It also provides a direct link between the measured and/or modeled properties of agent and tissue and the optimal filter properties. Equation 49 requires knowledge of both the magnitude and phase characteristics of agent and tissue echo spectra. In practice, the magnitudes can be obtained from direct *in vivo* or *in vitro* measurements of echoes from agent and tissue. The phase of such measurements, however, is related to the spatial distribution of scatterers rather than to the true phase response of single scatterers. While modeling or in vitro experiments on individual microbubbles one day may yield phase measurements suitable for filter design (Chin and Burns 1997; Dayton et al. 1999b), such comprehensive measurements do not exist at present. For the present work, finite impulse response (FIR) digital filters were designed to match the magnitude response of Equation 49 near the maximum of *H(f)* (over the –20 dB bandwidth). Criteria unrelated to agent to tissue contrast, such as resolution and image quality will likely play a role in the final choice of RF filters on clinical systems.

When only a single pulse is transmitted down each line of sight (as in the case of harmonic imaging), the filtering for contrast imaging is complete here. When multiple pulses are transmitted, appropriate Doppler filtering may be used to increase agent to tissue contrast.

3.2.2.2 Conventional Clutter Filters for Doppler Imaging:

In conventional Doppler imaging, no knowledge of blood velocity is assumed. Consequently, conventional Doppler filters ('wall' or 'clutter' filters) are based upon to the properties of tissue alone. They are designed to remove any echoes whose Doppler characteristics resemble those of tissue. Remaining signals are then interpreted as blood.

If N pulses are transmitted per line of sight, then the Doppler signal at each depth will also contain N samples (N is commonly referred to as the packet length). For typical packet lengths of 4 to 16 pulses, infinite impulse response digital filtering techniques require careful initialization to be effective (Kadi and Loupas 1995). A more general approach to filter design, suggested by Torp and outlined below, considers the Doppler signal as an N-dimensional complex vector, $\vec{v}$ (Torp 1997). All possible linear filter operations can then be expressed in the form:

$$\vec{v}' = A\vec{v}\,, \qquad 50$$

where $\vec{v}'$ is the filtered Doppler signal, and A is a complex $N \times N$ filter matrix.

The frequency response for a matrix filter can be estimated by calculating the magnitude of the filter output in response to short segments of complex sinusoids at different frequencies (Torp 1997).

If we now assume that the clutter signals form an *M*-dimensional subspace of all possible *N*-dimensional signals, we can choose

$$A = I - PP', \qquad 51$$

so that

$$\vec{v}' = \vec{v} - PP'\vec{v}, \qquad 52$$

where *I* is the identity matrix and *P* is a matrix whose columns are the basis vectors of the clutter space.

These filters subtract from the Doppler signal, the portion that resembles the clutter. Bjaerum and Torp have shown that, for optimal rejection of tissue, the columns of *P* should be the eigenvectors of the clutter autocorrelation matrix corresponding to its *M* largest eigenvalues. Furthermore, the clutter autocorrelation matrix, R_{tt}, may be estimated directly from the measured tissue echoes (Bjaerum and Torp 1997), as

$$R_{tt} = \frac{1}{K}\sum_{i=1}^{K} \vec{v}_i \vec{v}_i^{*T}, \qquad 53$$

where $\vec{v}_i$ are measured Doppler signals from tissue and $\vec{v}_i^{*T}$ denotes the complex conjugate transpose of $\vec{v}_i$.

3.2.2.3 Filters for Microbubble Perfusion Imaging

In contrast perfusion imaging, unlike conventional Doppler imaging, the Doppler spectra of microbubbles are predictable to some degree. When blood and microbubbles are moving slowly, their Doppler spectra will be dominated by microbubble disruption, and their PID spectra will be dominated by a combination of disruption and nonlinear scattering. Both disruption and nonlinear scattering are determined by the physical properties of microbubbles and acoustic conditions rather than physiological properties such as blood velocity. Hence, it should be possible to measure Doppler waveforms *in vivo* from a limited number of patients and then use these experimental data to develop Doppler filters, tuned to each combination of agent, tissue and acoustic environment, which can be used in a large number of patients. To distinguish these filters from those described above, they will be referred to as agent detection filters rather than clutter filters.

To design agent detection filters for contrast perfusion imaging, the autocorrelation matrices for agent and tissue, R_{tt} and R_{aa}, must be determined first from measured or simulated Doppler signals. Agent to tissue contrast can then be maximized by projecting the Doppler signals onto the principle eigenvector, $\vec{e}_1$, of the matrix (Schleher 1991)

$$Q = R_{tt}^{-1} R_{aa} \qquad 54$$

so that

$$A = \vec{e}_1 \vec{e}_1' \qquad 55$$

or, equivalently,

$$A = \vec{e}_1' \qquad 56$$

The latter form turns the filtering process into a simple weighted sum of the elements of the sampled Doppler signal. Since the output of such a filter has only one degree of freedom, it cannot be used for velocity estimation, but only for Doppler power estimation. Fortunately, Doppler power is directly proportional to the concentration of agent in the Doppler sample volume (Frush et al. 1995; Schwarz et al. 1993), and is thus the most relevant parameter for perfusion imaging. A simple interpretation of the filters described above is that $\vec{e}_1$ represents a prototype echo that looks most like agent echoes and least like tissue echoes (in a least-squares sense). The filtering process retains only the component of each echo that resembles $\vec{e}_1$. Bjaerum and Torp (Bjaerum and Torp 1997) have suggested a form of filter that uses all of the eigenvectors of Q, weighted according to their corresponding eigenvalues.

All of these matrix filters use the complex Doppler signals as input and will thus be complex-valued themselves. This property allows the design of filters with asymmetric frequency responses (i.e. positive and negative Doppler frequencies may be filtered differently). While asymmetric filters can provide added flexibility in some situations, it is often desirable to constrain filters to have symmetric frequency responses so that they are non-directional and hence more universally applicable (Doppler spectra from disrupting microbubbles are also expected to be symmetric in the absence of significant motion). By treating the real and imaginary components of the Doppler signals as independent samples of real processes, it is possible to constrain R_{aa}, R_{tt}, $\bar{e}_1$ and A to be real-valued, ensuring a symmetric frequency response for the resulting filters and simplifying their implementation.

3.3 Experimental Methods

To assess the techniques described above, RF data were acquired from experiments conducted *in vivo* on two mongrel dogs (weighing approximately 22 kg and 24 kg respectively). The handling and treatment of the dogs followed guidelines of the Canadian Council on Animal Care and the Animals for Research Act. Each dog was premedicated with an intramuscular injection of acepromazine (0.5 ml/kg) and atropine (0.05 mg/kg). Anaesthesia was induced with inhaled Halothane (5%) and oxygen via a facemask. The dog was then intubated and maintained on inhalation halothane (0.8% to 1.5%) with oxygen.

Bolus injections of the contrast agent Optison™ (Mallinckrodt Medical, Inc., St. Louis) were administered via a 3-way stopcock attached to an 18 gauge angiocatheter in the left cephalic vein. A clinical ultrasound system (HDI-5000, ATL, Bothell WA) running prototype software and modified to allow acquisition of RF data was used for all imaging. A P3-2 phased array scanhead was clamped in place using a mechanical arm to record a right parasternal short axis view of the heart. Radio frequency data to form colour frames of the heart (intermittent imaging at 1 frame/3 heartbeats, 12 pulses per line, 1.5 MHz transmit frequency, 6 kHz PRF) were acquired before and after each injection using either conventional Doppler or pulse inversion Doppler transmission. The mechanical index (MI) was varied from 0.1 to 1.2.

Doppler dosimetry was used to monitor all injection. A 5 MHz pulsed wave Doppler probe was clamped in place over the left femoral artery using a mechanical arm and connected to a custom-modified Interspec XL Doppler system. The quadrature output components of the demodulated Doppler signal were recorded using a high-fidelity DAT recorder (Panasonic SV-3700), and were also fed to a Macintosh computer running custom software which calculated the pulse-averaged Doppler power and displayed this in real time. The Doppler power versus time data were recorded digitally for later analysis.

3.4 Results

All data analysis and image formation was performed offline using custom analysis software written in MATLAB™(The Mathworks Inc., Natick, MA).

Figure 26 shows reconstructed right parasternal short axis views of the heart before and after a 0.3 ml bolus injection of Optison. From such views, it was possible to identify echoes from myocardium, myocardium perfused with agent, and agent (regions 1,2 and 3 respectively). These echoes were used to optimize filters, and to measure agent to tissue contrast (power in region 3/power in region 1) and myocardial enhancement (power in region 2/power in region 1).

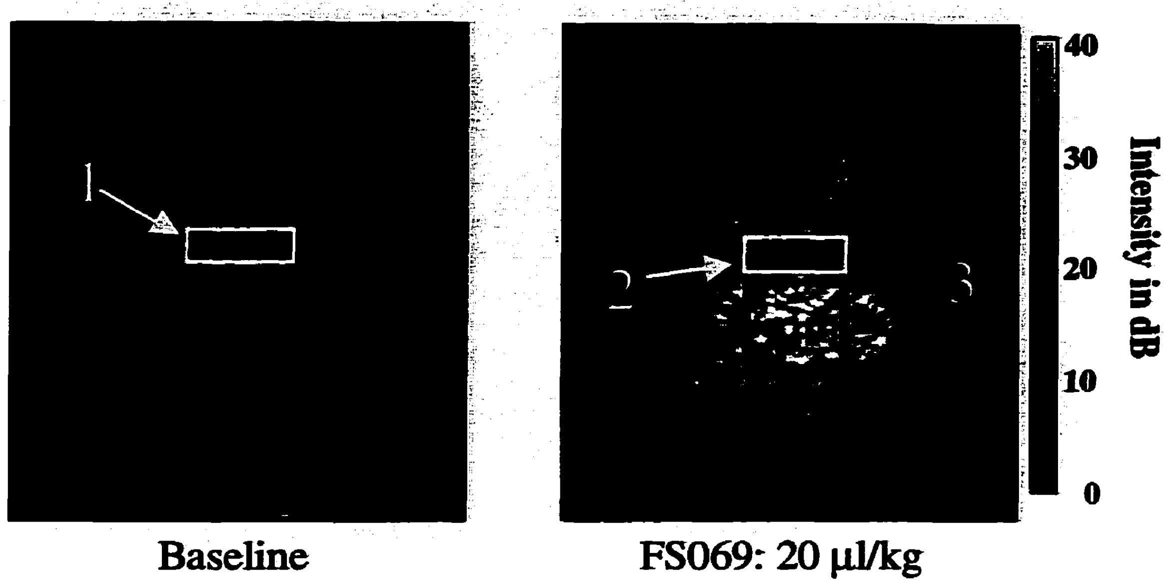

Figure 26: Reconstructed right parasternal short axis views of the heart before and after a 0.3 ml bolus injection of Optison (maximum depth: 11.7cm). From such images, echoes from tissue alone (1), perfused tissue (2), and agent alone (3) may be isolated for analysis.

3.4.1 Filtering for Agent Detection

For each injection, 61 point finite impulse response RF filters were designed with magnitude responses similar to Equation 49 over the –20 dB bandwidth of *H(f)*, using the agent echoes from the left ventricle after injection (region 3) to model agent, and the echoes from the myocardium before injection (region 1) to model tissue. These filters were applied to all of the echoes from the pre and post injection frames, and the data were then demodulated in quadrature at the filter centre frequency, band limited to 2 MHz using an 8th order Chebyshev type I filter, then resampled at 5 MHz. Following demodulation, the first echo from each line of was discarded (to reduce potential Doppler artifacts from multi-path echoes), and the remaining 11 echoes were available for Doppler processing. By using a subset of the available echoes, it was also possible to develop Doppler filters for packets of fewer than 11 pulses per line of sight.

Doppler filters were designed according to both Equations 51 and 56. Echoes from the myocardium after injection (region 2 in Figure 26) were used to model agent and echoes from the myocardium before injection (region 1) were used to model tissue. The post-injection myocardium echoes were used to model perfusing agent in preference to the ventricular echoes, since agent motion in the ventricles may have affected the corresponding Doppler spectra.

For high MI imaging, where even the Doppler spectra from the ventricles were dominated by microbubble disruption, filters were designed by using the data from the entire post-injection frame to model agent and the entire pre-injection frame to model tissue.

3.4.2 RF filtering

Sample RF spectra of echoes from tissue and Optison are shown Figure 27a. These echoes were acquired with conventional transmit pulsing at a mechanical index (MI) of 0.3. Figure 27b shows the frequency response given by Equation 49, together with the frequency response of a 61 point FIR filter suitable for imaging. Dashed lines in each figure show the locations of the centre frequency of the transmitted pulse and its second harmonic. Spectra from agent and tissue after filtering are shown in Figure 27c. For the data shown in this example, the harmonic filter increased agent to tissue contrast by 14.7 dB relative to the same data filtered at the fundamental. Figure 27d) to f) shows similar results for Optison at a higher transmit level (MI of 1.0). In this case, harmonic filtering increased the agent to tissue contrast by 17.1 dB compared to fundamental filtering.

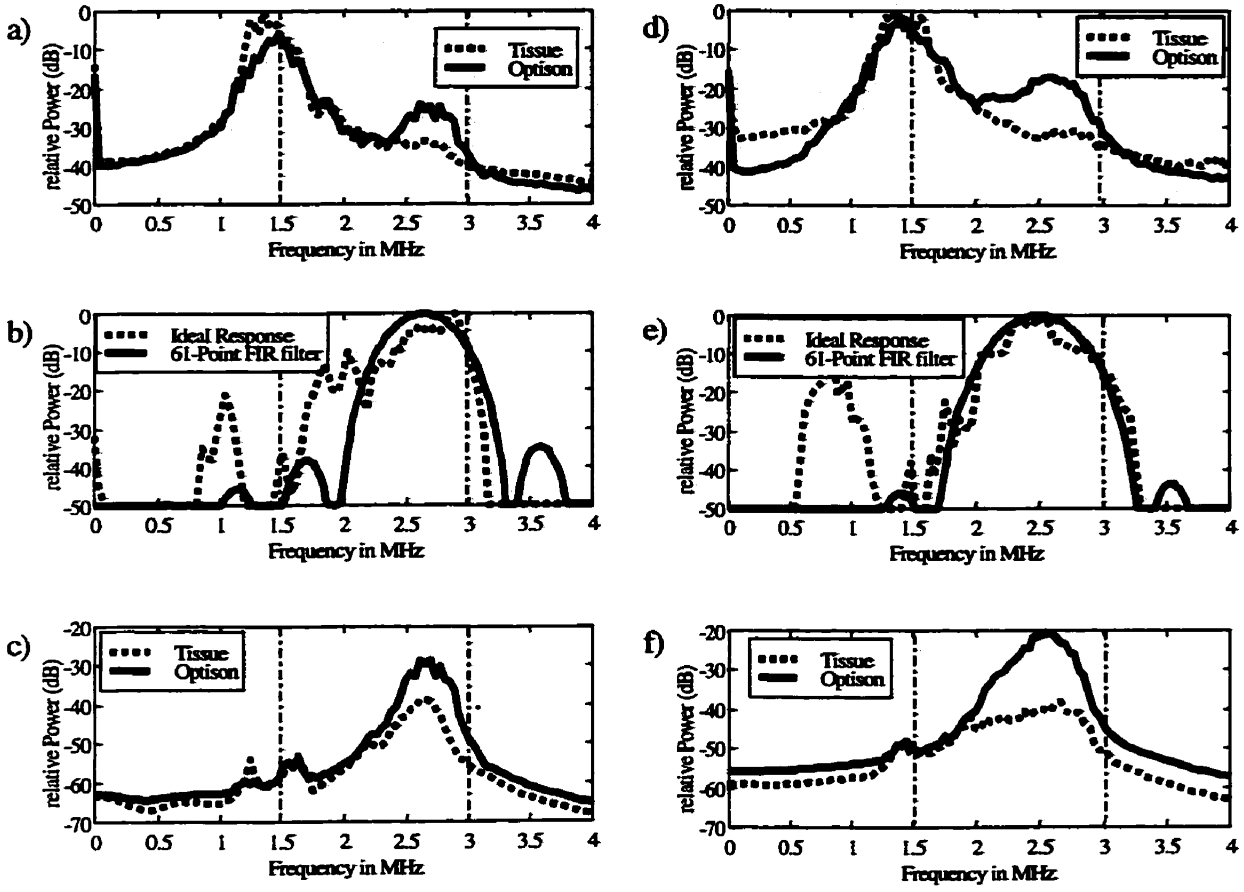

Figure 27: RF Filtering: a) RF spectra of echoes tissue (dotted line) and Optison (solid line) at an MI of 0.3; b) "ideal" frequency response from Equation 49 (dotted line) and the frequency response of a practical 61-point FIR filter; c) RF spectra of tissue and agent after filtering. d) – f) similar to a) – c) but for an MI of 1.0.

3.4.3 Doppler filtering

Examples of filters generated for harmonic Doppler imaging of Optison at an MI of 1.0 are shown in Figure 28a and Figure 28b. For the clutter filters, keeping the number of echoes processed (N) constant and changing the rank of the clutter space (M) produced different levels of myocardial enhancement (Figure 28c). The 1xN agent detection filters exceeded the performance of the best NxN clutter filters (Figure 28d), but exhibited more passband ripple. The complex-valued filters (not shown) produced marginal improvements over the corresponding real-valued filters, but had asymmetric passbands. For all designs, filter performance increased as more echoes were used for processing, but packet lengths of greater than 6 provided only marginal improvements.

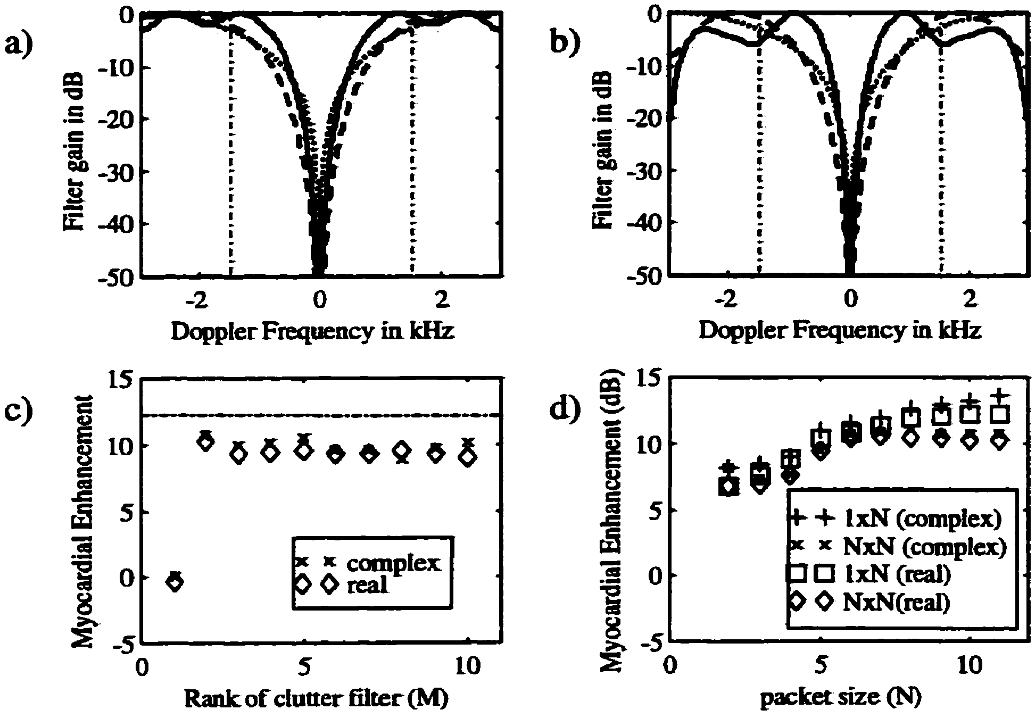

Figure 28: Filters for Conventional Doppler: a) Frequency responses of NxN harmonic Doppler clutter filters for Optison™ at an MI of 1.0 – lines are for packet lengths of 2 (dotted), 4 (dashed) and 8 (solid); b) frequency responses of 1xN agent detection filters for Optison™ at an MI of 1.0; c) Myocardial enhancement of 11-point clutter filters versus rank of filter; d) Myocardial enhancement vs packet size for clutter and agent detection filters

Doppler Filters for PID imaging at MIs of 0.13 and 1.0 are shown in Figure 29. At the lower MI, the Doppler filters were selective for nonlinear scattering, with passbands in the nonlinear portion of the Doppler spectrum and stopbands in the linear portion of the spectrum. At the higher MI, the Doppler filters were selective for microbubble disruption, with stopbands at +/- 3 kHz (the Nyquist frequency) and 0 Hz to eliminate both linear and nonlinear tissue echoes.

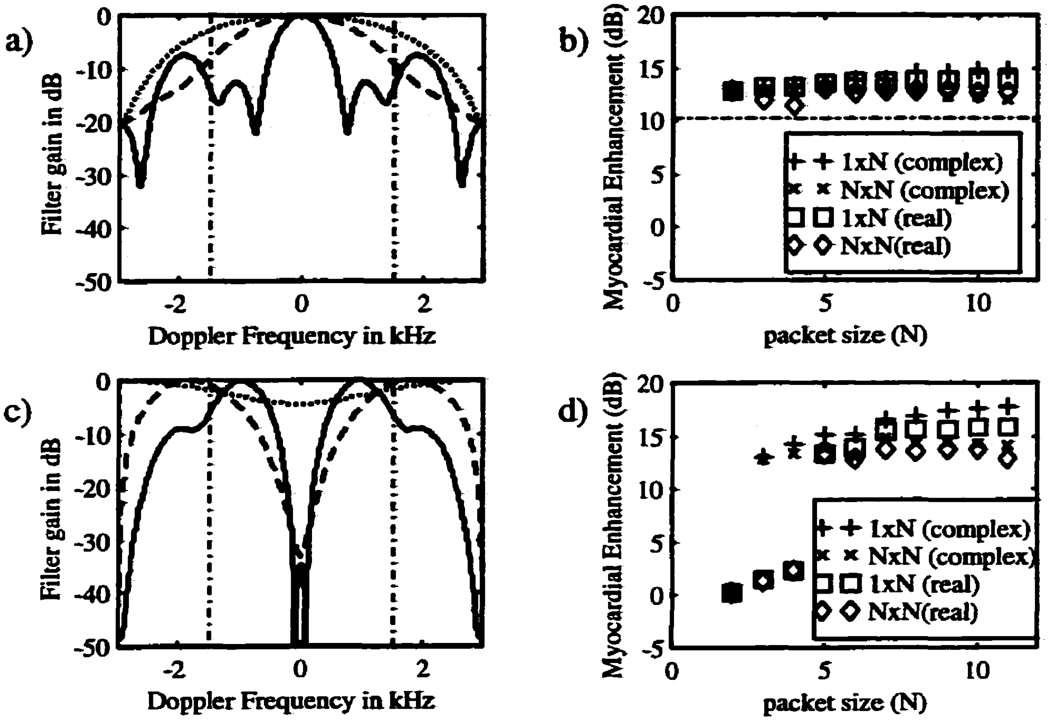

Figure 29: Filters for Pulse Inversion Doppler: a) Frequency responses of 2 (dotted), 4 (dashed) and 8 point (solid) 1xN agent detection filters for PID imaging of Optison™ at an MI of 0.13; b) Myocardial enhancement vs packet size for PID imaging of Optison™ at an MI of 0.13 – the dashed line represents the enhancement for 2-pulse pulse inversion imaging; c) Frequency responses of 2 (dotted), 4 (dashed) and 8 point (solid) 1xN agent detection filters for PID imaging of Optison™ at an MI of 1.0; d) Myocardial enhancement vs packet size for clutter size for PID imaging of Optison™ at an MI of 1.0

3.4.4 Coordinating RF and Doppler filtering

In the preceding analysis, RF and Doppler filtering were treated independently. To improve filtering, these filters may be designed together to take advantage of the correlation between the RF and Doppler components of microbubble and tissue echoes. By applying 2-dimensional (2D) Fourier transforms to the echo data arrays from each scanline and averaging the results, 2D spectra of echo power as a function of RF and Doppler frequency can be estimated (Wilson 1991). Figure 30 shows 2D spectra of conventional Doppler echoes from the entire heart before and after the administration of Optison at an MI of 1.0. Signal gain (echo power after injection divided by echo power before injection) is shown in Figure 30c. While for low Doppler shifts, signal gain was highest near the second harmonic, signal gain for high Doppler shifts appeared relatively uniform across the entire passband of the transducer. Such data illustrate the fact that rapidly disrupting microbubbles produce broadband RF echoes (de Jong 1997; Morgan et al. 1998), with large Doppler shifts at all RF frequencies. Conversely, tissue produces echoes with smaller Doppler frequency shifts at RF frequencies concentrated around the transmit frequency and, at higher transmit intensities, its second harmonic (tissue harmonics (Averkiou and Hamilton 1995; Christopher 1997)).

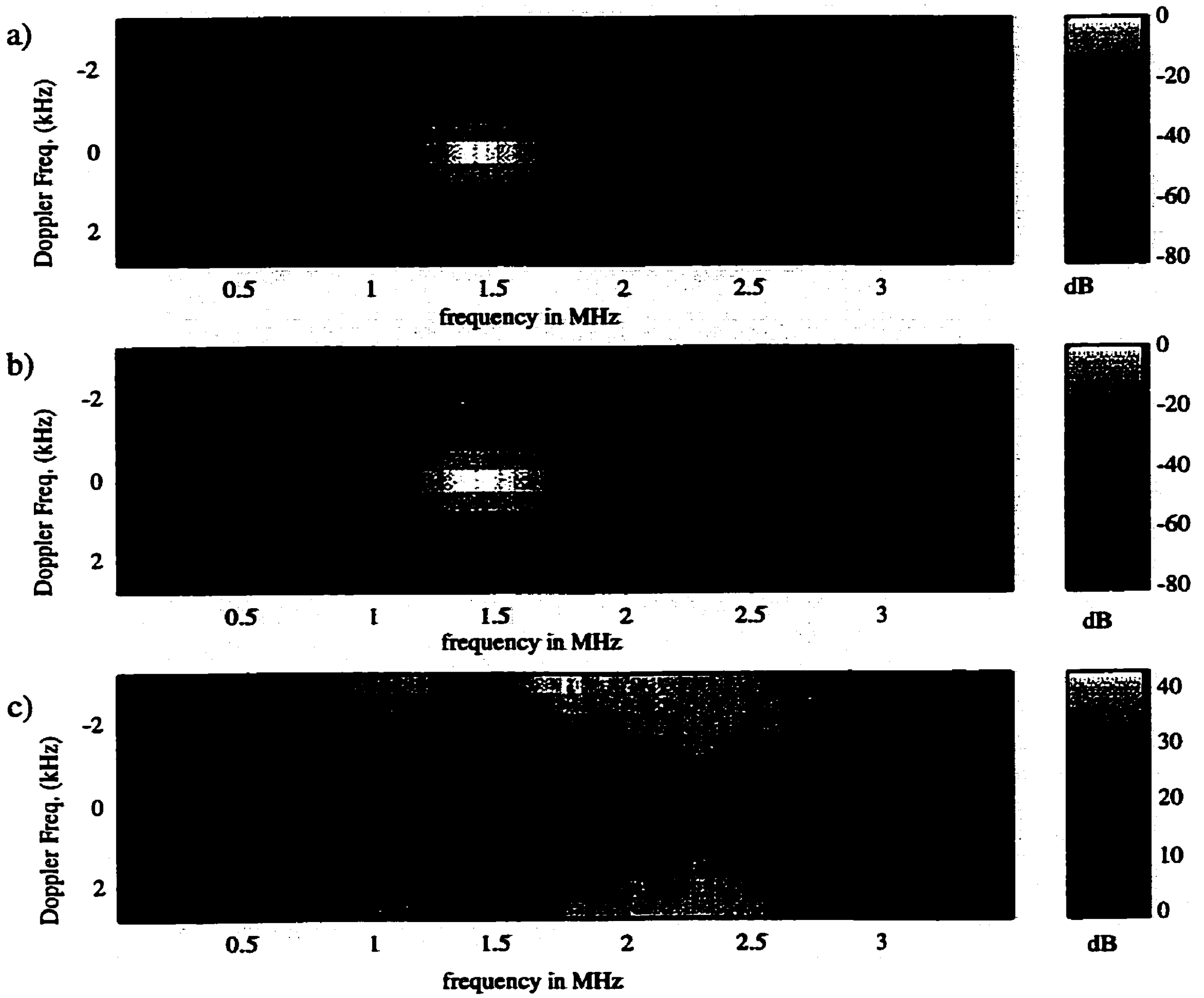

Figure 30: Intensity of Doppler echoes from the heart at an MI of 1.0 as a function of radio and Doppler frequency: a) baseline b) after the addition of 20 µl/kg Optison™; c) gain in signal strength vs radio and Doppler frequency.

A simple iterative procedure was developed to coordinate the choice of Doppler and RF frequencies. In this procedure, an RF filter was first developed according to Equation 49 and applied to pre and post injection RF echoes. The echoes were then demodulated and a Doppler filter was calculated according to Equation 56. After this first iteration, the Doppler filter was then applied to the raw RF echoes, and the entire procedure was repeated on the Doppler-filtered RF echoes. In most cases, two to seven iterations of this procedure were sufficient to produce coordinated RF and Doppler filters that significantly outperformed the combined filters from the first iteration.

Radio Frequency spectra of the data from Figure 30 are shown in Figure 31a and c before and after iterative Doppler filtering with a packet length of 11. The Doppler frequency response of the agent detection filter after 10 iterations is shown in Figure 31b. Myocardial enhancement increased from 13.3 dB in the first iteration to 17.1 dB in the sixth iteration (Figure 31d). In this instance, the optimal RF filters were actually centred about the transmission frequency rather than its second harmonic. This apparent paradox is related to the fact that harmonic filtering and Doppler filtering are both techniques for rejecting tissue clutter. For perfusion imaging at high MIs and sufficient packet lengths, Doppler processing alone was often able to eliminate clutter (Figure 31b). Harmonic filtering in these instances was redundant and only served to decrease the agent signal amplitude relative to the electronic noise from the transducer.

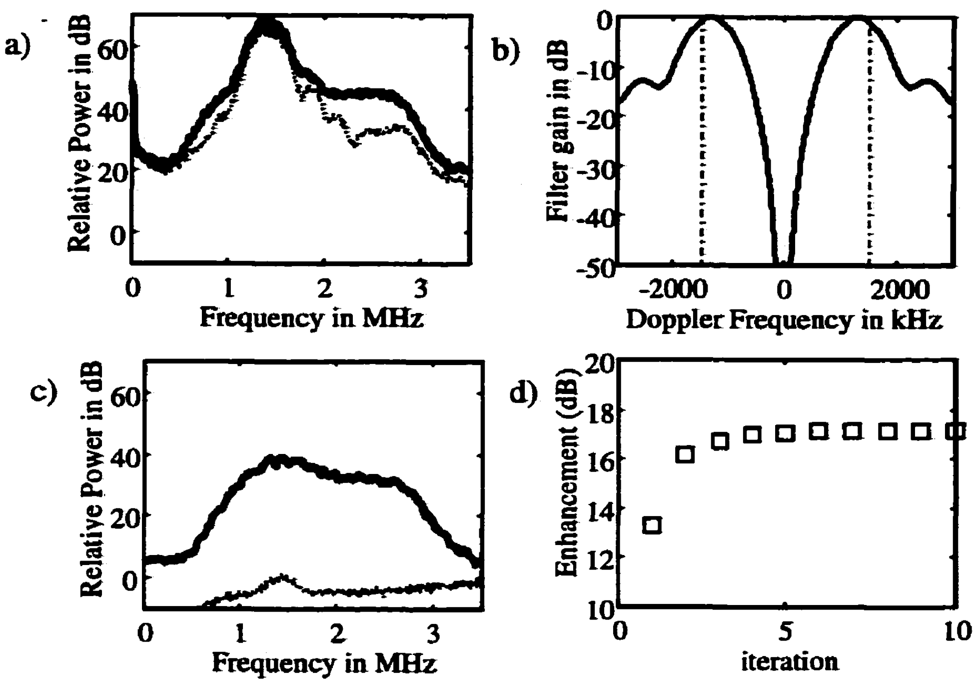

Figure 31: Coordinating RF and Doppler filters for conventional Doppler: a) RF spectra of unfiltered Doppler echoes from Optison and tissue at an MI of 1.0; b) frequency response of the optimized agent detection filter after 10 iterations; c) RF spectra (from a) after Doppler filtering with the optimized agent detection filter (from b); d) myocardial enhancement versus iteration.

When the iterative filter optimization was applied to pulse inversion data, it produced a variety of RF and Doppler filter combinations, depending on the transmit intensity. At an MI of 0.13, the iterative optimization improved myocardial enhancement by approximately 0.5 dB and produced filters similar to those produced by treating RF and Doppler components independently. At an MI of 1.0, the iterative procedure yielded RF filters with passbands centred at the transmit frequency and Doppler filters with stopbands to eliminate both the linear and nonlinear clutter components (Figure 32). In this case, the coordinated filters increased myocardial enhancement by 3.9 dB compared with the filters designed sequentially. In the corresponding images, enhancement was stronger and more uniform throughout the myocardium (Figure 33).

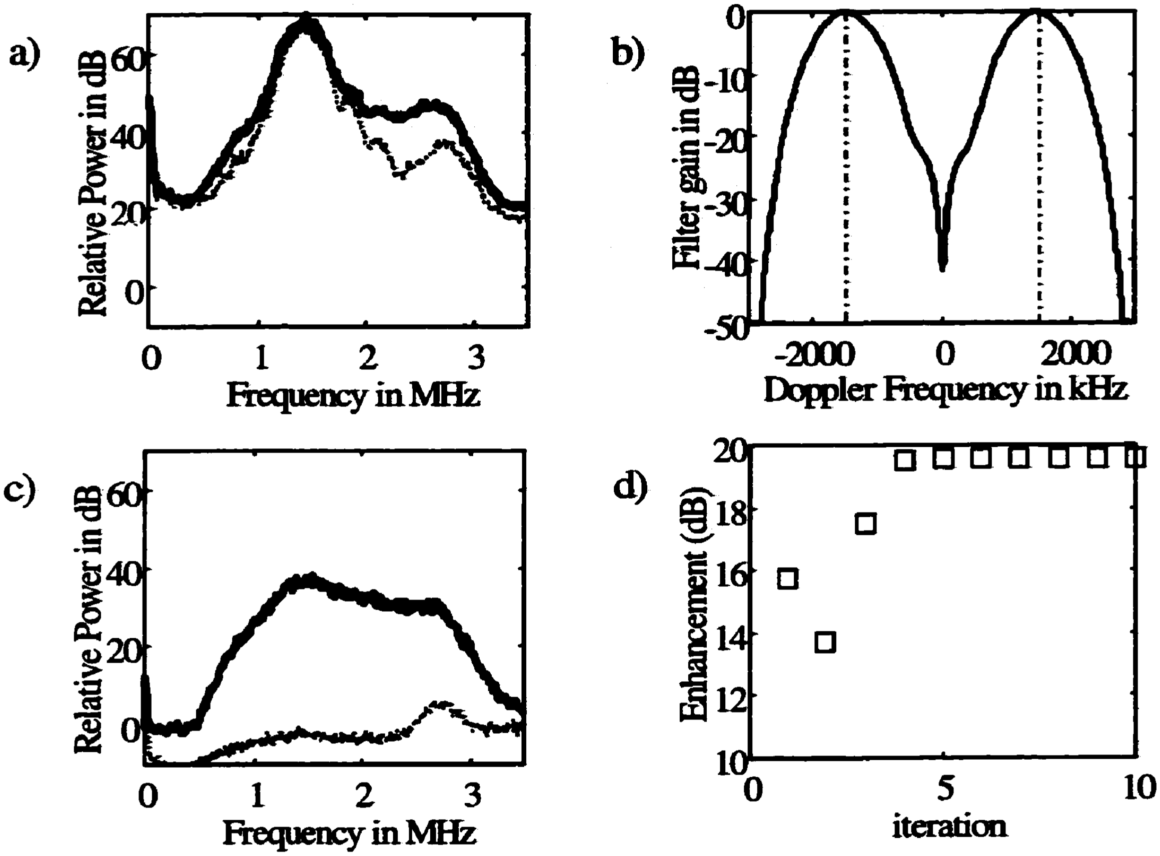

Figure 32: Coordinating RF and Doppler filters for P ID: a) RF spectra of unfiltered PID echoes from Optison and tissue at an MI of 1.0; b) frequency response of the optimized agent detection filter after 10 iterations; c) RF spectra (from a) after Doppler filtering with the optimized agent detection filter (from b); d) myocardial enhancement versus iteration.

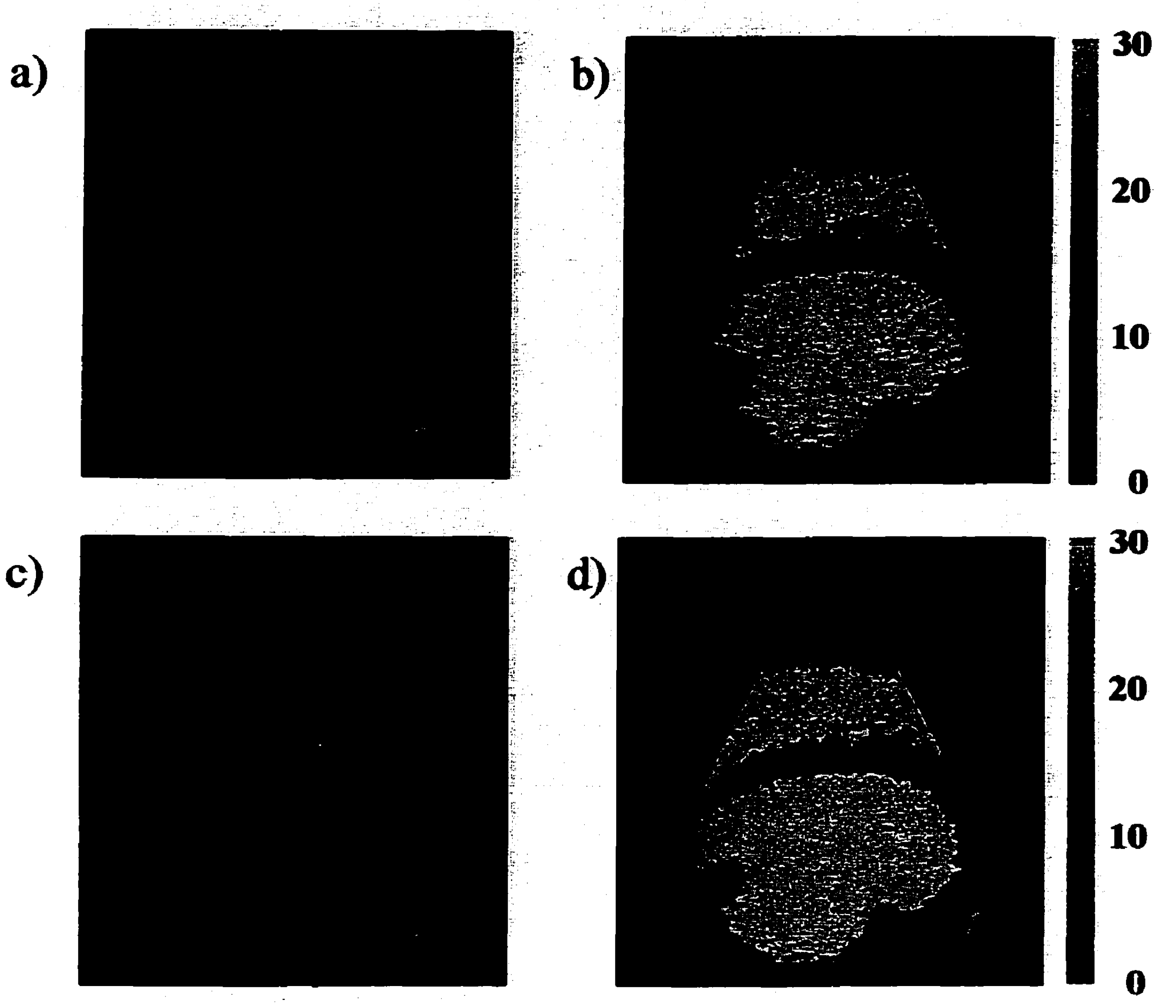

Figure 33: Fundamental vs Harmonic imaging: a) baseline and b) contrast enhanced harmonic PID images of heart at an MI of 1.0 made by optimizing RF and Doppler filters separately (colour dynamic range: 30 dB); c) baseline and d) contrast enhanced fundamental PID images of the heart made from the same data but using coordinated Doppler and RF filtering. In this case, fundamental imaging provided stronger and more uniform myocardial enhancement than harmonic imaging.

3.5 Discussion:

As new contrast agents and contrast-specific imaging techniques are developed, there will be a continuing need to adjust the RF and Doppler filtering for each combination of agent, technique and application. Moreover, a fair comparison of the various techniques can be performed only if the individual techniques have been optimized.

We have presented a coherent approach to contrast processing that uses the measured properties of contrast agents and tissue to generate RF and Doppler filters for perfusion imaging. One of the key advantages of this approach is that it does not require an explicit model of either the sound transmission or the scattering processes involved. This approach is sufficiently general to be used with a variety of imaging techniques including greyscale, conventional Doppler and pulse inversion Doppler techniques. Because the RF and Doppler filters described here can be generated with minimal operator intervention, they provide a relatively objective basis for the comparison of different transmission strategies. A similar approach to filter design has already been used to assess the performance of selected contrast agents and techniques for myocardial perfusion imaging (Hope Simpson and Burns 1998a).

This work has a number of implications for the development of contrast imaging strategies, since it highlights the fact that optimal detection methods are essentially predetermined for a given imaging task once the transmission scheme has been established. In particular, harmonic filtering arises as a natural consequence of the application of standard filtering techniques to the detection of contrast agents in tissue. It is most useful when Doppler filtering is not used or is not effective at removing tissue clutter, but becomes less necessary at high transmit intensities as Doppler filtering improves. Fundamental or broadband RF filtering may actually be preferred over harmonic RF filtering for intermittent perfusion imaging with high transmission power levels and large packet sizes. . Doppler and RF filters for pulse inversion imaging with Optison at low MIs should be tuned to detect nonlinear scattering at twice the transmit frequency (harmonic detection). At high transmit intensities, these filters should be tuned to detect broadband microbubble disruption and the RF filters should be moved *away* from the second harmonic. In all cases, Doppler and RF processing should be optimized together, rather than independently. These results demonstrate two things: first they support the intuitive model-based development of harmonic imaging and pulse inversion Doppler imaging, but secondly, they show that our intuition is not always correct. By letting the data "speak for themselves", we can eliminate potential biases. We are thus provided with an opportunity to revise our models and understanding of the physical processes involved whenever intuition and experimental results disagree. By demonstrating that the detection process is predetermined by the imaging conditions, this work focuses attention on the development of new ultrasound transmission strategies rather than detection schemes.

All of the filters presented in this Chapter were generated by automated routines that required minimal user intervention. Although these filters were generated for specific conditions, they should provide a good starting point for the development of filters for more general use. Eventually, it may be possible to incorporate some of these concepts into adaptive routines that update filter parameters during the course of an examination or imaging procedure (Bjaerum and Torp 1997). Doppler filtering using a simple weighted sum of the Doppler signal elements performed as well as more complicated matrix filtering techniques.

There are limitations to the present work. We have discussed the selection of RF and Doppler filters for perfusion imaging using conventional linear, separable filters. Other means of echo processing, such as thresholding and the use of joint RF/Doppler filters, have not been considered. Radio frequency filters have been designed to optimize agent to tissue contrast, and the effects on image resolution have been neglected. Doppler filter design has been restricted to the case of perfusion imaging where flow effects can be ignored. Although transmission parameters such as PRF, transmit pulse frequency and bandwidth will all affect image contrast and resolution, the choice of these parameters has not been examined methodically.

4 Myocardial Perfusion Imaging with Pulse Inversion Doppler

This Chapter has been submitted for publication as: Hope Simpson, D., Burns, P. N., and Averkiou, M. A. Myocardial Perfusion Imaging with Pulse Inversion Doppler and Microbubble Contrast Agents. Ultrasound in Medicine and Biology 2000 (manuscript UMB/2000/51). It has been edited for clarity and is reprinted with permission.

4.1 Introduction

This Chapter describes experiments performed to assess the performance of greyscale, power Doppler and pulse inversion Doppler imaging techniques for detecting myocardial perfusion *in vivo* at different incident power levels and with different agents. The techniques described in the previous chapter were used to optimize imaging techniques and to provide an objective comparison of the various methods. The goals of this work were to identify optimal methods for assessing myocardial perfusion under different operating conditions, and to investigate the possibility of realtime myocardial perfusion imaging.

4.2 Materials and Methods:

Experiments were conducted *in vivo* on two mongrel dogs (weighing approximately 22 kg and 24 kg respectively) on 5 separate study days. The handling and treatment of the dogs followed guidelines set forth by the Canadian Council on Animal Care and the Animals for Research Act. The protocol was also reviewed and approved by the hospital ethics committee. Following a 24 hour fast, each dog was premedicated with an intramuscular injection of acepromazine (0.5 ml kg^{-1}) and atropine (0.05 mg kg^{-1}). Anaesthesia was then induced with inhalation Halothane (5%) with oxygen via a facemask. after induction, each dog was intubated and maintained on inhalation halothane (0.8% to 1.5%) with oxygen for the duration of the experiment.

Three contrast agents were tested: Optison (MBI, San Diego,CA) is comprised of perfluoropropane gas bubbles (mean diameter: 3.9 μm) stabilized with a shell of denatured albumen (Skyba et al. 1996); DEFINITY (DMP-115) (Dupont Pharmaceuticals, Billerica, MA) is comprised of perfluoropropane bubbles (mean diameter: 2 μm) stabilized with a phospholipid shell (Kaul 1997); SHU 563A is comprised of air bubbles (99% with mean diameters between 0.1 and 4.0 μm) coated with a thin cyanoacrylate shell (Uhlendorf and Hoffman 1994). Agents were prepared according to the manufacturers' instructions. Unless otherwise noted, all agents were administered as bolus injections via a 3-way stopcock attached to an 18 gauge angiocatheter in a cephalic vein. Optison was administered in 0.3 ml or 0.5 ml boluses (13 to 20 μl kg^{-1}), Definity (DMP-115) was administered in 0.1 ml boluses (4 μl kg^{-1}), and SHU 563A was administered in 0.3 ml boluses (13 μl kg^{-1}). Each injection was followed immediately by a flush of approximately 2.0 ml of normal saline.

Microbubble kinetics were monitored continuously using real time Doppler dosimetry as described in Chapter 3. All ultrasound transmission and reception for imaging were performed with an ATL HDI-5000 ultrasound system (ATL Inc., Bothell, WA, USA) running experimental pulse inversion software. This system was equipped to provide access to the unprocessed radio frequency (RF) data, which could be down-loaded for offline processing. Note that all of the filters and image processing described in this paper were implemented by the authors and are not the same as those used for clinical imaging on the HDI-5000.

4.2.1 Dependence of Myocardial Contrast on Incident Pressure

Three of the five study days were devoted to an investigation of the effects of incident pressure on myocardial contrast. With the dog in a supine position, a P3-2 phased array scanhead was positioned to record a right parasternal short axis view of the heart, and clamped in place with a mechanical arm (Fisso, Switzerland). The use of this mechanical arm allowed the same field of view to be maintained indefinitely without operator intervention. Radio frequency colour frames of the heart (12 pulses per line, 1.67 MHz transmit frequency, and 6 kHz pulse repetition frequency) acquired before and after each injection using either conventional Doppler or pulse inversion Doppler transmission. In some cases, comparative data were also acquired using 2-pulse pulse inversion harmonic imaging. Image data were acquired using end-diastolic electrocardiogram-gated imaging at a rate of 1 frame per 3 heartbeats (approximately 0.5 Hz). The mechanical index (MI) was varied from 0.1 to 1.2, providing a range of incident peak negative pressures from approximately 0.12 to 1.5 MPa.

The Doppler densitometry measurements were used to synchronize the acquisition of the post injection frames to the plateau phase of Doppler enhancement following the first pass of the contrast bolus through the circulation. The Doppler data were also used to ensure that all post injection image data were acquired at comparable contrast concentrations.

Image and data analyses were performed offline using custom analysis routines written in MATLAB™(The Mathworks Inc., Natick, MA). The procedure used for analyzing all images was similar. Since the processed echoes from within the ventricles were often 12 to 25 dB stronger than the processed myocardial echoes, a procedure was developed to isolate the myocardial echoes. An edge detection routine was used first to identify the interface between the intraventricular septum and the left ventricle in the radio frequency echoes. All echoes were aligned so that this interface was at a constant depth. A rectangular region of interest (ROI), lying entirely within the septum, was then identified for perfusion measurements. A second ROI, lying entirely within the left ventricle and just distal to the septum was also identified. Fundamental and harmonic data were processed in parallel. For fundamental processing, the echoes were filtered with a bandpass filter centred at 1.5 MHz with a –6 dB bandwidth of 1.1 MHz, and then demodulated in quadrature. For harmonic imaging, a 0.8 MHz bandwidth filter centred at 2.8 MHz was applied to the data prior to demodulation.

To assess the performance of Doppler and pulse inversion Doppler techniques, Doppler clutter filters were generated directly from the measured echoes from each pair of pre and post injection images (Hope Simpson and Burns 1998a; Schleher 1991). These filters were designed to maximize the ratio of the Doppler power from the region of interest after injection (agent and tissue) to the Doppler power from the region of interest prior to injection (tissue alone). Separate Doppler filters were generated for fundamental and harmonic signals. Although 12 pulses were transmitted down each line of sight, the first echo from each line was discarded to reduce potential multi-path artifacts, and Doppler filters were applied to the remaining 11 echoes. The effects of imaging with fewer pulses per line were simulated by performing Doppler processing using only a subset of the available echoes from each line of sight. Figure 34 illustrates the principles of both pulse inversion and the Doppler wall filters. Second harmonic components from the first and second echoes are plotted against each other for echoes from the myocardium at an MI of 0.1, before and after the introduction of contrast agent (Definity (DMP-115), Dupont Pharmaceuticals, Billerica). The echoes from tissue are linear and lie along the line defined by $echo2 = -echo1$. Adding contrast agent introduces nonlinear harmonic components along the perpendicular line $echo2 = echo1$. Pulse inversion thus orthogonalizes the linear and nonlinear components of the returning echoes. The addition of the two echoes then acts as an agent detection filter that detects all echo components orthogonal to the line $echo2 = -echo1$.

After filtering, the myocardial enhancement in the region of interest was estimated as:

$$Enhancement(dB) = 10\log_{10}\left[\frac{\text{Mean Doppler Power After Injection}}{\text{Mean Doppler Power Before Injection}}\right] \qquad 57$$

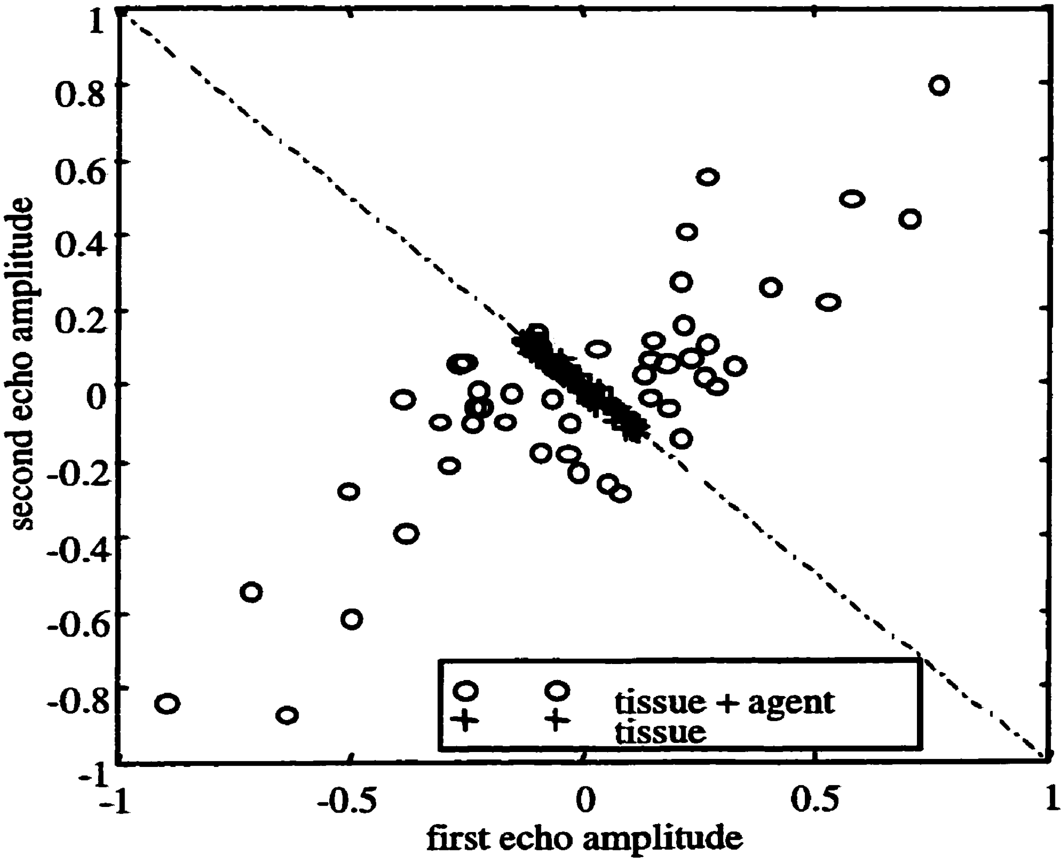

Figure 34: Pulse inversion imaging orthogonalizes linear and nonlinear components of the harmonic signal. First and second echo harmonic signals are plotted against each other for echoes from tissue (canine myocardium, crosses) and tissue containing contrast agent (Definity (DMP-115) in canine myocardium, circles) at a mechanical index of 0.1. Summing the two echoes acts as a Doppler filter that cancels all components parallel to the dashed line.

In addition to filtering the echoes at 1.5 MHz (to detect the fundamental component) and 2.8 MHz (to detect the harmonic component), a search routine was employed to find the optimal combination of radio frequency and Doppler filtering for each pair of images. The centre frequency of the radio frequency filter was stepped from 1.4 MHz to 3.0 MHz in increments of 0.1 MHz, and Doppler filters and corresponding myocardial enhancement were calculated at each stage. Once the optimal centre frequency was found, the bandwidth was also varied from 0.8 MHz upwards and Doppler filters and enhancement were recalculated. The optimal enhancement and filters were recorded.

4.3 Results

4.3.1 A Note on the Bandwidth of Radio Frequency Filters

Although the bandwidths of the radio frequency filters were varied in these experiments, the most narrowband filters tested (0.8 MHz) produced the strongest enhancement and were used in all cases. The tradeoffs between bandwidth and resolution were not investigated.

4.3.2 Pressure Dependence of Myocardial Enhancement with Optison

The dependence of myocardial enhancement on incident pressure following 20 μl kg^{-1} bolus injections of Optison is shown in Figure 35, for intermittent greyscale imaging and also for pulse inversion imaging with 2, 6 and 11 pulses per line. Figure 35 shows similar results for 11-pulse intermittent power Doppler imaging. In each case, Doppler filters were adjusted separately at each mechanical index. For the "optimized" case, RF filters were also adjusted separately at each power level.

At the lowest incident pressures (MI < 0.4), pulse inversion Doppler with second harmonic filtering provided the highest levels of enhancement, producing 10 to 12 dB more enhancement than Doppler and harmonic greyscale imaging. Doppler filters were selective for the nonlinear scattering component of the PID spectrum. At the 6 kHz PRF used in the pulse inversion Doppler imaging, the use of more than two pulses per line of sight did not produce a statistically significant increase in enhancement over the 2-pulse method. As the incident pressure was increased, the enhancement from 2-pulse PID imaging decreased. Above an MI of approximately 0.4, harmonic 2-pulse PID imaging and harmonic greyscale imaging produced similar levels of enhancement (dashed lines in Figure 35a, b).

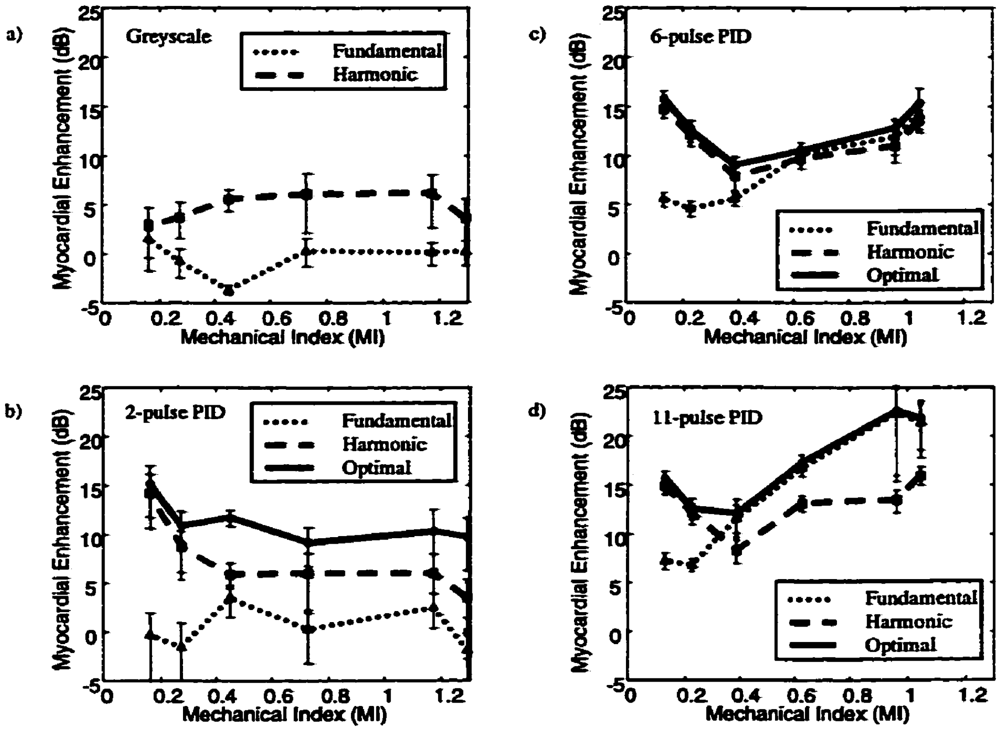

Figure 35: Myocardial enhancement following the administration of 20 µl/kg of Optison for a) Greyscale imaging; b) 2-pulse pulse inversion Doppler; c) 6-pulse pulse inversion Doppler; and d) 11-pulse pulse inversion Doppler. The separate lines represent results with fundamental (dotted), harmonic (dashed) and optimized RF filtering (solid). Each data point represents the mean enhancement over the region of interest for a single bolus injection, imaged at one frame per 3 heartbeats.

As expected, myocardial enhancement with Doppler imaging increased steadily with increasing pressure (Figure 36). The enhancement with 11-pulse PID also increased with pressure above a mechanical index of 0.4 (Figure 35d). At mechanical indices above 0.4, both Doppler and PID filters selected for disruption-induced Doppler spectral broadening. For Doppler and PID imaging with 11 pulses per line, the optimal radio frequency filters at high mechanical indices were centred at the transmitted frequency, not its second harmonic. Further investigation revealed a tradeoff between several competing factors; the optimum contrast between agent and electronic noise occurred at the fundamental whereas the optimum contrast between agent and tissue occurred at the second harmonic. As the number of pulses processed was increased from 2 to 11, the optimum receive frequency moved from the second harmonic to the fundamental, revealing a switch from tissue-limited to electronic noise-limited enhancement as Doppler filtering improved (Figure 37). These results using fewer than 11 pulses should be treated with caution, since 12 pulses were transmitted in all cases. Especially at high mechanical indices, this may have produced unnecessary microbubble disruption, reducing agent concentrations unnecessarily.

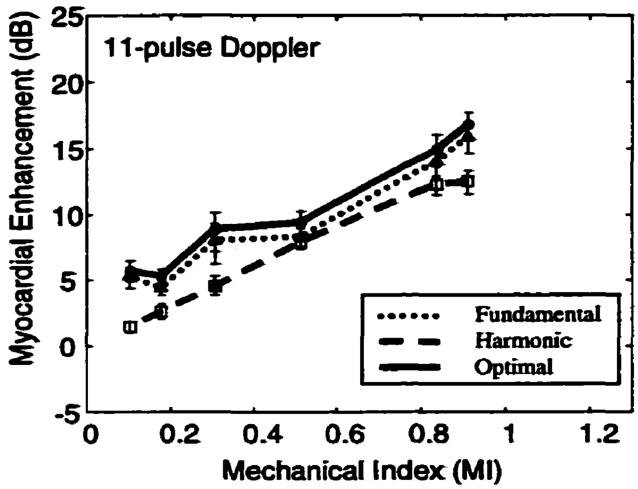

Figure 36: Myocardial enhancement following the administration of 20 μl/kg of Optison for 11-pulse Doppler imaging. The separate lines represent results with fundamental (dotted), harmonic (dashed) and optimized RF filtering (solid). Each data point represents the mean enhancement over the region of interest for a single bolus injection, imaged at one frame per 3 heartbeats.

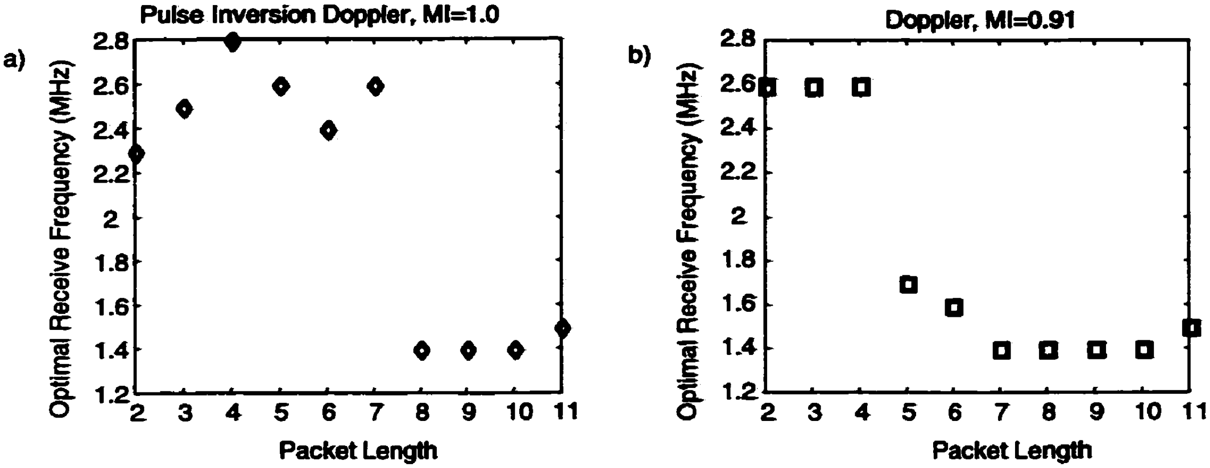

Figure 37: Optimum receive frequency vs packet length for a) pulse inversion Doppler imaging at MI=1.0; b) Doppler imaging at MI=0.91. As more pulses were used per line of sight, the optimal filter frequency dropped from the second harmonic, to the fundamental.

The optimal radio frequency filter frequency for 2-pulse PID imaging decreased with increasing incident pressure, shifting from approximately 2.6 MHz at the lowest pressures (MI<0.4) to approximately 2.2 MHz at higher incident pressures (MI >0.4). This shift in frequency to a point half way between the fundamental and harmonic at high incident pressures occurred in response to two separate phenomena. At high incident pressures, nonlinear scattering from microbubbles produced broadband echoes, detectable across the entire passband of the transducer. There was also a concomitant increase in the tissue harmonic signals. By placing the receive filter frequency half way between the fundamental and second harmonic, the broadband microbubble echoes were detected while both the linear and nonlinear echoes from tissue were suppressed (Figure 38).

Baseline and contrast-enhanced pulse inversion Doppler images of the heart at low and high mechanical indices are shown Figure 39.

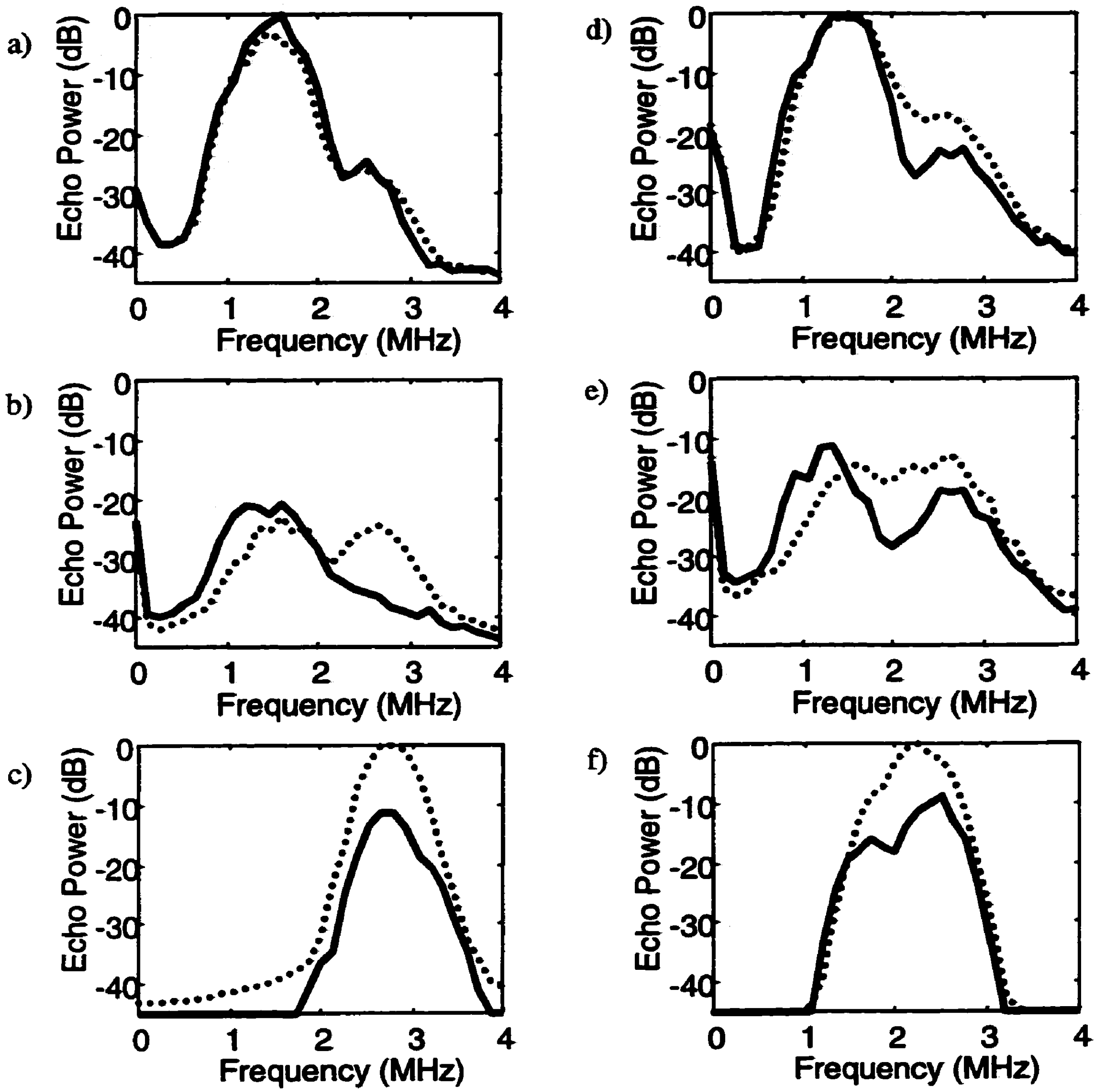

Figure 38:RF Filtering for pulse inversion at low and high transmit intensities: a) Radio frequency spectra of unprocessed echoes from myocardium (solid line) and myocardium + Optison (dotted line) at a mechanical index of 0.13; b) spectra of the same echoes after 2-pulse pulse inversion Doppler filtering; c) spectra after pulse inversion Doppler and radio frequency filtering; d)-f) same as a)-c) but at MI=1.3. At low incident pressures, RF filters should be placed at the second harmonic of the transmit frequency. At high incident pressures, RF filters should be placed between the fundamental and second harmonic frequencies.

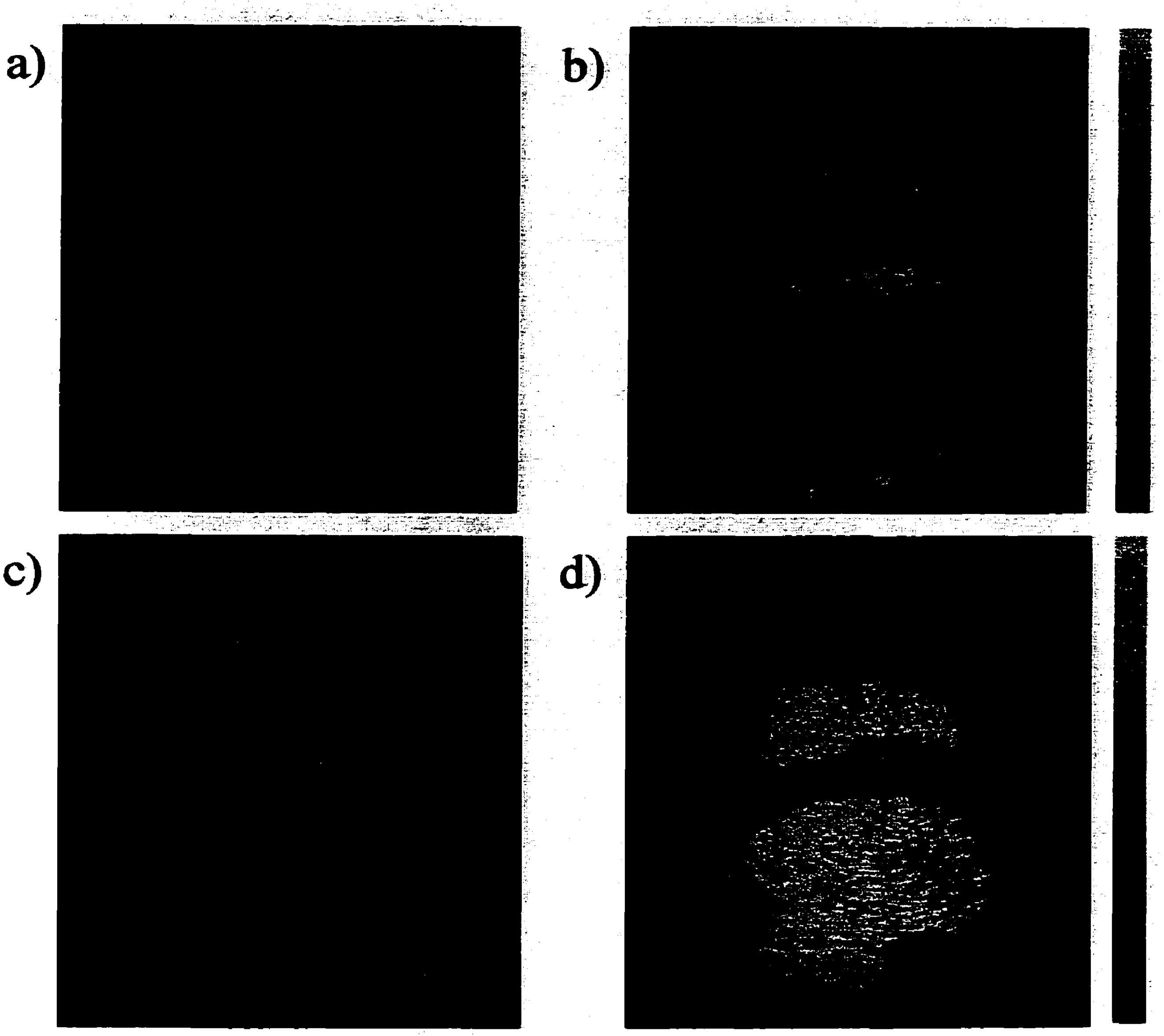

Figure 39: Right parasternal short axis images of the heart made with 11-pulse pulse inversion Doppler at a frame rate of 1 frame per 3 heartbeats: a) baseline image at MI=0.2; b) following a bolus injection of 20 μl kg^{-1} of Optison at MI=0.2; c) baseline image at MI=1.0; d) following a bolus injection of 20 μl kg^{-1} of Optison at MI=1.0. In all images the dynamic range of the colour overlay is 40 dB. Pulse inversion Doppler can detect myocardial perfusion at both low and high incident pressures.

To demonstrate the effects of microbubble disruption, data were acquired at MIs of 0.3 and 1.3 with 2-pulse pulse inversion Doppler at 1 frame per 3 heartbeats and also in realtime at 13 frames/second (Figure 40). While myocardial enhancement was detectable at both MIs with intermittent imaging, realtime myocardial enhancement at a mechanical index of 1.3 was undetectable due to agent disruption. More significantly, realtime myocardial enhancement was detectable at the lower mechanical index. By avoiding excessive microbubble disruption, pulse inversion Doppler imaging at low incident power levels offers the opportunity of imaging myocardial perfusion in realtime.

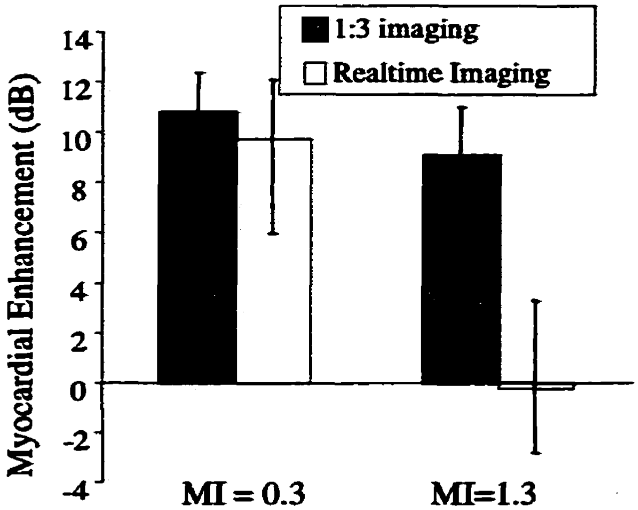

Figure 40: Myocardial enhancement with Optison (20 μl kg^{-1}) for 2-pulse pulse inversion Doppler for intermittent imaging at 1 frame per 3 heartbeats (filled bars) and 13 frames per second (open bars). Myocardial enhancement can be detected in realtime with pulse inversion Doppler at low incident pressures.

The effects of varying both the Doppler pulse repetition frequency (PRF) and ensemble length at low transmit pressure were simulated by taking the 12-pulse PID data and processing every echo (6 kHz PRF), every 3rd echo (2 kHz PRF), etc. and then processing a subset of the remaining echoes using optimized RF and Doppler filtering. For packet lengths of 2, 3 and 4 echoes, myocardial enhancement increased with increasing PRF (Figure 41a). At low PRFs, enhancement with the 2-pulse method suffered due to tissue motion, and using just three pulses per line of sight improved enhancement significantly. With the 0.8 MHz bandwidth harmonic receive filters, myocardial enhancement using 4 pulses per line was indistinguishable from the 3-pulse results at 2 kHz and 6 kHz. The radio frequency spectra of agent and tissue echoes following 2 and 4-pulse PID filtering are shown in Figure 42. When the processing described above was repeated with a broadband receive filter (2.7 MHz centre frequency, 2.2 MHz bandwidth), the myocardial enhancement with 2-pulse imaging decreased at low PRFs as more of the fundamental echoes from moving tissue were detected (Figure 41b). Here again, myocardial enhancement was improved significantly by using 3 or more pulses and appropriate Doppler filtering.

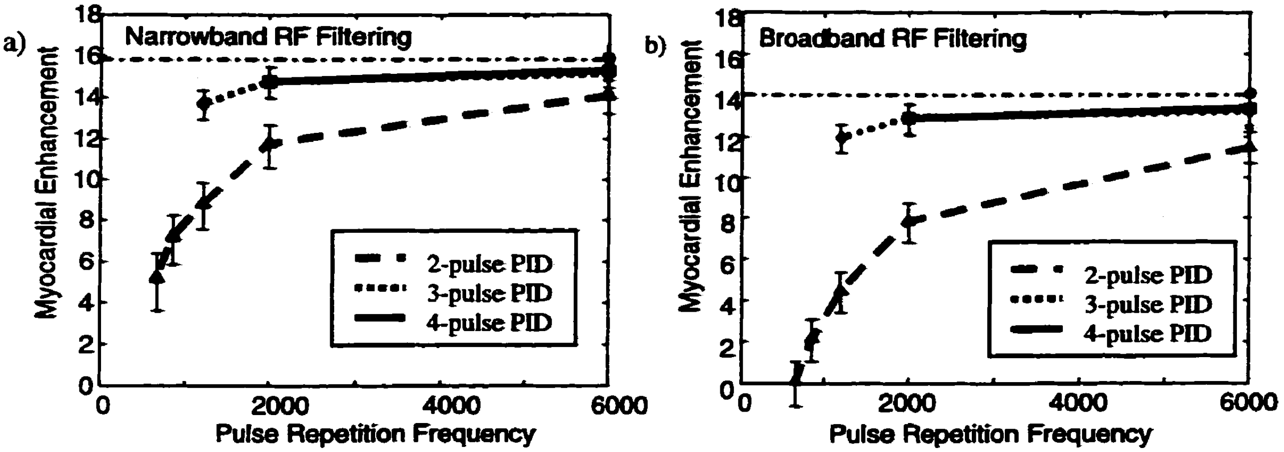

Figure 41: a) Myocardial enhancement versus PRF at MI=0.13 for pulse inversion Doppler with narrowband harmonic filtering using 2 pulses (dashed line), 3 pulses (dotted line) or 4 pulses per line (solid line). The dash-dot line represents the enhancement with 11 pulses per line at a PRF of 6 kHz. Myocardial enhancement increased as more pulses and higher PRFs were used. Using as few as 3 pulses per line produced strong enhancement at most pulse repetition frequencies. b) Myocardial enhancement versus PRF at MI=0.13 for pulse inversion Doppler with a broadband receive filter.

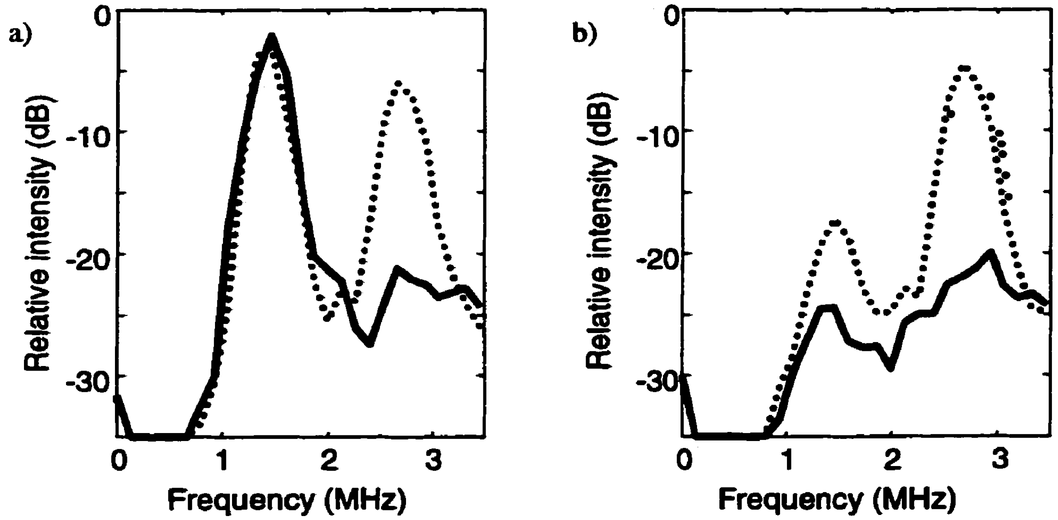

Figure 42: Radio frequency spectra of Doppler-filtered echoes from myocardium (solid lines) and myocardium+Optison (dotted lines) for a) 2-pulse PID; and b) 4-pulse PID. Using more than two pulses helped to suppress the fundamental echoes from moving tissue.

4.3.3 Other Agents

On 2 of the 5 study days, experiments were conducted with other agents to assess the generality of the observations discussed above.

The pressure dependence of myocardial contrast following 0.1 ml (4 µl kg^{-1}) injections of Definity (DMP-115) is shown in Figure 43, for pulse inversion Doppler with 11 pulses per line. Like Optison, this agent consists of perfluoropropane bubbles surrounded by a flexible shell. Results with PID imaging were similar to those from Optison, with optimal contrast provided by harmonic pulse inversion imaging below an MI of approximately 0.4, and by fundamental Doppler at higher MIs.

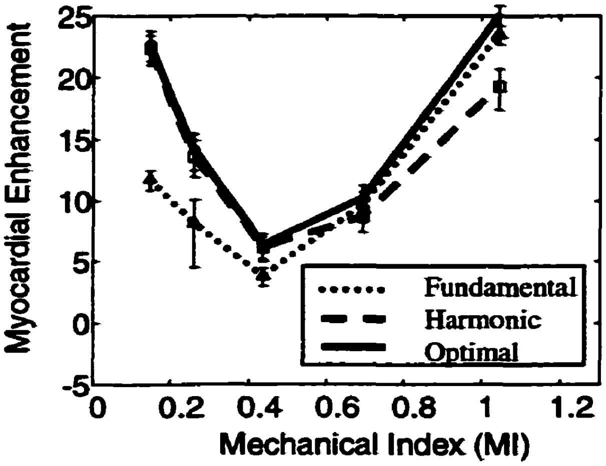

Figure 43: Myocardial enhancement versus mechanical index with 11-pulse pulse inversion Doppler (1 frame per 3 heartbeats) following bolus injections of Definity (DMP-115) (4 µl kg^{-1}). The separate lines represent results with fundamental (dotted), harmonic (dashed) and optimized RF filtering (solid).

Experiments were also conducted on Sonavist. The pressure dependence of myocardial contrast for 11 pulse Doppler and pulse inversion Doppler imaging is shown in Figure 44a and Figure 44b respectively. This agent is comprised of polymer encapsulated air bubbles that dissolve rapidly when disrupted by high intensity ultrasound. At the incident pressure levels tested, it was detected best with conventional Doppler. Since the lowest mechanical index tested was approximately 0.3, the behaviour of this agent *in vivo* at low incident intensities remains to be explored. At high incident pressure levels and despite the high PRFs used in the experiments, the Doppler shifts produced by microbubble disruption produced aliasing between the two components of the pulse inversion Doppler spectrum, reducing the effectiveness of this technique. A similar pattern of behaviour was observed with Levovist (Schering AG, Berlin), another air-based agent.

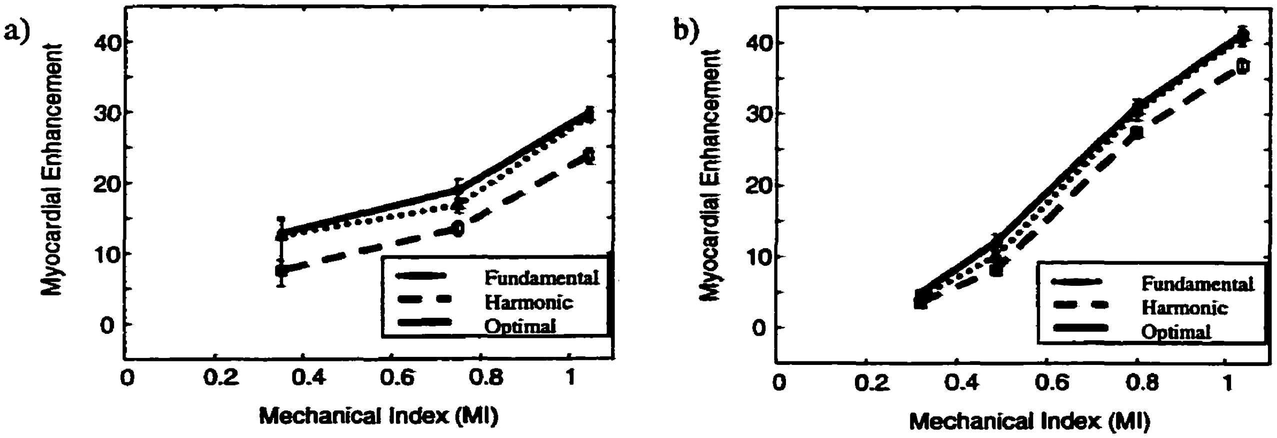

Figure 44: Myocardial enhancement versus mechanical index following bolus injections of SHU 563a (12 µl kg^{-1}) with a) 11-pulse pulse inversion Doppler; and b) 11-pulse conventional Doppler (all at 1 frame per 3 heartbeats). The separate lines represent results with fundamental (dotted), harmonic (dashed) and optimized RF filtering (solid).

4.4 Discussion and Summary

We have shown that pulse inversion techniques, tuned to detect second harmonic nonlinear scattering, can significantly outperform other contrast-specific imaging techniques at low incident sound pressures, potentially enabling myocardial perfusion to be detected with realtime imaging when used in conjunction with the perfluorocarbon agents tested. Here, use of the highest possible pulse repetition frequencies together with effective second harmonic filtering can minimize the deleterious effects of tissue motion. If imaging depth prohibits the use of high PRFs and second harmonic filtering is not sufficient to suppress tissue motion, then motion effects may be reduced significantly by transmitting more than two pulses per line of sight and using appropriate Doppler filtering. At higher incident sound pressures, imaging techniques should be designed to detect Doppler spectral broadening caused by microbubble disruption. Here, the choice of whether to use fundamental or second harmonic radio frequency filtering will depend upon the effectiveness of Doppler frequency filtering. The multi-pulse Doppler and pulse inversion Doppler techniques can provide significantly more myocardial enhancement than two-pulse pulse inversion Doppler at high incident pressures.

Although a short axis view of the heart was used to detect myocardial perfusion in these experiments as a matter of convenience, this is probably not the optimal view for such measurements. Agent-induced attenuation in the left and right ventricles in this view limited our ability to assess perfusion distal to the left ventricle in these experiments. The use of an apical 2 or 4-chamber view in these experiments would have placed the majority of the myocardium between the transducer and the ventricles, reducing the effects of attenuation.

5 Clinical Applications of Pulse Inversion Doppler

The following figures in this Chapter have appeared in print or have been submitted for publication, and are used with permission:

Figures 50 and 51 originally appeared in: Burns, P. N., Wilson, S. R., and Hope Simpson, D. Pulse Inversion Imaging of Liver Blood Flow: Improved Method for Characterizing Focal Masses with Microbubble Contrast. Investigative Radiology 2000; 35(1):58-71, as Figures 10 & 12 respectively.

Figure 58 originally appeared in Burns, P. N., Hope Simpson, D., and Averkiou, M. A. Nonlinear Imaging. Ultrasound Med Biol 2000a; 26(1001):S19-S22, as Figure 3.

5.1 Introduction

The development of ultrasound contrast agents, harmonic imaging, and contrast-specific imaging techniques has opened up many new applications for diagnostic ultrasound imaging and has provided potential benefits for existing applications. Since pulse inversion Doppler combines harmonic imaging and Doppler contrast detection techniques, it offers benefits in many areas. Rather than attempting to catalog the possible uses of pulse inversion techniques, three applications of particular interest have been selected for review: quantification of myocardial perfusion, the assessment of blood flow in liver masses, and tissue harmonic imaging. The role of pulse inversion Doppler imaging in each application is discussed. The principles of operation underlying these applications may be extended readily to other areas.

5.2 *Quantifying Myocardial Perfusion*

5.2.1 Intermittent Doppler Imaging

When diagnostic ultrasound imaging systems were first used to image microbubble contrast agents, it was quickly realized that the microbubbles could be destroyed by high intensity sound pulses, and that the subsequent return of microbubbles into the ultrasound beam could be used to measure blood flow (Figure 45)(Fowlkes et al. 1998). It was not until recently, however, that a practical blood flow measurement technique was developed.

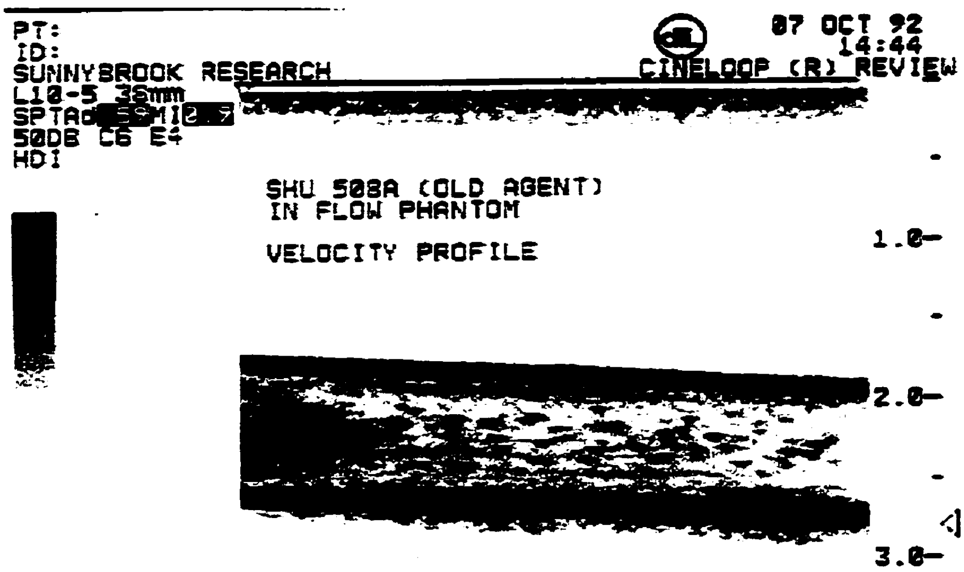

Figure 45: An early attempt to measure blood flow using microbubble disruption. Microbubbles flowing from left to right through a tube have been destroyed in the image plane by the imaging pulses. The degree of reflow of bubbles into the image plane between frames is proportional to velocity, yielding a profile of flow in this vessel phantom (unpublished).

In a 1998 paper, Wei et al. described an indicator dilution technique for measuring myocardial blood flow using microbubbles. In this technique, a single frame of high intensity power Doppler ultrasound pulses is used to image and destroy all of the microbubbles lying within the scan plane during a constant intravenous infusion of microbubbles (Wei et al. 1998). A second image frame is acquired soon afterwards, providing an image of only those microbubbles that have entered the scan plane between frames. By varying the time delays between successive frames and plotting the Doppler power signal from a given image location against time, a concentration versus time curve may be constructed for agent reperfusing the scan plane (Figure 46). Experimental results show that these concentration data may be fitted to the function:

$$C(t)=\alpha(1-e^{-\beta t}), \qquad 58$$

where $C(t)$ is the agent concentration (as measured by Doppler power), and α and β are fitted parameters. Theory, supported by preliminary experimental results, suggests that initial slope of this curve, $\alpha\beta$, will be proportional to the rate of blood flow into the scan plane, and the final asymptote, α, will be proportional to blood volume. The use of this technique is demonstrated in Figure 47.

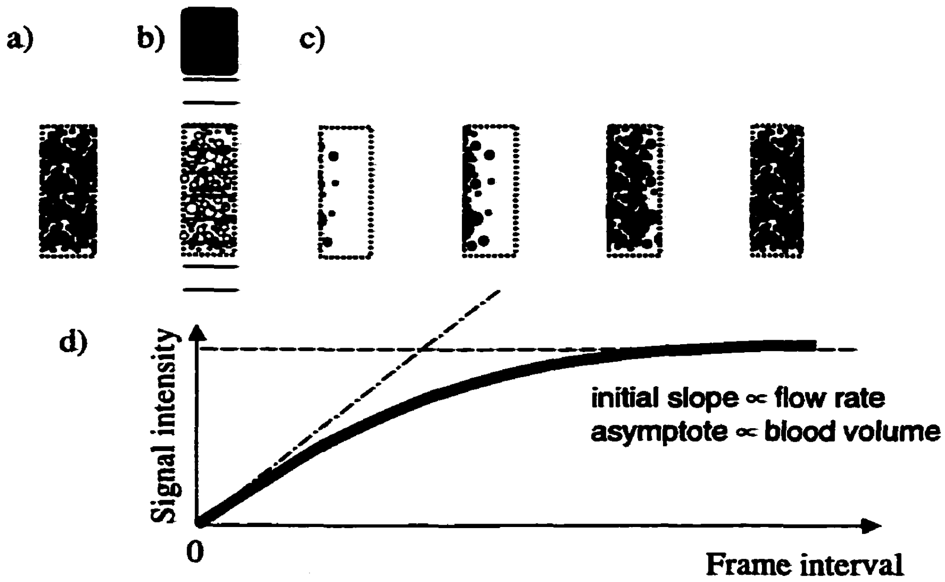

Figure 46: Principles of destruction/reperfusion flow measurement: a) steady state bubble concentrations are established in the blood; b) ultrasound is used to destroy microbubbles in the scan plane; c) over time, blood flow refills the scan plane with bubbles; d) the relationship between signal intensity and frame interval may be used to estimate blood flow and volume.

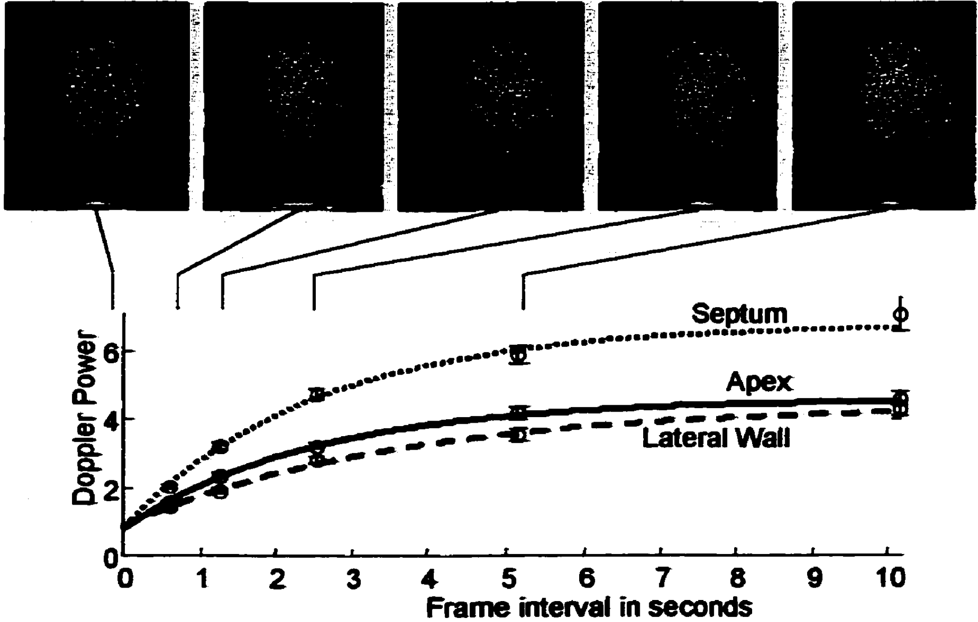

Figure 47: Destruction/reperfusion measurements of myocardial bloodflow in a dog heart using an infusion of Levovist (Burns et al. 2000b).

To provide absolute measurements of blood flow and volume with intermittent Doppler imaging, the effective thickness of the scan plane and the absolute detection sensitivity to microbubble concentration must be known at each point in the image plane. In practice, neither of these parameters is known. This technique can thus be used only to provide relative comparisons of blood flow between adjacent regions of tissue.

5.2.2 Limitations of Intermittent Doppler Measurements

In addition to providing only relative measures of blood flow, the intermittent imaging technique described above suffers from other drawbacks related to the speed of imaging. Firstly, since this technique requires intermittent imaging, myocardial perfusion and wall motion cannot be assessed together. Secondly, in a typical measurement of blood flow with this technique, 4 image frames might be acquired at each of 1, 2,4, 8 and 16 heart beat time delays. This corresponds to 20 frames in a total measurement period of 124 heart beats, or just under two minutes of imaging time. Since this interval on the order of the enhancement time provided by the infusion of a single vial of contrast agent, a separate vial of agent would likely be required for each measurement. Any significant movement of the transducer relative to the patient over this interval would invalidate the measurement.

We have recently demonstrated a potential source of measurement bias with this technique in an animal model (Burns et al. 2000b). For accurate measurements, the concentration of microbubbles in the blood outside of the scan plane should remain constant. Because the imaging plane often includes the ventricles, however, bubble disruption within the ventricles significantly reduces the microbubble concentration in the aortic blood. This process leads to a systemic reduction in microbubble concentration that is proportional to the frame rate, so that frames acquired at short time intervals contain fewer microbubbles than would otherwise be expected. At present, the clinical significance of this artifact is unclear.

5.2.3 Realtime Myocardial Perfusion Imaging with Pulse Inversion:

In the previous chapter we showed how real time perfusion imaging was possible with pulse inversion techniques operating at low transmit intensities. Realtime, low power, pulse inversion Doppler myocardial perfusion imaging has recently been introduced for clinical use (Power Pulse Inversion (PPI), ATL Ultrasound, Bothell, WA) (Averkiou et al. 2000). Baseline and enhanced images of a dog heart made at 8 frames per second with real time PPI are shown in Figure 48. In the contrast-enhanced image, perfusion is demonstrated throughout the moycardium surrounding the left ventricle. Some Doppler artifacts are visible in the baseline image, but these are primarily restricted to prominent interfaces (such as the endocardial border) and are unlikely to be misinterpreted as perfusion. With PPI, perfusion images may be obtained at rates well over 15 frames per second by adjusting imaging parameters (sector width, pulse repetition frequency, etc.). Power pulse inversion imaging thus allows myocardial perfusion and cardiac wall motion to be assessed simultaneously in real time. Preliminary trials in humans confirm these results and show that myocardial perfusion and perfusion defects can be detected with this technique (Tiemann et al. 1999).

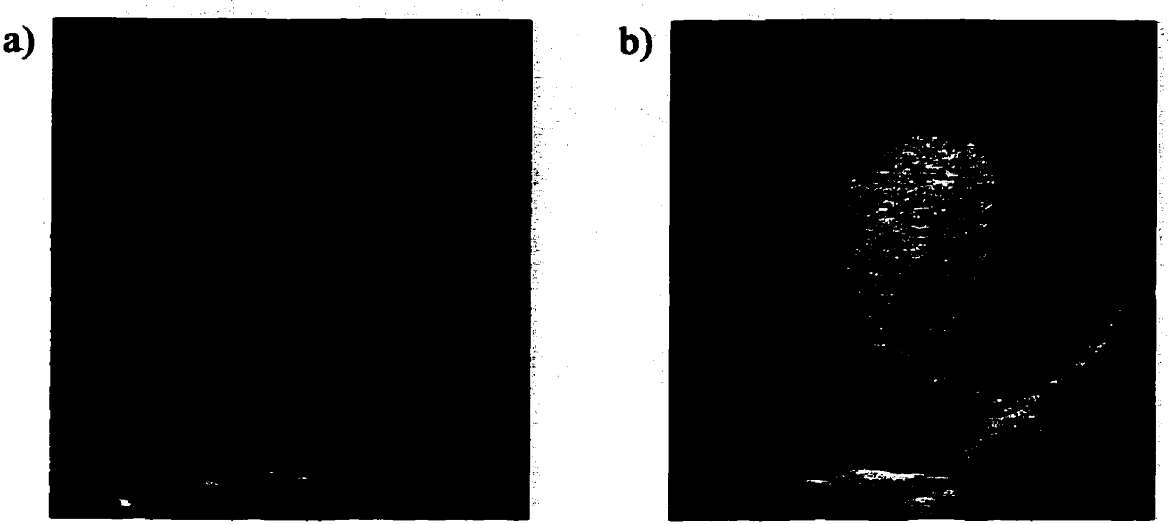

Figure 48: Apical 4-chamber images of a dog heart made with real time PPI imaging a) before; and b) after the intravenous bolus adminstration of Definity (18 μl/kg). In the enhanced image, myocardial perfusion is visible throughout the myocardium with realtime imaging.

5.2.4 Measuring Perfusion with Pulse Inversion

Because it does not disrupt microbubbles, low power pulse inversion imaging measures moving blood volume, not flow rate. While moving blood volume may often be adequate to assess myocardial perfusion abnormalities (Kaul and Jayaweera 1997), volume flow rates are also of interest. The destruction/reperfusion measurements of blood flow described in the preceding section have been adapted for use with the realtime PPI imaging. In a technique known as "flash" imaging, the clinician first identifies a region of interest using realtime scanning. Next, a rapid sequence of high intensity destruction frames is triggered, which disrupts all of the microbubbles within the scan plane. The system is then reset automatically to low power PPI imaging and the flow of agent into the scan plane is monitored in realtime. Several hundred image frames may be acquired over a 20 second time period and agent concentration (measured by PPI) vs time may be fitted to Equation 58 to estimate blood flow

(Figure 49). Compared with the intermittent Doppler method described previously, this method allows up to 10 times the data to be acquired in 1/5 the imaging time. Trials with these techniques are ongoing.

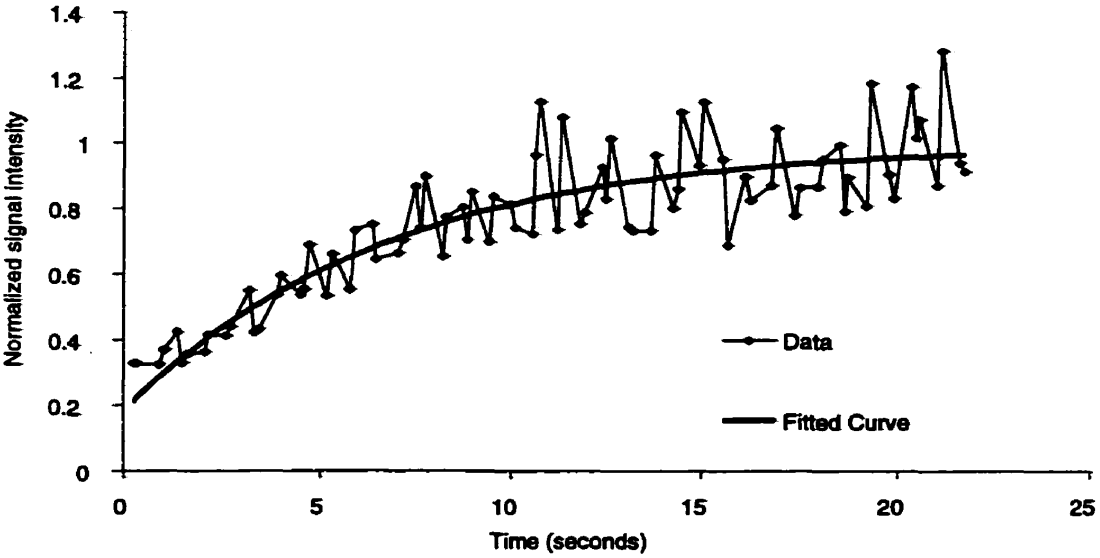

Figure 49: Destruction/reperfusion flow measurements in the intraventricular septum of a dog heart made using real time PPI imaging and an infusion of Definity (Dupont Pharmaceuticals, Billerica, MA) (data from diastolic frames only are shown). Because of measurement artifacts (resulting partially from thresholding and log compression of the Doppler data), intensity measurements have actually been fitted to a curve of the form: intensity = $\gamma + \alpha(1-e^{-\beta t})$*. Intensity values have then been normalized to the asymptotic value of the fitted curve.*

5.3 Blood Flow in Liver Masses

One of the major areas of interest in contrast imaging, outside of cardiac imaging, is the detection and diagnosis of liver masses. Primary liver cancer, or hepatocellular carcinoma (HCC), is one of the most prevalent cancers worldwide. Due in part to its role as a filter for blood, the liver is also a common site for metastases from colon cancer and other cancers including breast and lung cancer.

In cancer, the development of new blood vessels around solid tumours (angiogenesis) provides these tumours with nutrients required for growth and also with a pathway for the systemic spread of the cancer (metastasis) (Folkman 1995). These new blood vessels are abnormally tortuous and often contain direct connections between artery and vein (anastomoses) with abnormally high blood velocities (Balen et al. 1994; Burns et al. 1982; Taylor et al. 1997; Taylor 1995). Tumour vessels also tend to lack normal vasomotor tone and blood flow is largely unregulated (Cosgrove 1996). Whereas the blood supply of normal liver parenchyma is predominantly from the portal vein, many liver cancers including hepatocellular carcinoma are supplied primarily by the hepatic artery. The abnormal patterns of blood flow and vessel morphology in liver tumours aid their detection and differentiation with imaging techniques such as contrast assisted MRI and CT imaging (Stevens et al. 1994).

Efforts are now underway to determine whether microbubble contrast agents can enable the vascular features of liver tumours to be detected and differentiated with ultrasound (Girard et al. 1998; Tanaka et al. 1995). Since the diagnostic criteria are different from those in cardiac imaging, imaging techniques, too, will be different. Spatial resolution is much more important in liver imaging than in cardiac imaging (where extended perfusion defects are of primary interest. Resolution is required to delineate blood vessel morphology and to define the borders of lesions accurately. Since the colour overlays used in Doppler based techniques tend to mask the underlying anatomical information, greyscale techniques such as harmonic imaging are preferred. The Doppler settings designed for blood detection also produce gross saturation artifacts when used to image microbubbles. For these reasons, greyscale, 2-pulse, pulse inversion imaging (as described in Chapter 2) is the preferred technique for liver imaging with contrast microbubbles (Burns et al. 2000c). This technique provides high resolution and contrast sensitivity and does not use a colour overlay. At low transmit intensities, realtime pulse inversion imaging enables contiguous segments of tumour vasculature to be seen with high resolution (Figure 50). At high transmit intensities, intermittent pulse inversion imaging can be used to provide both blood flow and blood volume weighted images using the principles outlined in Section 5.2.1 (Figure 51).

Figure 50: Pulse inversion harmonic images of a large biopsy-proven hepatocellular carcinoma: a) baseline image—the tumour is a large round mass (M); b) contrast-enhanced image showing long tortuous vessels within the tumour; c) a high MI image after a delay shows enhancement surrounding a dark region within the tumour, indicating an area of necrosis (Burns et al. 2000c).

Harmonic imaging and pulse inversion imaging actually appear to benefit from the fact that they don't entirely eliminate signals from tissue. Especially at high incident sound intensities, nonlinear sound propagation causes nonlinear tissue echoes to appear in the harmonic signal (see Section 5.4). These weak tissue signals serve as the background image in contrast harmonic and pulse inversion imaging.

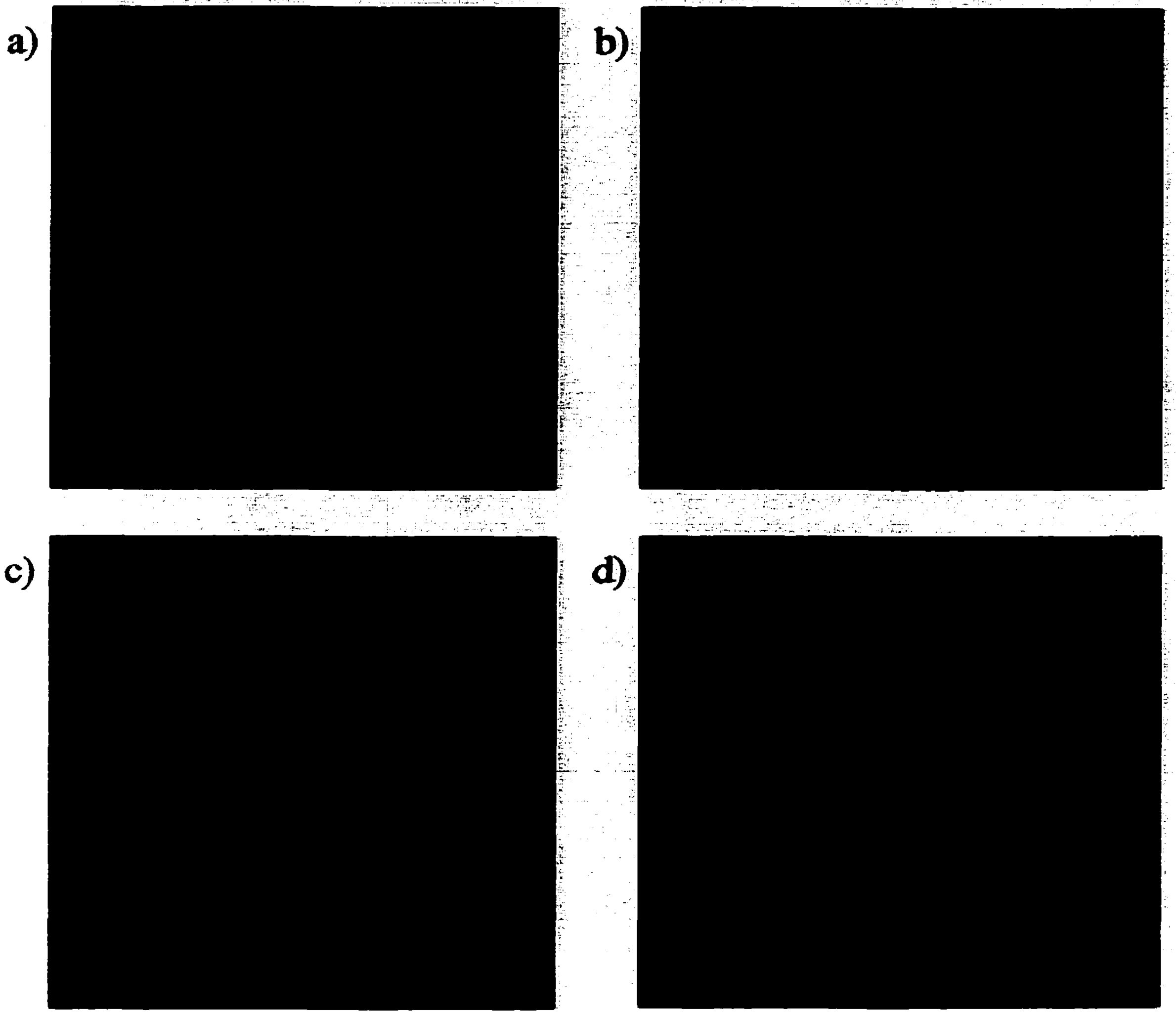

Figure 51: Pulse inversion harmonic images of a metastatic carcinoid—vascular metastasis: a) baseline image showing a large echogenic tumour containing hypoechoic necrotic regions; b) following a bolus injection of Optison with real time imaging, blood vessels are visible within the tumour and a second vascular lesion is now visible (arrow); c) with high MI imaging and a short frame interval, the lesion appears hyperechoic relative to the liver parenchyma, indicating a high flow rate; d) with high MI imaging and a longer frame interval, the lesion appears hypoechoic relative to the liver parenchyma, indicating a lower blood volume than the surrounding parenchyma (Burns et al. 2000c).

5.3.1 Levovist Late Phase Imaging

In addition to acting as blood pool enhancing agents, several contrast agents including Levovist and Sonavist (both from Schering AG, Berlin) demonstrate a late phase of enhancement in the liver. Although the exact mechanism for this late enhancement is unclear, it appears to involve either the phagocytosis of microbubbles by macrophages of the reticuloendothelial system (Kupffer cells), or the slow transit of microbubbles through the liver sinusoids (Blomley et al. 1999a; Blomley et al. 1999b; Kono et al. 2000). Whatever the mechanism, this enhancement is absent in many tumours, offering a means of distinguishing tumours from normal liver parenchyma. To image late phase enhancement, microbubbles are administered intravenously. Following a 5 to 10 minute delay, the liver is imaged with high intensity pulse inversion imaging or harmonic power Doppler imaging. Tumours appear as signal voids within the liver (Figure 52). Although power Doppler imaging is more sensitive than pulse inversion imaging (2-pulse) at high transmit intensities (See Chapter 4), pulse inversion appears to provide enough contrast to identify lesions, and offers a clearer view of the underlying tissue.

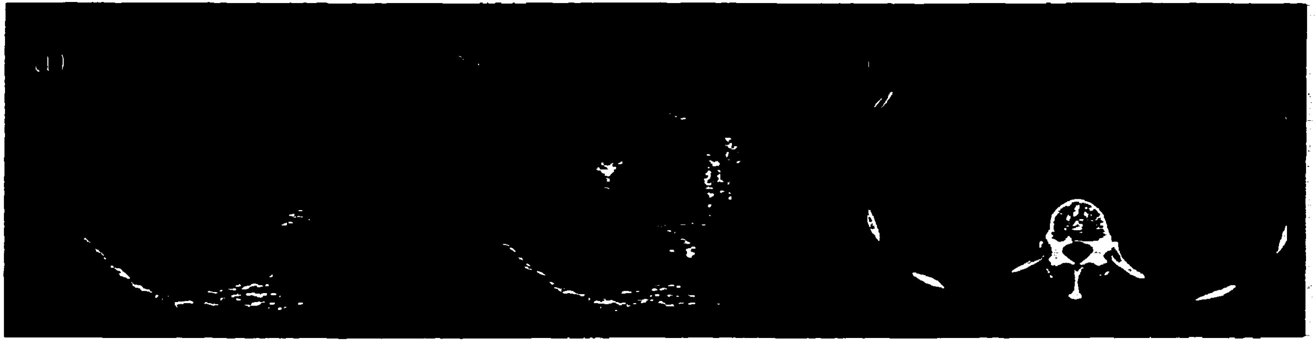

Figure 52: Metastatic adenocarcinoma a) baseline image showing an abnormal liver; b) Levovist-enhanced late phase pulse inversion image – contrast is much higher than at baseline, and small satellite lesions are now visible; c) confirmatory CT scan. Note the concordance between the CT and ultrasound images (images courtesy Dr. S. R. Wilson, Dr. P.N. Burns).

5.4 Tissue Harmonic Imaging

When harmonic imaging and Doppler techniques were first developed, in the early 1990s, the scattering of sound from tissue was commonly treated as a linear process. The echoes from tissue, thus, were expected to contain only those sound frequencies present in the transmitted pulses. Experiments performed with the prototype harmonic imaging systems quickly revealed that tissue echoes contained significant sound energy at the second harmonic of the transmitted frequency. These "tissue harmonic" components actually developed in the outgoing pulses as the sound propagated through tissue. Their intensity relative to the fundamental frequency components increased with distance and sound intensity – hallmarks of a well-understood process known as nonlinear propagation. While tissue harmonic echoes place fundamental limits on the performance of contrast harmonic imaging schemes, they can be exploited to provide improved tissue images (Averkiou and Hamilton 1997; Christopher 1997; Ward et al. 1997).

5.4.1 Nonlinear Propagation

In linear sound theory, the speed of sound, c_{sound}, is assumed to be independent of the sound intensity (see Chapter 1, Equation 4). This assumption is valid only for low intensity sound waves. For finite amplitude sound waves, the phase velocity (the propagation speed of a point of constant particle velocity) is a function of particle velocity. Two physical effects, the pressure dependence of compressibility (material nonlinearity) and convective nonlinearity, contribute to this effect.

The material nonlinearity results from a nonlinearity in the equation of state (the relationship between pressure and density) of the material. When compressed, the bulk compressibility of most materials decreases, making it progressively harder to compress them further. This effect causes the speed of sound to increase with increasing sound pressure. In a propagating sound wave, regions of high pressure correspond to regions of high particle velocity, so that:

$$c_{sound} = c_0 + \frac{B}{2A}u, \qquad 59$$

where c_0 is the low intensity speed of sound (approximately 1540 m/s in tissue at 37 C), u is the particle velocity of a point in tissue, and B/A is a material constant.

The convective nonlinearity results from the fact that the phase velocity is the sum of the local speed of sound and the particle velocity (Leighton 1994)[6]:

$$\text{Phase velocity} = c_{sound} + u \qquad 60$$

Summing the two contributions, we get

$$\begin{aligned} \text{Phase velocity} &= c_0 + \left(1 + \frac{B}{2A}\right)u, \\ &= c_0 + \beta u \end{aligned} \qquad 61$$

where β is referred to as the coefficient of nonlinearity. Values of β for different tissues range from 3.6 for water to approximately 6.5 for fat (Law et al. 1985).

As a result of the non-uniform phase velocity described by Equation 61, regions of high pressure in a sound wave (corresponding to regions of high particle velocity) propagate faster than regions of low pressure. This variation in propagation speed causes a gradual "steepening" of the sound wave as it travels, distorting the wave and shifting sound energy away from the transmitted frequency into higher harmonics (Figure 53). The rate of development of the second harmonic component is proportional to the square of the pressure amplitude of the propagating wave (Fry and Dunn 1962). Since scattered sound is typically of much lower intensity than the transmitted beam, nonlinear propagation affects primarily the outgoing sound wave.

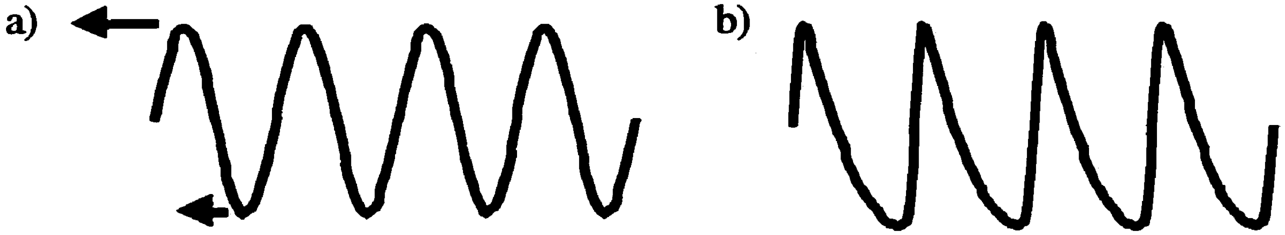

Figure 53: a) Sketch of an ultrasound wave propagating to the left; b) as the wave propagates, nonlinear propagation causes the high pressure regions of the wave to travel faster than the low pressure regions, distorting the sound wave.

---

[6] This convective component may be explained by analogy with a travelling airplane. The airplane's ground speed (phase velocity) is equal to the its air speed (c_{sound}) plus the wind velocity (u).

5.4.2 Characteristics of the Nonlinear Beam

Figure 54 shows sketches of two-way (transmit/receive) sensitivity patterns for a focussed ultrasound transducer operating in fundamental and harmonic imaging modes. In fundamental imaging (Figure 54a), the transducer is most sensitive at its focus, but is also sensitive to scattering near the skin surface. Sound reverberating in layers of fat and muscle near the skin surface can therefore produce imaging artifacts in fundamental mode. In harmonic imaging (Figure 54b), the nonlinear beam is not present near the skin surface, but develops as the sound propagates (Averkiou and Hamilton 1995; Averkiou and Hamilton 1997; Christopher 1997). Hence, reverberation artifacts from scattering in superficial layers are suppressed.

Figure 54: a) Sketch of the two-way sensitivity pattern for conventional imaging; b) sketch of the two-way sensitivity pattern for tissue harmonic imaging. Tissue harmonic imaging is insensitive to scattering from superficial layers.

Figure 55 shows a sketch of the fundamental and harmonic beam profiles at the transducer focus. In addition to having a broad main lobe on the beam axis, the fundamental beam has strong off-axis components, or sidelobes. These sidelobes diverge from the main sound beam and scatter off tissue. The ultrasound system interprets echoes from sidelobes as coming from structures along the beam axis, producing artifacts in the resulting image. Because it is at twice the transmit frequency, the harmonic beam has a narrower main lobe, which results in improved lateral resolution. More significantly, the harmonic beam is produced primarily along the beam axis where sound intensity is highest. It therefore has lower sidelobes and generates correspondingly weaker sidelobe artifacts (Averkiou and Hamilton 1997).

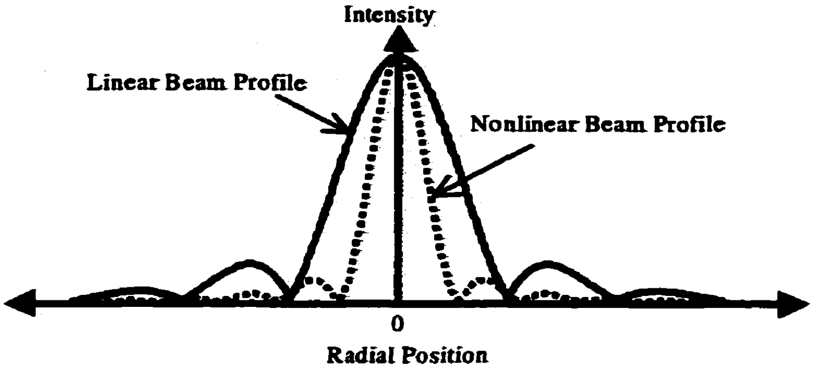

Figure 55: Sketch of the fundamental and harmonic beam profiles at the transducer focus. The harmonic beam has a narrower main lobe and lower sidelobes than the fundamental beam.

Trans-thoracic cardiac imaging, where harmonic imaging was first used, is particularly prone to the imaging artifacts mentioned above. Many patients suffering from ischemic heart disease are overweight, and have significant layers of fat and tissue at or near the skin surface that can generate reverberation artifacts in conventional imaging. Also, since sound cannot pass through bone and air, small gaps between the ribs and lungs must be used as "acoustic windows" for viewing the heart. The phased-array ultrasound transducers used to image the heart through these windows produce particularly significant sidelobes, which can reflect off the nearby ribs and lungs, generating sidelobe artifacts. Before the introduction of tissue harmonic imaging, a significant fraction of cardiac ultrasound examinations were considered non-diagnostic due to poor image quality resulting from sidelobe and reverberation artifacts. It is precisely such "difficult" examinations, which appear to be improved by tissue harmonic imaging (Kremkau et al. 1998).

Tisssue harmonic imaging is now used widely in cardiac ultrasound imaging, and is available on most modern cardiac ultrasound systems. Following its success in cardiology, harmonic imaging has also been applied to radiological imaging, where it has been shown to improve visualization of low contrast lesions and cystic structures (Tranquart et al. 1999)(Burns et al, 2000).

5.4.3 Pulse Inversion Tissue Harmonic Imaging

Like the nonlinear harmonics generated by microbubbles, tissue harmonics result from an asymmetric response to regions of high and low pressure in the transmitted sound. Not surprisingly, therefore, pulse inversion harmonic imaging detects tissue harmonic echoes in addition to bubble harmonic echoes.

Calibrated hydrophone measurements of high intensity normal and inverted sound pulses measured at the focus (8.8×10^{-2} m) of the Picker 3.5 MHz transducer used in Chapter 2, following excitation with a single cycle tone burst at 3.5 MHz and transmission through water are shown in Figure 56a and b. The positive and negative portions of the sound waves are distorted assymetrically for both pulses. Assuming that the scattering and reflection processes do not cause further distortions, we may use these pulses to simulate the detected tissue echoes. Summing the two pulses isolates the asymmetric components of the echoes (Figure 56c), while subtracting the two pulses isolates the symmetric echo components (Figure 56d). Spectral analysis of the sum and difference signals shows that these signals contain the even order and odd order harmonic components respectively (Figure 57), as predicted in Chapter 2 for bubble harmonics.

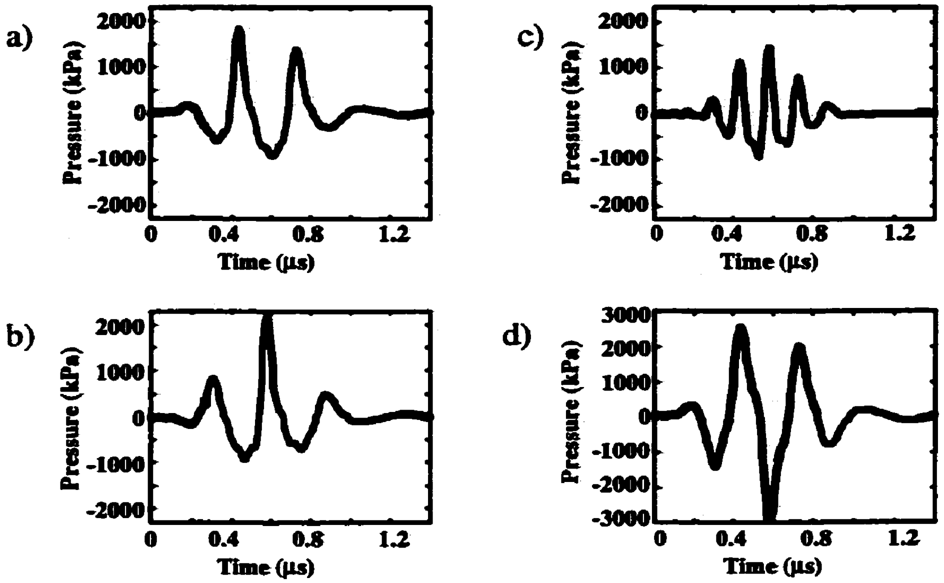

Figure 56: Pressure waveforms for focussed sound pulses transmitted 88 mm through water: a) normal pulse; b) inverted pulse; c) adding the signals together isolates the asymmetric signal components; d) subtracting the signals isolates the symmetric components

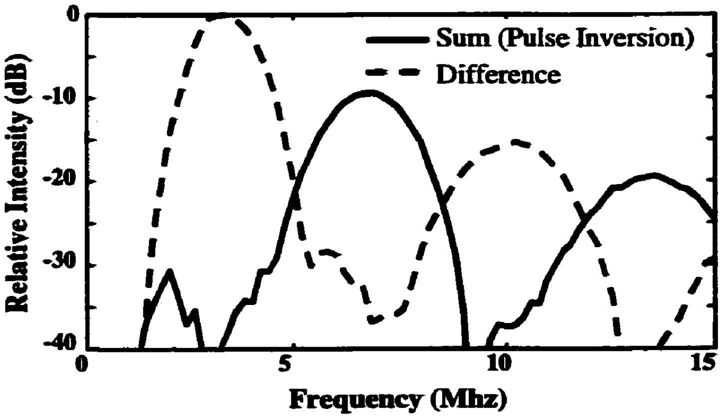

Figure 57: Spectra of pulse inversion sum and difference signals from Figure 56. The sum signal contains the even harmonic components and the difference signal contains the odd harmonic components.

The use of pulse inversion imaging to detect tissue harmonic echoes was first suggested in 1997 (Hope Simpson and Burns 1997). At least two ultrasound system manufacturers, (Siemens Ultrasound, Issaquah,WA and ATL Ultrasound, Bothell, WA) now offer pulse inversion tissue harmonic imaging modes as standard imaging options (Jiang et al. 1998). Conventional, harmonic and pulse inversion harmonic images of a dog heart made with the ATL HDI-5000 system are shown in Figure 58. In the conventional image (Figure 58a), haze from imaging artifacts is visible in the ventricles and partially obscures the endocardial borders. Harmonic imaging (Figure 58b) reduces this haze and provides improved visualization of the endocardial borders. Pulse inversion imaging (Figure 58c) provides further improvements in image quality over harmonic imaging, but at a reduced frame rate.

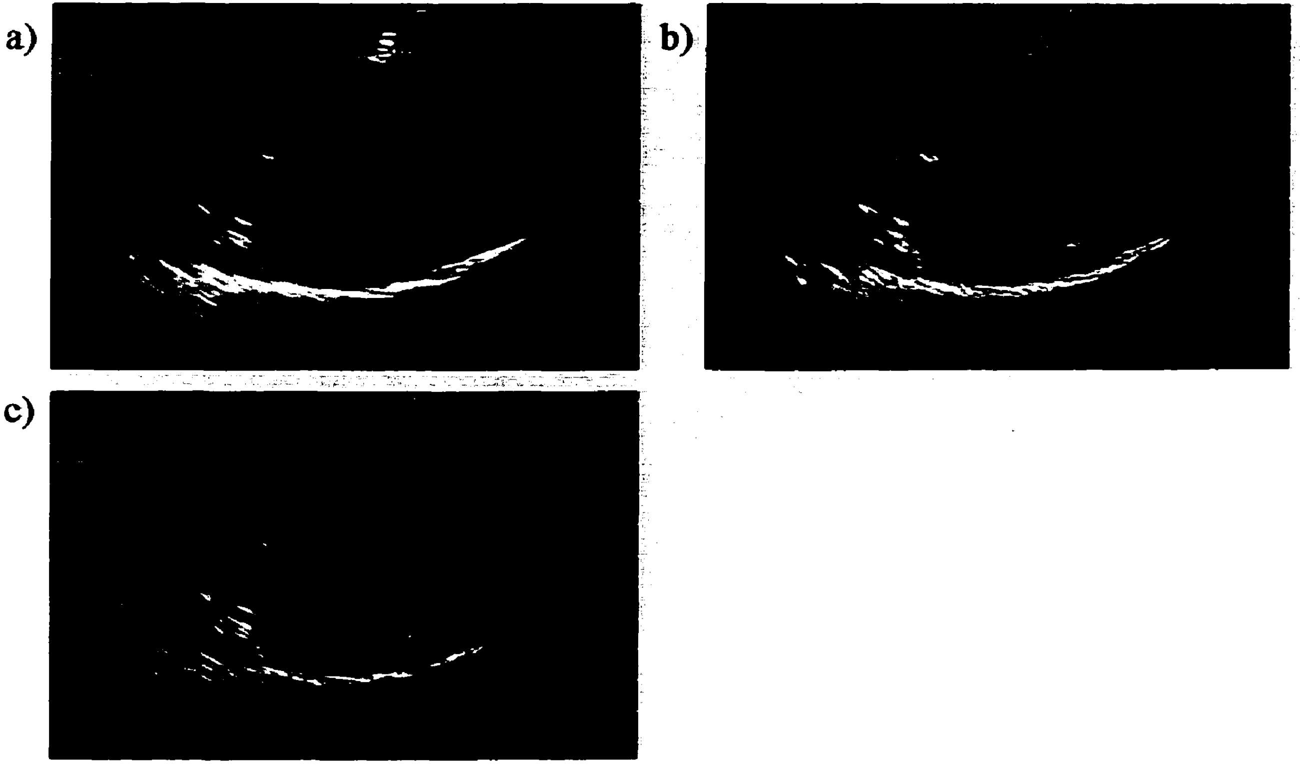

Figure 58: Right parasternal long axis images of a dog heart made with a)Fundamental imaging; b) harmonic imaging; and c) pulse inversion harmonic imaging.

5.4.3.1 Filters For Tissue Harmonic Imaging

The principles used to develop radio frequency and Doppler filters for contrast imaging (see Chapter 3) are equally applicable to other imaging tasks, including tissue imaging. With baseline pulse inversion Doppler image data taken from the experiments described in Chapter 3, we have designed RF and Doppler filters to detect echoes arising from the septal myocardium and to reject (artifactual) echoes detected from within the left ventricle. Figure 59a shows a conventional greyscale image of the heart formed by transmitting and receiving echoes at the fundamental frequency (1.67 MHz), without the use of a Doppler filter. Only the first four echoes from each line of sight have been processed. Artifacts are present within the left ventricle, and the right ventricle is almost entirely obscured by haze. Figure 59b shows the same data processed using filters designed with the automated techniques described in Chapter 3. Artifacts appear reduced in the left ventricle, and much of the right ventricle is now visible. In this case, the filter design techniques automatically selected for the second harmonic, nonlinear components of the echoes (Figure 59c and d). Such experiments provide further evidence that artifacts in cardiac imaging arise primarily from the linear sound beam.

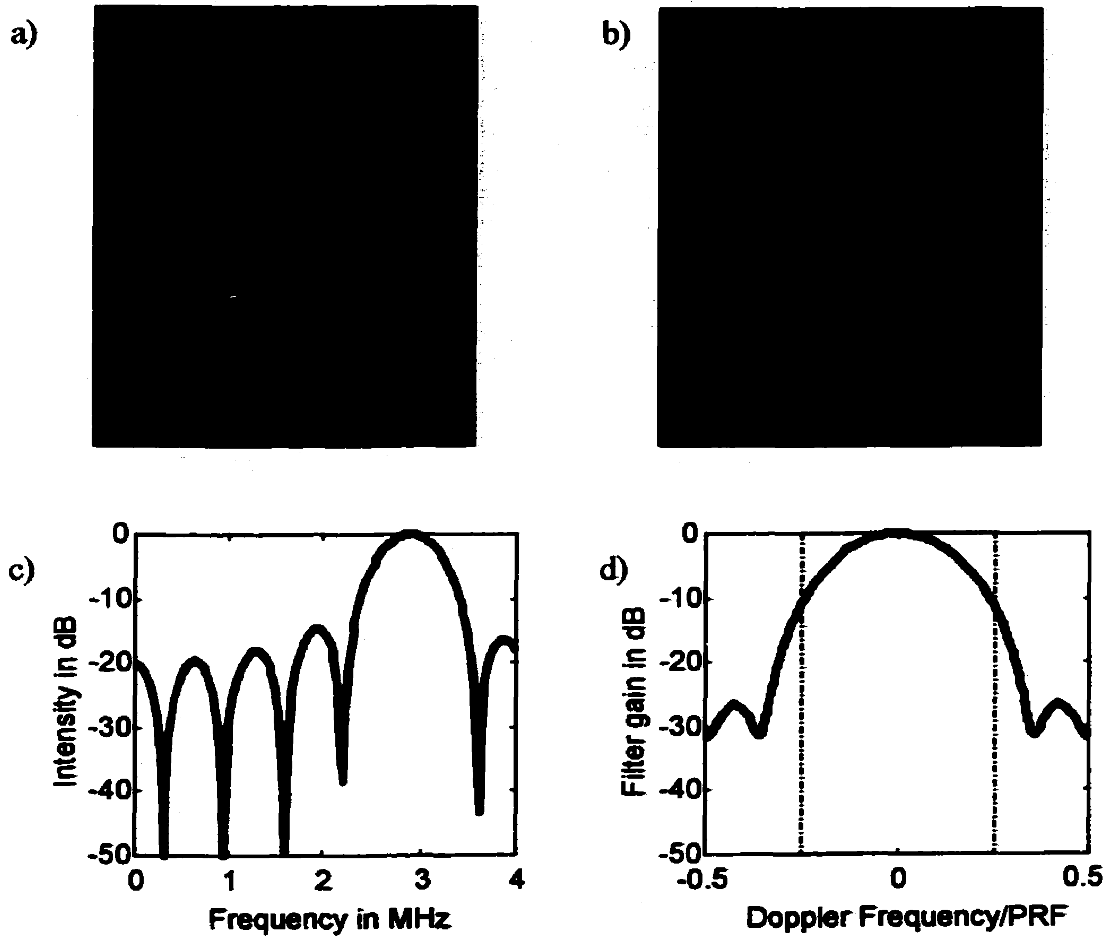

Figure 59: Right parasternal short axis images of a dog heart made with a) fundamental greyscale imaging; and b) optimized 4-pulse pulse inversion imaging. Filters designed to suppress echoes from within the left ventricle automatically select for the second harmonic, nonlinear component of the echoes.

5.5 Discussion

These three applications demonstrate the vast potential of nonlinear contrast and tissue imaging techniques. Pulse inversion Doppler and its two-pulse variant, pulse inversion imaging, have evolved from earlier Doppler and harmonic imaging techniques, and appear to offer significant benefits in many areas. By removing the resolution/contrast tradeoffs of harmonic imaging, pulse inversion techniques have provided the capability to image microbubbles in realtime without destroying them.

The somewhat serendipitous discovery of tissue harmonic imaging has had a profound impact in cardiology, where harmonic imaging is now used as the standard cardiac imaging technique in many centres. Whereas contrast media will likely be used in only a portion of ultrasound examinations, harmonic imaging offers potential benefits for all ultrasound examinations. The incremental benefits provided by pulse inversion imaging over tissue harmonic imaging may thus prove even more significant than the contrast applications for which this technique was originally developed. The only approved cardiac indication for contrast imaging at the moment is for left ventricular opacification – i.e. to make the ventricles more visible with ultrasound. Ironically, harmonic imaging, which was first developed to detect contrast microbubbles, may actually help to make the use of microbubbles for this application obsolete (Kasprzak et al. 1999; Main et al. 1999).

6 Significance and Future Work

Figures 61a-d have been submitted for publication as Figures 5a,b, and 8a,b in Hope Simpson, D. and Burns, P. N. Segmentation of Microbubble and Tissue Echoes in Pulse Inversion Doppler Imaging. Ultrasoound in Medicine and Biology (manuscript UMB/2000/52). They are used with permission.

6.1 Significance

The applications described in the previous chapter demonstrate the potential of pulse inversion techniques. These techniques are now in the hands of clinical researchers. Their utility appears well established, and the feasibility of realtime perfusion imaging has been demonstrated. Pulse inversion imaging, where available, has largely superceded harmonic imaging as the preferred greyscale technique for microbubble detection in radiological applications. Intermittent power Doppler imaging, however, still remains the most sensitive method for detecting microbubbles in tissue and is the most common technique for myocardial perfusion imaging (Becher et al. 2000). Power Doppler imaging has the additional advantage that it works well with all microbubble contrast agents, not just with perfluorocarbon agents. Because they can provide complementary information, both realtime pulse inversion Doppler and intermittent power Doppler will both likely play an important role in clinical practice.

6.1.1 Context of the Present Work

As is common with many scientific advances, some of the concepts presented in this work have been developed in parallel by others. The original concept of pulse inversion imaging, described in Chapter 2, was also developed by Juin Jet Hwang at ATL Ultrasound Inc. (Bothell, WA) (Hwang and Hope Simpson 1998). Chapman and Lazenby also described similar concepts at roughly the same time (Chapman and Lazenby 1997). The first *in vivo* pulse inversion images were presented in 1996 by Lee et al. (Lee et al. 1997), who used prototype software running on a Sonoline Elegra imaging system (High Resolution Harmonic Imaging, Siemens, Issaquah, WA).

The present formulation of pulse inversion as a Doppler-based technique (Chapter 2) arose from an analysis of the error induced by tissue motion in the original 2-pulse technique. The theory of pulse inversion Doppler and corresponding *in vitro* data were originally presented at the IEEE Ultrasonics Symposium in Toronto in 1997, and at the same time the use of pulse inversion for tissue imaging was suggested (Hope Simpson and Burns 1997). Further work with pulse inversion imaging (2-pulse and multi-pulse), was conducted in partnership with ATL Ultrasound, who developed all of the experimental software and imaging systems used in this work as part of a larger contrast imaging program. Many significant scientific and engineering challenges required to make pulse inversion function in a clinical setting were overcome by the ATL research and development team. As a result of these collaborations, the first pulse inversion images of myocardial perfusion were presented in January 1998 and the possiblity of using of low sound intensities to reduce disruption effects was first suggested (Hope Simpson and Burns 1998b --). The first pulse inversion Doppler images of myocardial perfusion were presented later that year (Hope Simpson and Burns 1998a). While we predicted the possibility of real time perfusion imaging, the clinical success of this technique was due largely to the work of researchers at ATL.

6.2 Future Work

6.2.1 The Future of Contrast Imaging

Despite the success of research in microbubble perfusion imaging, the approved indications for contrast agents are currently restricted to left ventricular opacification (to enhance visibility of the endocardial border) and Doppler enhancement. No contrast agent has yet been approved for perfusion imaging, although several are now undergoing clinical trials for this application. The slow acceptance of microbubble contrast imaging has been due to several factors. The traditional strengths of ultrasonic imaging have included its noninvasive nature, and low cost. Since -- The use of contrast media make an ultrasound exam more invasive and adds cost (each vial of agent is currently over $100 U.S.—a significant fraction of the cost of some examinations). To justify the additional costs and invasiveness, contrast media must provide tangible diagnostic benefits with routine use (Kremkau et al. 1998; Leopold 1998; Cosgrove 1996). The large clinical trials required to obtain regulatory approval for specific diagnostic indications are expensive and time consuming, so significant indications such as myocardial perfusion imaging are needed to support these trials. Unfortunately, existing perfusion imaging techniques are difficult to perform. Most clinical studies of myocardial perfusion imaging performed to date have used intravenous bolus injections of microbubbles. Such injections provide peak signal enhancement within about 20 seconds of injection, followed by a rapid fall-off in enhancement over the next 2 to 4 minutes (Figure 60). During this brief period, all imaging parameters including gain, power levels, frame intervals and Doppler settings must be adjusted correctly, and diagnostic images acquired. Failure to set any single parameter correctly may render the exam ineffective, wasting both agent and time.

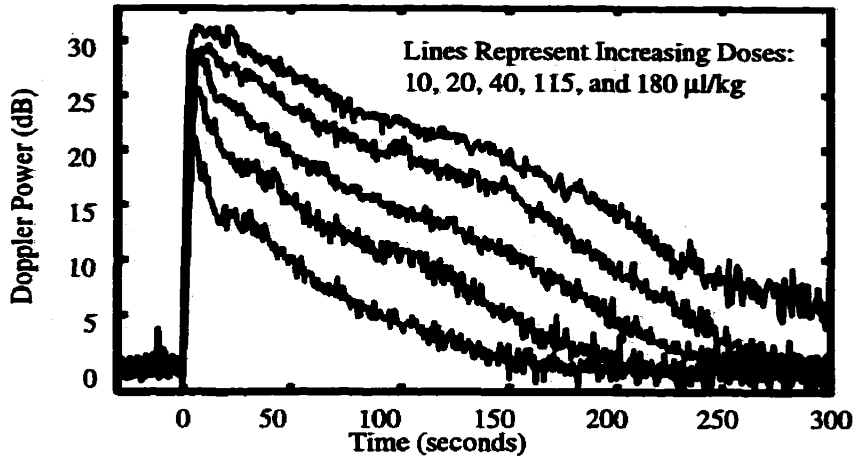

Figure 60: Doppler enhancement versus time in a 3.5 kg new Zealand White rabbit for bolus injections of Optison (Mallinckrodt medical, St. Louis), for increasing doses of 10, 20, 40, 115, and 180 µl/kg (Hope Simpson et al. 1996). Typical human doses are below 40 µl/kg. Bolus duration is short-lived and enhancement changes continuously.

For ultrasonic perfusion imaging to become accepted clinically, four things are required: infusable contrast agents, robust imaging techniques, established imaging protocols, and proper education in their use for clinicians (Kremkau et al. 1998). Together with these requirements, clinical trials must be performed to demonstrate the effectiveness of imaging techniques. Basic research is also required to understand the acoustic behaviour of microbubbles and to understand the relationships between ultrasonic perfusion measurements, microvascular blood flow, and disease states.

Work is progressing steadily in all of these areas. Infusion protocols, using either infusion pumps or intravenous drips, are now available or under investigation for many contrast agents (Correas et al. 2000). Machine and agent-specific protocols for myocardial perfusion imaging are being developed for dissemination to clinicians (Becher and Burns 2000). Extensive clinical research is being conducted at many centres to investigate the benefits of contrast imaging techniques (Cohen et al. 1998). Sophisticated optical imaging systems are being used to measure microbubble pulsations and compare these with mathematical models (Dayton et al. 1999a; Klibanov et al. 1998). At the same time, physiological phenomena, such as the mechanisms underlying phenomena such as the late phase of liver enhancement, are being investigated (Kono et al. 2000).

6.2.2 Future Developments of Pulse Inversion Techniques

Pulse inversion imaging is still in its infancy, and more work is required to refine this technique to its full potential. For example, the current implementations of realtime pulse inversion Doppler use a simple power threshold on the nonlinear signal to determine whether or not microbubbles are present in a given sample volume. The essential feature that differentiates microbubbles from tissue is not the absolute intensity of nonlinear scattering, but the ratio of nonlinear to linear scattering (see Chapter 2). We are currently investigating thresholding techniques that use a combination of the nonlinear signal power and the ratio of nonlinear to linear scattering to identify microbubble echoes. Preliminary results show that such thresholding can significantly reduce artifacts in realtime power pulse inversion imaging (Figure 61).

It is now clear that the acoustic properties of microbubble contrast agents depend on the nature of the shell and filling gases used. All contrast imaging techniques must therefore be optimized for each combination of agent and acoustic conditions, possibly using the techniques outlined in Chapter 3. Some instrument manufacturers are already developing such agent-specific settings, but more work is required before all manufacturers can provide techniques that work robustly with all available agents.

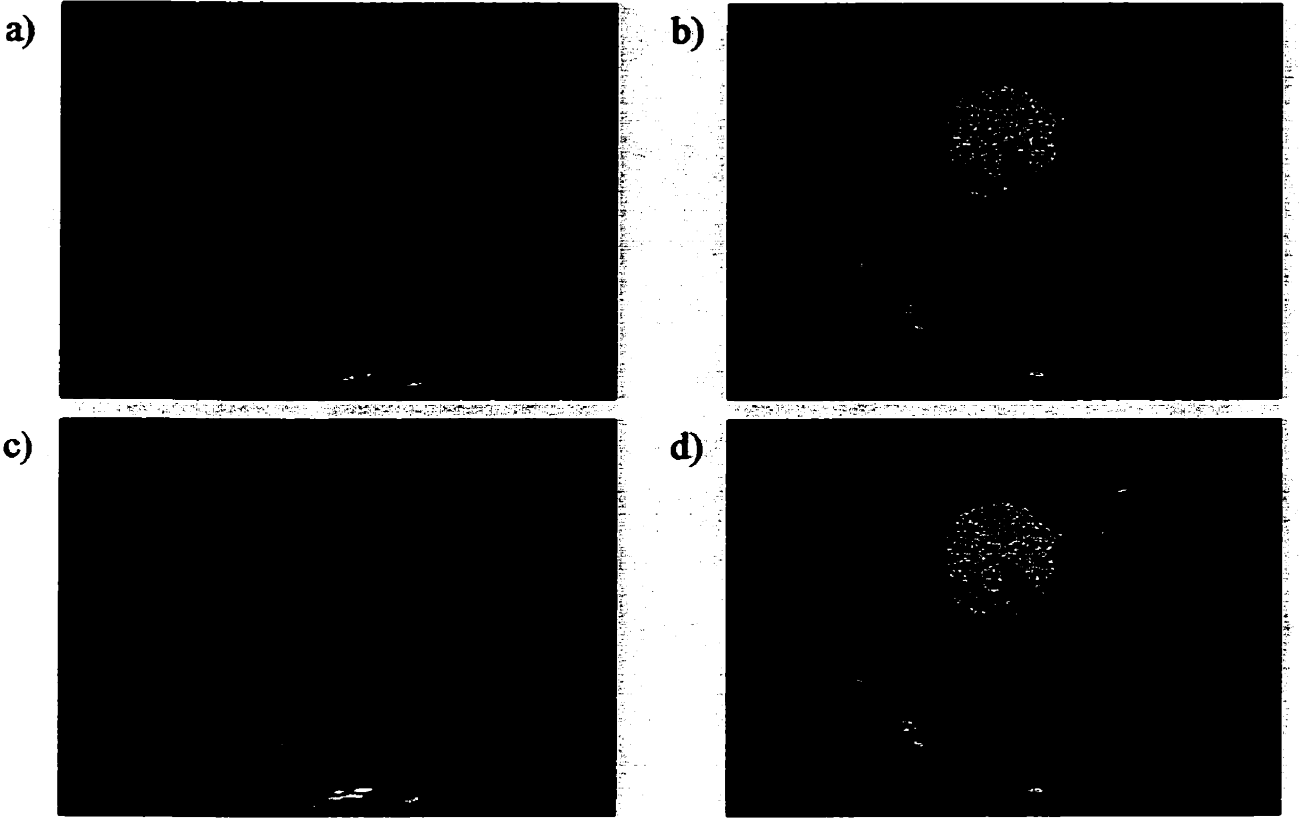

Figure 61: Apical 4 chamber views of the heart made with 4-pulse pulse inversion Doppler imaging (MI=0.1) using a conventional power threshold to identify microbubbles: a) baseline; b) following a bolus injection of Definity (18 μl/kg). These same data were reprocessed using an experimental thresholding technique, showing similar contrast enhancement with reduced Doppler artifacts in the baseline image (Figures c and d) (Hope Simpson and Burns 2000).

6.2.3 Other Approaches to Contrast Imaging

Several other microbubble imaging techniques, currently in the research stages, deserve mention. Subharmonic imaging is a technique which exploits the sound scattered from microbubbles not at twice the transmit frequency (as in harmonic imaging), but at half the transmit frequency (Shi et al. 1999a). Since nonlinear propagation does not produce subharmonics, this technique should be less affected by tissue scattering than harmonic imaging. The low frequency subharmonic echoes should also be less affected by attenuation. Early results, however, suggest that narrowband transmit bursts and intermediate to high power levels (and consequent microbubble disruption) are required to generate significant levels of subharmonics from microbubbles (Shi et al. 1999b). These conditions create resolution and frame rate limitations which must be overcome if subharmonic imaging is to provide high resolution, realtime contrast imaging. Unless this technique can operate effectively without microbubble disruption, it is also unclear whether it will outperform power Doppler imaging in terms of contrast and resolution.

Several variants of the pulse inversion detection concept have been suggested. In Power Modulation Imaging, two pulses are transmitted at different power levels (Brock-Fisher et al. 1996; Christopher 1997). The corresponding echoes are then scaled and subtracted to cancel stationary linear echoes. Remaining signals are due to nonlinear scattering. While this technique has relatively poor signal to noise characteristics for second harmonic detection when compared to pulse inversion (Jiang et al. 1998), it can detect third order nonlinear components at the transmit frequency, which may have benefits (Brock-Fisher et al. 2000). We have also described a generalized pulse inversion Doppler system in which the phase and amplitude of a sequence of transmitted pulses are both modulated (Burns and Hope Simpson 1998). Techniques have recently been described to optimize this generalized form of pulse inversion Doppler to detect higher harmonics of nonlinear signals (Haider and Chiao 1999). These higher harmonics may offer incremental benefits for tissue and contrast harmonic imaging.

A variant of power Doppler imaging called "release burst imaging" has been introduced to image disrupting microbubbles (Frinking et al. 1997). In this method, a sequence of high resolution imaging pulses is combined with a separate low frequency sound pulse, specially designed to disrupt microbubbles efficiently. By separating the pulses used for imaging from those used for disruption, both processes may be optimized independently. Preliminary results show that this technique may provide greater sensitivity to microbubbles than existing power

Doppler methods (Kirkhorn et al. 2000). Chapter 3 may prove useful in optimizing such techniques.

6.2.4 Novel Applications of Microbubble Contrast Agents

The potential applications for existing microbubble contrast agents range from measuring perfusion in the brain to detecting obstructions in fallopian tubes (Balen et al. 1993; Greenberg et al. 1996). Novel targeted contrast agents are also being developed, including agents that adhere to thrombus, increasing its visibility (Unger et al. 2000). In addition to radiological applications, microbubbles are increasingly being developed for therapeutic applications. Several researchers have demonstrated the ability to attach drugs and even DNA to microbubbles (Unger et al. 1997). High intensity ultrasound can then be used selectively to disrupt microbubbles in tissues, offering a method for targeted drug delivery or ultrasound-enhanced gene transfection (Greenleaf et al. 1997). Blood clots can be lysed using a combination of high intensity ultrasound and thrombus-targeted microbubbles (Birnbaum et al. 1998; Wu et al. 1998b). Angiogenesis has long been known to be crucial to the development of solid tumours, and anti-angiogenic drugs are now being developed to treat these tumours (Folkman 1995; O'Reilly et al. 1997; O'Reilly et al. 1994). Ultrasound contrast techniques should be ideal for monitoring the effects of anti-angiogenic drug therapy, and even for delivering anti-angiogenic drugs and genes. In the heart, it may one day be possible to identify regions of ischemic myocardium with contrast imaging, use ultrasound activated microbubbles to deliver angiogenesis-promoting genes to these regions, and then use contrast imaging to monitor the results of gene therapy.

6.3 Summary of This Thesis

This thesis has addressed the problem of detecting blood flow in the coronary microcirculation using ultrasound and microbubble contrast agents.

Prior to this work, existing harmonic and Doppler imaging techniques suffered from compromises between spatial and temporal resolution and image contrast, which limited the detection of myocardial blood flow to frame rates below 1 frame per 3 to 5 heartbeats. To overcome these limitations and enable real time imaging of myocardial blood flow, this thesis has reexamined both the transmission and detection of ultrasound for microbubble imaging. A new ultrasound technique, pulse inversion Doppler, has been introduced in which successive transmitted pulses are inverted to provide improved separation of microbubble and tissue echoes (Chapter 2). Chapter 3 provides an analysis of the detection process, and shows how the measured echoes from agent and tissue can be used, without explicit models of the transmission and scattering processes, to optimize filters for myocardial perfusion imaging. This analysis is applicable to a wide variety of imaging techniques including harmonic, Doppler and pulse inversion techniques.

Using the techniques of Chapter 3, the effectiveness of grayscale, harmonic, Doppler and pulse inversion Doppler imaging techniques for detecting myocardial perfusion in canine myocardium have been assessed under controlled conditions as a function of incident sound intensity (Chapter 4). These results show that pulse inversion Doppler at low transmit intensities outperforms harmonic and Doppler techniques and can detect myocardial perfusion in real time at rates exceeding 15 frames per second.

Pulse inversion Doppler techniques are now available for use on clinical ultrasound systems. For cardiological applications, pulse inversion Doppler is now the recommended technique for simultaneously assessing myocardial blood flow and wall motion (Becher and Burns 2000). Pulse inversion imaging is also the preferred technique for contrast imaging in the liver. Pulse inversion imaging is also used without microbubbles to provide improved imaging of tissue and cystic structures.

7 References:

Anderson, A. L., and Hampton, L. D. Acoustics of Gas-Bearing Sediments I. Background. J Acoust Soc Am 1980; 67(6):1865-1889.

Apfel, R. E. Sonic Effervescence: A Tutorial on Acoustic Cavitation. J Acoust Soc Am 1997; 101(3):1227-1237.

Apfel, R. E., and Holland, C. K. Gauging the Likelihood of Cavitation From Short-Pulse, Low-Duty Cycle Diagnostic Ultrasound. Ultrasound Med Biol 1991; 17(2):175-185.

Armstrong, W. F., Mueller, T. M., Kinney, E. L., Tickner, E. G., Dillon, J. C., et al. Assessment of Myocardial Perfusion Abnormalities with Contrast-Enhanced Two-Dimensional Echocardiography. Circulation 1982; 66(1):166-173.

Averkiou, M. A., and Hamilton, M. F. Measurements of harmonic generation in a focussed finite-amplitude sound beam. J Acoust Soc Am 1995; 98(6):3439-3442.

Averkiou, M. A., and Hamilton, M. F. Nonlinear Distortion of Short Pulses Radiated by Plane and Focused Circular Pistons. J Acoust Soc Am 1997; 98(6):3439-3442.

Averkiou, M. A., Roundhill, D. N., and Powers, J. E. A New Imaging Technique Based on the Nonlinear Properties of Tissues. Proc IEEE Ultrason Symp 1997; :1561-1566.

Averkiou, M. A., Skyba, D. M., Bruce, M. F., and Powers, J. E. "Real Time Perfusion Imaging with Ultrasound Contrast Agents." *The 5th Heart Centre European Symposium on Ultrasound Contrast Imaging, 2000*, 9-12.

Ayme-Bellegarda, E. J. Collapse and Rebound of a Gas-Filled Spherical Bubble Immersed in a Diagnostic Ultrasonic Field. J Acoust Soc Am 1990; 88(2):1054-1060.

Balen, F. G., Allen, C. M., and Lees, W. R. Ultrasound Contrast Agents. Clin Rad 1994; 49(´):77-82.

Balen, F. G., Allen, C. M., Siddle, N. C., and Lees, W. R. Ultrasound contrast hysterosalpingography -- evaluation as an outpatient procedure. Brit J Radiol 1993; 66:592-599.

Barnett, S. B. WFUMB Symposium on Safety of Ultrasound in Medicine: Conclusions and Recommendations for Biological Effects of Ultrasound. Ultrasound Med Biol 1998; 24(Supplement 1):S1-S55.

Bax, J. J., Poldermans, D., Elhendy, A., Cornel, J. H., Boersma, E., et al. Improvement of Left Ventricular Ejection Fraction, Heart Failure Symptoms and Prognosis After Revascularization in Patients with Chronic Coronary Artery Disease and Viable

Myocardium Detected by Dobutamine Stress Echocardiography. J Am Coll Cardiol 1999; 34(1):163-169.

Becher, H., and Burns, P. N. A Handbook Of Contrast Echocardiography. Heidelberg: Springer, 2000.

Becher, H., Kuntz, S., and Tiemann, K. "Clinical Value of Myocardial Perfusion Imaging Using Power Doppler." *The 5th Heart Centre European Symposium on Ultrasound Contrast Imaging, 2000,* 4.

Birnbaum, Y., Luo, H., Nagai, T., Fushbein, M. C., Peterson, T. M., et al. Noninvasive in Vivo Clot Dissolution Without a Thrombolytic Drug. Circulation 1998; 97:130-134.

Bjaerum, S., and Torp, H. Optimal Adaptive Clutter Filtering in Colour Flow Imaging. Proc IEEE Ultrason Symp 1997; :1223-1226.

Blomley, M. J., Albrecht, T., Cosgrove, D. O., Patel, M., Jayaram, V., et al. Improved Imaging of Liver Metastases with Stimulated Acoustic Emission in the Late Phase of Enhancement with the US Contrast Agent SHU508A: Early Experience. Radiology 1999a; 210(2):409-416.

Blomley, M. J. K., Albrecht, T., Cosgrove, D. O., Eckersley, R. J., Butler-Barnes, J., et al. Stimulated Acoustic Emission to image Late Liver and Spleen-Specific Phase of Levovist in Normal Volunteers and Patients With and Without Liver Disease. Ultrasound Med Biol 1999b; 25(9):1341-1352.

Boukaz, A., and De Jong, N. In Vitro Standard Acoustic Parameters of Ultrasound Contrast Agents: Definitions and Calculations. Proc IEEE Ultrasonics Symp 1996; :1445-1448.

Brennan, C. E. Cavitation and Bubble Dynamics. New York: Oxford University Press, 1995.

Brock-Fisher, G. A., Poland, M. D., and Rafter, P. G. Means for Increasing Sensitivity in Non-Linear Ultrasound imaging Systems., US Patent # 5,577,505, 1996.

Brock-Fisher, G. A., Poland, M. D., Rafter, P. G., and Mooney, M. G. Experimental Observations of the Sensitivity and Frequency Response of the Power Modulation Technique for Contrast Imaging. The 5th Heart Centre European Symposium on Ultrasound Contrast Imaging,2000 2000; .

Burns, P. N. Harmonic Imaging with Ultrasound Contrast Agents. Clin Rad 1996; 51(Supplement 1):50-55.

Burns, P. N., Halliwell, M., and Wells, P. N. T. Ultrasonic Doppler Studies of the Breast. Ultrason Med Biol 1982; 8(2):127-143.

Burns, P. N., and Hope Simpson, D. Pulse Inversion Doppler Ultrasound Diagnostic Imaging., US Patent Application 09/156,097 (pending), 1998.

Burns, P. N., Hope Simpson, D., and Averkiou, M. A. Nonlinear Imaging. Ultrasound Med Biol 2000a; 26(1001):S19-S22.

Burns, P. N., Hope Simpson, D., Chin, C. T., and Powers, J. The Origin of Transient Echoes from Ultrasound Contrast Agents. presented at the IEEE Ultrasonics Symposium, Toronto 1997; .

Burns, P. N., Hope Simpson, D., Qi, X., and Purcell, C. The Effect of Bubble Depletion on Destruction-Reperfusion Flow Measurement with Contrast. The 5th Heart Centre European Symposium on Ultrasound Contrast Imaging, 2000 2000b; :8-8A.

Burns, P. N., Powers, J. E., and Fritzsch, T. Harmonic Imaging: New Imaging and Doppler Method for Contrast Enhanced US. Radiology 1992; 185(P):142.

Burns, P. N., Powers, J. E., Hope Simpson, D., Brezina, A., Chin, C. T., et al. "Harmonic Power Mode Doppler Using Microbubble Contrast Agents: An Improved Method for Small Vessel Flow Imaging." *Proceedings of the IEEE Ultrasonics Symposium*, 1547-1550.

Burns, P. N., Powers, J. E., Hope Simpson, D., Uhlendorf, V., and Fritzsch, T. Harmonic Imaging: Principles and Preliminary Results. Angiology 1996; 47(7):S63-S74.

Burns, P. N., Wilson, S. R., and Hope Simpson, D. Pulse Inversion Imaging of Liver Blood Flow: Improved Method for Characterizing Focal Masses with Microbubble Contrast. Invest Radiol 2000c; 35(1):58-71.

Chapman, C. S., and Lazenby, J. C. Ultrasound Imaging System Employing Phase Inversion Subtraction to Enhance the Image., US Patent # 5632277, 1997.

Child, S. Z., Hartman, C. L., Schery, L. A., and Carstensen, E. L. Lung Damage from Exposure to Pulsed Ultrasound. Ultrasound Med Biol 1990; 16(8):817-825.

Chin, C. T., and Burns, P. N. "Predicting the Acoustic Response of a Microbubble Population for Contrast Imaging." *Proc. IEEE Ultrason. Symp.*, 1557-1560.

Christopher, T. Finite Amplitude Distortion-based Inhomogenous Pulse Echo Ultrasonic Imaging. IEEE Transaction on Ultrasonics, Ferroelectrics, and Frequency Control 1997; 44(1):125-139.

Church, C. C. The Effects of an Elastic Solid Surface Layer on the Radial Pulsations of Gas Bubbles. J Acoust Soc Am 1995; 97(3):1510-1521.

Cohen, J. L., Cheirif, J., Segar, D. S., Gillam, L. D., Gottdiener, J. S., et al. Improved Left Ventricular Endocardial Border Delineation and Opacification with OPTISON (FS069), a New Echocardiographic Contrast Agent: Results of a Phase III Multicenter Trial. J Am Coll Cardiol 1998; 32(3):746-752.

Correas, J.-M. Echogen Emulsion: A New Ultrasound Contrast Agent Based on Phase Shift Colloids. Clin Rad 1996; 51(Supplement 1):11-14.

Correas, J.-M., Burns, P. N., Lai, X., and Qi, X. Infusion Versus Bolus of an Ultrasound Contrast Agent. Invest Radiol 2000; 35(1):72-79.

Cosgrove, D. Ultrasound Contrast Enhancement of Tumours. Clin Rad 1996; 51(Supplement 1):44-49.

Dayton, P., Klibanov, A., Brandenburger, G., and Ferrara, K. Acoustic Radiation Force in Vivo: A Mechanism to assist Targeting of Microbubbles. Ultrasound Med Biol 1999a; 25(8):1195-1201.

Dayton, P. A., Morgan, K. E., Klibanov, A. L., Brandenburger, G. H., and Ferrara, K. W. Optical and Acoustical Observations of the Effects of Ultrasound Contrast Agents. IEEE Transaction on Ultrasonics, Ferroelectrics, and Frequency Control 1999b; 46(1):220-232.

de Jong, N. Physics of Microbubble Scattering. Advances in Echo Imaging Using Contrast Enhancement, N. C. Nanda, R. Schlief, and B. B. Goldberg, eds., Dubai, Kluwer Academic Publishers, 1997:39-64.

de Jong, N., and Hoff, L. Ultrasound Scattering Properties of Albunex Microspheres. Ultrasonics 1993; 31(3):175-181.

De Maria, A., Cotter, B., and Ohmori, K. Myocardial Contrast Echocardiography: Too Much, Too Soon? J Am Coll Cardiol 1998; 32(5):1270-1.

Eatock, B. C., and Johnston, G. W. Numerical Studies of the Spectrum of Low-Intensity Ultrasound Scattered by Bubbles. J Acoust Soc Am 1985; 77(5):1692-1701.

Epstein, P. S., and Plesset, M. S. On the Stability of Gas Bubbles in Liquid-Gas Solutions. J Appl Mech 1949; 16:277.

Everbach, E. C., Makin, I. R. S., Francis, C. W., and Meltzer, R. S. Effect of Acoustic Cavitation on Platelets in the Presence of an Echo-Contrast Agent. Ultrasound Med Biol 1998; 24(1):129-136.

Feinstein, S. B., Cheirif, J., Ten Cate, F. J., Silverman, P. R., Heidenreich, P. A., et al. Safety and Efficacy of a New Transpulmonary Ultrasound Contrast Agent: Initial Multicenter Clinical Results. J Am Coll Cardiol 1990; 16(2):316-324.

Ferrara, K., and DeAngelis, G. Color Flow Mapping. Ultrason Med Biol 1997; 23(3):321-345.

Ferrara, K. W., Zagar, B. G., Sokil-Melgar, J. B., Silverman, R. H., and Askanidis, I. M. Estimation of Blood Velocity with High Frequency Ultrasound. IEEE Trans Ultrason, Ferroelect, Freq Contr 1996; 43(1):149-157.

Firschke, C., Lindner, J. R., Goodman, N. C., Skyba, D. M., Wei, K., et al. Myocardial Contrast Echocardiography in acute Myocardial Infarction Using Aortic Root Injections of Microbubbles in Conjunction With harmonic imaging: Potential Appliaction in the Cardiac Catheterization Laboratory. J Am Coll Cardiol 1997; 29(1):207-216.

Folkman, J. Clinical Applications of Research on Angiogenesis. N Engl J Med 1995; 333(26):1757-1763.

Fowlkes, J. B., and Holland, C. K. Mechanical Bioeffects from Diagnostic Ultrasound: AIUM Consensus Statements. J Ultrasound Med 2000; 19:69-168.

Fowlkes, J. B., Sirkin, D. W., Ivey, J. A., A., G. E., Rhee, R. T., et al. Transcutanous Interruption of Ultrasound Contrast Agents for Blood Flow Evaluation. Invest Radiol 1998; 33(12):893-901.

Fox, S. L Human Physiology. Dubuque, Iowa: Wm. C. Brown Publishers, 1987.

Frinking, P. J. A., Cespedes, I., and deJong, N. Multi-Pulse Ultrasound Contrast imaging Based on a Decorrelation Detection Strategy. Proc IEEE Ultrasonics Symp 1997; :1787-1790.

Frush, D. P., Babcock, D. S., White, K. S., and Barr, L. L. Quantification of Intravenous Contrast-Enhanced Doppler Power Spectrum in the Rabbit Carotid Artery. Ultrasound Med Biol 1995; 21(1):41-47.

Fry, W. J., and Dunn, F. Physical Techniques in Biological Research, chap. 6 Ultrasound: Analysis and Experimental Methods in Biological Research. : Academic Press, 1962.

Garcia, E. V. Imaging Guidelines for Nuclear Cardiology Procedures: Part 1. Journal of Nuclear Cardiology 1996; 3(3):G1-G46.

Girard, M. S., Sirlin, C. B., Baker, K. B., Hall, L. A., and Mattrey, R. F. Liver-Tumor Detection with Ultrasound Contrast: A Blinded Prospective Study in Rabbits. Acad Radiol 1998; 5(Supplement 1):S189-S191.

Gramiak, R., and Shah, P. M. Echocardiography of the Aortic Root. Investigative Radiology 1968; 3:356-366.

Grayburn, P. A., Weiss, J. L., Hack, t. C., Klodas, E., Raichlen, J. S., et al. Phase III Multicenter Trial Comparing eht Efficacy of 2% Dodecafluoropentane Emulsion (Echogen) and Sonicated 5% Human Albumen (Albunex) as Ultrasound Contrast Agents in Patients With Suboptimal Echocardiograms. Joural of the American College of Cardiology 1998; 32(1):230-6.

Greenberg, R. S., Taylor, G. A., Stapleton, J. C., Hillsley, C. A., and Spinak, D. Analysis of Regional Cerebral Blood Flow in Dogs, with an Experimental Microbubble-based US Contrast Agent. Radiology 1996; 201:119-123.

Greenleaf, W. J., Bolander, M. E., Sarkar, G., Goldring, M. B., and Greenleaf, J. F. Enhancement of Ultrasonically Induced Cell Transfection with Artificial Cavitation Nuclei. Proc IEEE Ultrasonics Symp 1997; .

Haider, B., and Chiao, R. Y. Higher Order Nonlinear Ultrasonic Imaging. Proc IEEE Ultrasonics Symp 1999; :in press.

Hamilton, M. F. Sound beams. Nonlinear Acoustics, M. F. Hamilton and D. T. Blackstock, eds., San Diego, Academic Press, 1998:233-261.

Hamilton, M. F., and Blackstock, D. T. Nonlinear Acoustics. , San Diego, Academic Press, 1998.

Hesse, B. Trends in myocardial perfusion single-photon emission technique. Clinical Physiology 1999; 19(3):204-210.

Higgins, C. B. Functional Imaging of the Heart: Role of Magnetic Resonance Imaging Contrast Media. Invest Radiol 1993; Supplement 4:S38-S42.

Holland, C. K., Roy, R. A., Apfel, R. E., and Crum, L. A. In Vitro Detection of Cavitation Induced by a Diagnostic Ultrasound System. IEEE Trans IEEE Transaction on Ultrasonics, Ferroelectrics, and Frequency Control 1992; 29(1):95-101.

Hope Simpson, D., and Burns, P. N. Pulse Inversion Doppler: A New Method for Detecting Nonlinear Echoes from Microbubble Contrast Agents. Proc IEEE Ultrasonics Symp 1997:1597-1600.

Hope Simpson, D., and Burns, P. N. Perfusion Imaging with Pulse Inversion Doppler and Microbubble Contrast Agents: In Vivo Studies of the Myocardium. Proc IEEE Ultrasonics Symp 1998a:1783-1786.

Hope Simpson, D., and Burns, P. N. Pulse Inversion Doppler: a New Nonlinear Imaging Method for Microbubble Contrast Agents. Third Thoraxcenter European Symposium on Ultrasound Contrast Imaging 1998b:(Abstract and Poster).

Hope Simpson, D., and Burns, P. N. Segmentation of Microbubble and Tissue Echoes in Pulse Inversion Doppler Imaging. Ultrasound Med Biol 2000; :(submitted).

Hope Simpson, D., Burns, P. N., and Averkiou, M. A. Myocardial Perfusion Imaging with Pulse Inversion Doppler and Microbubble Contrast Agents. Ultrasound Med Biol 2000; :(submitted).

Hope Simpson, D., Chin, C. T., and Burns, P. N. Pulse Inversion Doppler: A New Method for Detecting Nonlinear Echoes from Microbubble Contrast Agents. IEEE Trans Ultrasonics Ferroelectrics Freq Control 1999; 49(2):372-382.

Hope Simpson, D., Lalond, J., Wilson, S. R., and Burns, P. N. "Dose-Response and Nonlinear Imaging with the Agent FS069." *UCSD Ultrasound Contrast Research Symposium, 1996*, San Diego, CA.

Hwang, J. J., and Hope Simpson, D. Ultrasound Diagnostic Imaging with Harmonic Contrast Agents. , US Patent # 5706819, 1998.

Hwang, J.-J., Quistgaard, J., Souquet, J., and Crum, L. A. Portable Ultrasound Device for Battlefield Trauma. Proc IEEE Ultrasonics Symp 1998; Sendai:1663-1667.

Ito, H., Tomooka, T., Sakai, N., Higashino, Y., Fujii, K., et al. Time Course of Functional Improvement in Stunned Myocardium in Risk Area in Patients With Reperfused Anterior Infarction. Circulation 1993; 87:355-362.

Jensen, J. A. Estimation of Blood Velocities Using Ultrasound: A Signal Processing Approach. Cambridge: Cambridge University Press, 1996.

Jiang, P., Mao, Z., and Lazenby, J. C. A New Tissue Harmonic Imaging Scheme with Better Fundamental Frequency Cancellation and Higher Signal-to-Noise Ratio. Proc IEEE Ultrasonics Symp 1998; :1589-1594.

Kadi, A., and Loupas, T. On the Performance of Regression and Step-Initialized IIR Clutter Filters for Color Doppler Systems in Diagnostic Medical Ultrasound. IEEE Transaction on Ultrasonics, Ferroelectrics, and Frequency Control 1995; 42(5):927-937.

Kasprzak, J. D., Paelinck, B., Ten Cate, F. J., Vletter, W. B., de Jong, N., et al. Comparison of Native and Contrast-Enhanced Harmonic Echocardiography for Visualization of left Ventricular Endocardial Border. Am J Cardiol 1999; 83:211-217.

Kassab, G. S., and Fung, Y.-C. B. Topology and Dimensions of Pig Coronary Capillary Network. American Journal of Physiology 1994; :H319-H325.

Kassab, G. S., Lin, D. H., and Fung, Y.-C. B. Morphometry of Pig Coronary Venous System. American Journal of Physiology 1994a; :H2100-2112.

Kassab, G. S., Rider, C. A., Tang, N. J., and Fung, Y.-C. B. Morphometry of Pig Coronary Arterial Trees. American Journal of Physiology 1994b; 265(34):H350-365.

Kaul, S. Myocardial Contrast Echocardiography: 15 Years of Research and Development. Circulation 1997; 96:3745-3760.

Kaul, S., and Jayaweera, A. R. Coronary and Myocardial Blood Volumes: Noninvasive Tools to Assess the Coronary Microcirculation? Circulation 1997; 96:719-724.

Kaul, S., Senior, R., Dittrich, H., Raval, U., Khattar, R., et al. Detection of Coronary Artery Disease with Myocardial Contrast Echocardiography: Comparison with ^{99m}Tc-Sestamibi Single-Photon Emission Computed Tomography. Circulation 1997; 96:785-792.

Kirkhorn, J., Frinking, P. J. A., deJong, N., Torp, H., and Frigstad, S. "Initial Experience with Multi-Pulse Release Imaging." *The 5th Heart Centre European Symposium on Ultrasound Contrast Imaging*, Rotterdam, 53-54.

Klibanov, A. L., Ferrara, k. W., Hughes, M. S., Wible, J. H., Wojdyla, J. K., et al. Direct In-Vivo Microscopic Observation of the Dynamic Effects of Medical Ultrasound on Ultrasound Contrast Microspheres. Invest Radiol 1998; 33(12):863-870.

Kono, Y., Stenbach, G., Peterson, T., Schmidt-Schonbein, G. W., and F., M. R. "The Mechanism of Parenchymal Enhancement of Liver by Microbubble-Based Ultrasound Contrast Agent: An intravital Microscopy Study." *The 5th Heart Centre European Symposium on Ultrasound Contrast Imaging*, Rotterdam.

Kremkau, F. W., Merritt, C. R. B., Carson, P. L., Needleman, L., Nelson, T. R., et al. Future Directions in Diagnostic US. Radiology 1998; 209:305-311.

Lauterborn, W. Numerical Investigation of Nonlinear Oscillation of Gas Bubbles in Liquids. J Acoust Soc Am 1976; 59(2):283-293.

Law, W. K., Frizzell, L. A., and Dunn, F. Determination of the Nonlinearity Parameter B/A of Biological Media. Ultrasound Med Biol 1985; 11(2):307-318.

Lee, Y. Z., Sirlin, C. B., Steinbach, G. C., and Mattrey, R. F. High Resolution Harmonic Imaging (HRH) versus Duplex Sonography for the Evaluation of Carotid Artery Stenosis. Radiology 1997; 205(P):419.

Leighton, T. G. The Acoustic Bubble. London: Harcourt Brace and Company, 1994.

Leopold, G. R. Commentary on Future Directions in Diagnostic US. Radiology 1998; 209:312-313.

Lerman, L. O., Siripornpitak, S., Maffei, N. L., Sheedy, P. F. I., and Ritman, E. L. Measurement of In Vivo Myocardial Microcirculatory Function with Electron Beam CT. J Computer Assisted Tomography 1999; 23(3):390-398.

Linka, A. Z., Ates, G., Wei, K., Firoozan, S., Skyba, D. M., et al. Three-Dimensional Myocardial Contrast Echocardiography: Validation of In Viov Risk and Infarct Volumes. J Am Coll Cardiol 1997; 30:1892-9.

Loupas, T., Powers, J. T., and Gill, R. W. An Axial Velocity Estimator for Ultrasound Blood Flow Imaging, Based on a Full Evaluation of the Doppler Equation by Means of a Two-Dimensional Autocorrelation Approach. IEEE Transaction on Ultrasonics, Ferroelectrics, and Frequency Control 1995; 42(4):672-688.

Maddahi, J., Kiat, H., and Barman, D. B. Myocardial Perfusion Imaging with Technetium-99m--Labelled Agents. Am J Cardiol 1991; 67:27D-34D.

Main, M. L., Asher, C. R., Rubin, D. N., Odabashian, J. A., Cardon, L. A., et al. Comparison of Tissue Harmonic Imaging With Contrast (Sonicated Albumin) Echocardiography and Doppler Myocardial Imaging for Enhancement of Endocardial Border Resolution. Am J Cardiol 1999; 83:218-222.

Main, M. L., and Garyburn, P. A. Clnical Applications of Transpulmonary Contrast Echocardiography. Am Heart J 1999; 137:144-153.

Marchand, B., Douek, P. C., Benderbous, S., Corot, C., and Canet, E. Pilot MR Evaluation of Pharmacokinetics and Relaxivity of Specific Blood Pool Agents for MR Angiography. Invest Radiol 2000; 35(1):41-49.

Marwick, T. H., Brunken, R., Meland, N., Brochet, E., Baer, F. M., et al. Accuracy and Feasibility of Contrast Echocardiography for Detection of Perfusion Defects in Routine Practice: Comparison with Wall Motion and Technetium-99m Sestamibi Single-Photon Emission Computed Tomography. J Am Coll Cardiol 1998; 32:1260-9.

Mattrey, R. F., Steinbach, G., Lee, Y., Wilkening, W., and Lazenby, J. High-Resolution Harmonic Gray-Scale Imaging of Normal and Abnormal Vessels and Tissues in Animals. Acad Radiol 1998; 5(suppl 1):S63-S65.

Medwin, H. Counting Bubbles Acoustically: A Review. Ultrasonics 1977; (January):7-13.

Miller, D. L. Ultrasonic Detection of Resonant Cavitation Bubbles in a Flow Tube by Their Second Harmonic Emissions. Ultrasonics 1981; :217-224.

Miller, D. L., Gies, R. A., and Chrisler, W. B. Ultrasonically Induced Hemolysis at High Cell and Gas Body Concentrations in a Thin-Disk Exposure Chamber. Ultrasound Med Biol 1997; 23(4):625-633.

Miller, D. L., and Thomas, R. M. Ultrasound Contrast Agents Nucleate inertial Cavitation in Vitro. Ultrason Med Biol 1995; 21(8):1059-1065.

Miller, D. L., Thomas, R. M., and Williams, A. R. Mechanisms for Hemolysis By Ultrasonic Cavitation in the Rotating Exposure System. Ultrasound Med Biol 1991; 17(2):171-178.

Miller, M. W., Miller, D. L., and Brayman, A. A Review of in Vitro Bioeffects of Inertial Ultrasonic Cavitation From a Mechanistic Perspective. Ultrasound Med Biol 1996; 22(9):1131-1154.

Morgan, K. E., Dayton, P. A., Kruse, D. E., Klibanov, A. L., Brandenburger, G. H., et al. Effect of Imaging Parameters on the Echoes from Ultrasonic Contrast Agents. Proc IEEE Ultrasonics Symp 1997; :1593-1997.

Morgan, K. E., Dayton, P. A., Kruse, D. E., Klibanov, A. L., and Ferrara, K. W. Changes in the Echoes From Ultrasonic Contrast Agents With Imaging Parameters. IEEE Transaction on Ultrasonics, Ferroelectrics, and Frequency Control 1998; 45(6):1537-1548.

Morse, P. M., and Ingard, K. U. Theoretical Acoustics. Princeton: Princeton University Press, 1968.

Nagueh, S. F., Vaduganathan, P., Ali, N., Blaustein, A., Verani, M. S., et al. Identification of Hibernating Myocardium: Comparative Accuracy of Myocardial Contrast Echocardiography, Rest-Redistribution Thallium-201 Tomography and Dobutamine Echocardiography. J Am Coll Cardiol 1997; 29(5):985-993.

Nichols, W. W., and O'Rourke, M. F. MacDonald's Blood Flow in Arteries: Theoretical, Experimental and Clinical Principles. New York: Oxford University Press, Inc., 1998.

Omoto, R., and Kasai, C. Physics and Instrumentation of Doppler Flow Mapping. Echocardiography 1987; 4(6):467-483.

Ophir, J., and Parker, K. J. Contrast Agents in Diagnostic Ultrasound. Ultrason Med Biol 1989; 15(4):319-333.

O'Reilly, M. S., Boehm, T., Shing, Y., Fukai, N., Vasios, G., et al. Endostatin: An Endogenous inhibitor of Angiogenesis and Tumour Growth. Cell 1997; 88(January):277-285.

O'Reilly, M. S., Holmgren, L., Shing, Y., Chen, C., Rosenthal, R. A., et al. Angiostatin: A Novel Angiogenesis Inhibitor That Mediates the Suppression of Metastases By a Lewis Lung Carcinoma. Cell 1994; 79(October 21):315-328.

Papoulis, A. Probability, Random Variables, and Stochastic Processes. New York: McGraw-Hill Book Company, 1984.

Plesset, M. S. The Dynamics of Cavitation Bubbles. J Appl Mech 1949; 16:277-282.

Poritsky, H. The Collapse and Growth of a Spherical Bubble or Cavity in a Viscous Fluid. Proceedings of the First US National Congress on Applied Mechanics 1951; :813-821.

Porter, R. The Greatest Benefit to Mankind: A Medical history of Humanity from Antiquity to the Present. London: Harper Collins Publishers, 1997.

Porter, T. R., and Xie, F. Visually Discernable Myocardial Echocardiographic Contrast After Intravenous Injection of Sonicated Dextrose Albumin Microbubbles Containing High Molecular Weight, Less Soluble Gases. J Am Coll Cardiol 1995; 25(2):509-15.

Porter, T. R., Xie, F., Kricsfeld, A., and Kilzer, K. Noninvasive Identifications of Acute Myocardial Ischemia and Reperfusion With Contrast Ultrasound using Intravenous Perfluoropropane-Exposed Sonicated Dextrose Albumin. J Am Coll Cardiol 1995; 26(1):33-40.

Porter, T. R., Xie, F., Kricsfeld, D., and Armbruster, R. W. Improved Myocardial Contrast With Second Harmonic Transient Ultrasound Response Imaging in Humans Using Intravenous Perfluorocarbon-Exposed Sonicated Dextrose Albumin. J Am Coll Cardiol 1996; 27(6):1497-501.

Powers, J. E., Burns, P. N., and Souquet, J. Imaging Instrumentation for Ultrasound Contrast Agents. Advances in Echo Imaging Using Contrast Enhancement, N. C. Nanda, R. Schlief, and B. B. Goldberg, eds., Dubai, Kluwer Academic Publishers, 1997:139-170.

Prasad, P. V., Cannillo, J., Chavez, D. R., Pinchasin, E. S., Dolan, R. P., et al. First-Pass Renal Perfusion Imaging Using MS-325, an Albumin-Targetted MRI Contrast Agent. Invest Radiol 1999; 34(9):566-571.

Ragosta, M., Camarano, G., Kaul, S., Powers, E. R., Sarembock, I. J., et al. Microvascular Integrity Indicates Myocellular Viability in Patients with Recent Myocardial Infarction: New Insights Using Myocardial Contrast Echogocardiography. Circulation 1994; 89(6):2562-2569.

Rayleigh, L. On the Pressure Developed in a Liquid During the Collapse of a Spherical Cavity. Philosophy Magazine 1917; Series 6(34):94-98.

Riesz, P., Barndahl, D., and Christman, C. L. Free Radical Generation by Ultrasound in Aqueous and Non -Aqueous Solutions. Environmental Health Perspectives 1985; 64:233-252.

Riesz, P., and Christman, C. L. Sonochemical Free Radical Formation in Aqueous Solutions. Federation Proceedings 1986; 45(10):2485-2492.

Rubin, J. M., Adler, R. S., Fowlkes, J. B., Spratt, S., Pallister, J. E., et al. Fractional Moving Blood Volume: Estimation with Power Doppler US. Radiology 1995; 197:183-190.

Schelbert, H. R. Consideration of Measurements of Myocardial Blood Flow with Positron-Emission Tomography. Invest Radiol 1993; 28(Supplement 4):S47-S55.

Schleher, D. C. MTI and Pulsed Doppler Radar, chap. 5: Theory of Optimum Radar Doppler Processing. Norwood,MA: Artech House, Inc., 1991.

Schlief, R. Developments in Echo-Enhancing Agents. Clin Rad 1996; 51(Supplement 1):5-7.

Schmermund, A., Gerber, T., Behrenbeck, T., Reed, J. E., Sheedy, P. F., et al. Measurement of Myocardial Infarct Size By Electron Beam Computed Tomography: A Comparison with 99m-Tc Sestamibi. Invest Radiol 1998; 33(6):313-321.

Schwarz, K. Q., Bezante, G. P., Chen, X., and Schleif, R. Quantitative Echo Contrast Concentration Measurement by Doppler Sonography. Ultrasound Med Biol 1993; 19(4):289-297.

Schwarz, K. Q., Chen, X., Bezante, G. P., Phillips, D., and Schlief, R. The Doppler Kinetics of Microbubble Echo Contrast. Ultrason Med Biol 1996; 22(4):453-462.

Senior, R., Kaul, S., and Lahiri, A. Myocardial Viability on Echocardiography Predicts Long-Term Survival After Revascularization in Patients With Ischemic Congestive Heart Failure. J Am Coll Cardiol 1999; 33(7):1848-1854.

Shi, W. T., Forsberg, F., Hall, A. L., Chiao, R. Y., Liu, J.-B., et al. Subharmonic Imaging With Microbubble Contrast Agents: Intial Results. Ultrasonic Imaging 1999a; 21:79-94.

Shi, W. T., Forsberg, F., Raichlen, J. S., Needleman, L., and Goldberg, B. B. Pressure Dependence of Subharmonic Signals From Contrast Microbubbles. Ultrasound Med Biol 1999b; 25(2):275-283.

Shung, K. K., Sigelman, R. A., and Reid, J. M. Scattering of Ultrasound by Blood. IEEE Transactions on Biomedical Engineering 1976; 23(6):460-467.

Shung, K. K., and Thieme, G. A. Ultrasound Scattering in Biological Tissues. , Boca Raton, CRC Press, 1993.

Skorton, D. J., Schelbert, H. R., Wolf, G. L., and Marcus, M. L. Heart Disease: A Textbook of Cardiovascular Medicine, 4th edition, chap. 12. Philadelphia: W. B. Saunders Company, 1992.

Skyba, D. M., Camarano, G., Goodman, N. C., Price, R. J., Skalak, T. C., et al. Hemodynamic Characteristics, Myocardial Kinetics and Microvascular Rheology of FS069, a Second-Generation Echocardiographic Contrast Agent Capable of Producing Myocardial Opacification From a Venous Injection. J Am Coll Cardiol 1996; 28(5):1292-1300.

Sontum, P. C., Ostensen, J., Dyrstad, K., and Hoff, L. Acoustic Properties of NC100100 and Their Relation With the Microbubble Size Distribution. Invest Radiol 1999; 34(4):268-275.

Stevens, W. R., Johnson, C. D., Stephens, D. H., and Batts, K. P. CT Findings in Hepatocellular Carcinoma: Correlation of Tumor Characteristics with Causative Factors, Tumor Size, and Histologic Tumor Grade. Radiology 1994; 191:531-537.

Suslick, K. S. The Chemical Effects of Ultrasound. Sci Am 1989; (February):80-86.

Tanaka, S., Kitamra, T., Yoshioka, F., Kitamura, S., Yamamoto, K., et al. Effectiveness of Galactose-Based intravenous Contrast Medium on Color Doppler Sonography of Deeply Located Hepatocellular Carcinoma. Ultrason Med Biol 1995; 21(2):157-160.

Taylor, C. R., Garcia-Tsao, G., Henson, B., Case, C. Q., and Taylor, K. J. W. Doppler Ultrasound in the Evaluation of Cirrhotic Patients: The Prevalence of Intrahepatic Arteriovenous Shunting and Implications for Diagnosis of Hepatocellular Carcinoma. Ultrasound Med Biol 1997; 23(8):1155-1163.

Taylor, K. J. W. Pulse Doppler and Colour Flow of Tumours. Clinical Applications of Doppler Ultrasound, K. J. W. Taylor, P. N. Burns, and P. N. T. Wells, eds., New York, Raven Press Ltd., 1995:355-366.

Taylor, K. J. W., Burns, P. N., and Wells, P. N. T. Clinical Applications of Doppler Ultrasound. , New York, Raven Press, 1995.

Tiemann, K., Lohmeier, S., Kuntz, S., Koster, J., Pohl, C., et al. Real-Time Contrast Echo Assessment of Myocardial Perfusion at Low Power: First Experimental and Clinical Results Using Power Pulse Inversion Imaging. Echocardiography 1999; 16(8):799-809.

Torp, H. Clutter Rejection Filters in Color Flow Imaging: A Theoretical Approach. IEEE Transaction on Ultrasonics, Ferroelectrics, and Frequency Control 1997; 44(2):417-424.

Tranquart, F., Grenier, N., Eder, V., and Pourcelot, L. Clinical Use of Ultrasound Tissue Harmonic Imaging. Ultrasound Med Biol 1999; 25(6):889-894.

Trilling, L. The Collapse and Rebound of a gas Bubble. J Appl Phys 1952; 23(1):14-17.

Uhlendorf, V. Physics of Ultrasound Contrast Imaging: Scattering in the Linear Range. IEEE Trans Ultrason, Ferroelect, Freq Contr 1994; 41(1):70-79.

Uhlendorf, V., and Hoffman, C. Nonlinear Acoustical Response of Coated Microbubbles in Diagnostic Ultrasound. Proc IEEE Ultrasonics Symp 1994; :1559-1564.

Unger, E., Metzger, P., Krupinski, E., Baker, M., Hulett, R., et al. The Use of a Thrombus-Specific Ultrasound Contrast Agent to Detect Deep Thrombus in Arteriovenous Fistulae. Invest Radiol 2000; 35(1):86-89.

Unger, E. C., McCreery, T. P., and Sweitzer, R. H. Ultrasound Enhances Gene Expression of Liposomal Transfection. Invest Radiol 1997; 32(12):723-727.

Van Der Wall, E. E., Blanksma, P. K., Neimeyer, M. G., Vaalburg, W., and Crijns, H. J. G. M. Advanced Imaging in Coronary Artery Disease. Developments in Cardiovascular Medicine, Boston, Kluwer Academic Publishers, 1998.

Villanueva, F. S., Camarano, G., Ismail, S., Goodman, N. C., Sklenar, J., et al. Coronary Reserve Abnormalities in the Infarcted Myocardium: Assessment of Myocardial Viability Immediately Versus Late After Reflow by Contrast Echocardiography. Circulation 1996; 94:748-754.

Volkurka, K. Comparison of Rayleigh's, Herrings, and Gilmore's Models of Gas Bubbles. Acoustica 1986; 59:214-219.

Ward, B., Baker, A. C., and Humphrey, V. F. Nonlinear propagation applied to the improvement of resolution in diagnostic medical ultrasound. J Acoust Soc Am 1997; 101(1):143-154.

Wei, K., Jayaweera, A. R., Firoozan, S., Linka, A., Skyba, D. M., et al. Quantification of Myocardial Blood Flow With Ultrasound-Induced Destruction of Microbubbles Administered as a Constant Infusion. Circulation 1998; 97:473-483.

Wielgosz, A., Arango, M., Carew, M., Ferguson, A., Johansen, H., et al. The Changing Face of Heart Disease and Stroke in Canada. , Ottawa, Heart and Stroke Foundation of Canada, 1999.

Williams, A. R., Kubowicz, G., and Cramer, E. The Effects of the Microbubble Suspension SHU 454 (Echovist) on Ultrasound-Induced Cell Lysis in a Rotating Tube Exposure System. Echocardiography 1991; 8(4):423-433.

Wilson, L. S. Description of a Broad-band Pulsed Doppler Ultrasound Processing Using the Two-Dimensional Fourier Transform. Ultrasonic Imaging 1991; 13:301-315.

Winkler, P., and Helmke, K. Major Pitfalls in Doppler Investigations with Particular Reference to the Cerebral Vascular System Part I. Sources of Error, Resulting Pitfalls and Measures to Prevent Errors. Ped Radiol 1990; 20:219-228.

Winkler, P., Helmke, K., and Mahl, M. Major Pitfalls in Doppler Investigations Part II. Low Flow velocities and Colour Doppler Applications. Ped Radiol 1990; 20:304-310.

Wu, K. C., Kim, R. J., Bluemke, D. A., Rochette, C. E., Zerhouni, E. A., et al. Quantification and Time Course of Microvascular Obstruction by Contrast-Enhanced Echocardiography and Magnetic Resonance Imaging Following Acute Myocardial Infarction and Reperfusion. J Am Coll Cardiol 1998a; 32(6):1756-64.

Wu, Y., Unger, E. C., McCreery, T. P., Sweitzer, R. H., Shen, D., et al. Binding and Lysing of Blood Clots Using MRX-408. Invest Radiol 1998b; 33(12):880-885.